A NEW FAMILY OF PROTON CONDUCTING ELECTROLYTES WITH ENHANCED STABILITY FOR REVERSIBLE FUEL CELL OPERATION: $BaHf_xCe_{0.8-x}Y_{0.1}Yb_{0.1}O_3$

A Dissertation
Presented to
The Academic Faculty

by

Ryan Joe Murphy

In Partial Fulfillment
of the Requirements for the Degree
Doctor of Philosophy in the
School of Materials Science and Engineering

Georgia Institute of Technology
December 2019

A NEW FAMILY OF PROTON CONDUCTING ELECTROLYTES WITH ENHANCED STABILITY FOR REVERSIBLE FUEL CELL OPERATION: $BaHf_xCe_{0.8-x}Y_{0.1}Yb_{0.1}O_3$

Approved by:

Dr. Meilin Liu, Advisor
School of Materials Science and Engineering
Georgia Institute of Technology

Dr. Mark Losego
School of Materials Science and Engineering
Georgia Institute of Technology

Dr. Preet Singh
School of Materials Science and Engineering
Georgia Institute of Technology

Dr. Angus Wilkinson
School of Chemistry and Biochemistry
Georgia Institute of Technology

Dr. Hamid Garmestani
School of Materials Science and Engineering
Georgia Institute of Technology

Date Approved: July 26, 2019

ACKNOWLEDGEMENTS

First and foremost, I would like to thank my parents for their love and support throughout my time at Georgia Tech. Next, I would like to thank my advisor, Dr. Meilin Liu who has helped guide my research and develop my scientific reasoning. I would also like to thank all the past and present members of our research group who have all contributed in various ways to improving my research, maintaining the lab, and overall enjoyment: Dr. Yu Chen, Dr. Bote Zhao, Dr. Gordan Waller, Dr. Seonyoung Yoo, Dr. Ben Rainwater, Dr. Samson Lei, Dr. Jun Kim, Dr. Ben Deglee, Dr. Yucun Zhou, Dr. Ali Abdelhafiz, Yuchen Liu, Lei Zhang, Weilin Zhang, Jerry Luo, Nick Kane, and Luke Soule as well as all the visiting members. I would like to specifically thank Lei Zhang for his help with the computational work in this dissertation and discussions on first principles analysis. I would also like to thank Dr. Yucun Zhou for his help in fabricating and testing of full cells. I would also like to thank the staff of the Materials Characterization Facility, especially David Tavakoli, for not only his help in training and analysis, but also for making it much more enjoyable to spend time in the MCF. I would also like to thank my roommate for the past five years, Kevin Chan, and our roommates at "the house," Jeff Luo, Chris Perini, and Kasey Hanson. Graduate school would have been a lot less enjoyable without basement brewed beer and game-nights. Lastly, I would like to acknowledge the funding sources which have made this research possible: The Nanomaterials for Energy Storage and Conversion IGERT fellowship program and the Phillips 66 Energy Transition Division.

TABLE OF CONTENTS

LIST OF TABLES

LIST OF FIGURES

LIST OF SYMBOLS AND ABBREVIATIONS

ΔG	Gibbs Free Energy
BHCYYb	$BaHf_xCe_{0.8-x}Y_{0.1}Yb_{0.1}O_3$; any numbers following represent relative dopants in the B-site (e.g. BZCYYb-1711 = $BaZr_{0.1}Ce_{0.7}Y_{0.1}Yb_{0.1}O_3$
BZCYYb	$BaZr_xCe_{0.8-x}Y_{0.1}Yb_{0.1}O_3$; any numbers following represent relative dopants in the B-site (e.g. BZCYYb-1711 = $BaZr_{0.1}Ce_{0.7}Y_{0.1}Yb_{0.1}O_3$
DFT	Density Functional Theory
EIS	Electrochemical Impedance Spectrometry
MPD	Maximum Power Density
OCV	Open Circuit Voltage
SEM	Scanning Electron Microscopy
SOEC	Solid Oxide Electrolysis Cell
SOFC	Solid Oxide Fuel Cell
TGA	Thermo-Gravimetric Analysis
XPS	X-ray Photoelectron Spectroscopy
XRD	X-Ray Diffraction
YSZ	Yttria-Stabilized Zirconia

SUMMARY

Solid oxide fuel cell (SOFC) technology has the potential to be one of the most efficient energy conversion technologies and the same technology can be used to efficiently produce several chemical species such as hydrogen and syngas through reverse operation, known as solid oxide electrolysis cells (SOEC). However, SOFC's high temperature requirement limit the feasibility and cost-competitiveness of the technology. There has been significant work in recent years to reduce the required operating temperature. One successful method is the shift from oxygen ion conductors to proton conductors as the electrolyte material. This has led to the development of the current state-of-the-art electrolyte material: $BaZr_{0.1}Ce_{0.7}Y_{0.1}Yb_{0.1}O_3$ (BZCYYb). While this material has enabled record breaking fuel cell performance, several challenges remain for broader commercialization such as limited stability against high concentration of water and CO_2, which become more pronounced in the electrolysis mode (SOEC) where the material could be exposed to pure CO_2 or steam.

In order to address the degradation issues with BZCYYb, this work has developed a new family of proton conducing electrolyte materials, $BaHf_xCe_{0.8-x}Y_{0.1}Yb_{0.1}O_3$ (BHCYYb). This material is theoretically more stable than that of BZCYYb due to $BaHfO_3$'s higher stability but the increase in stability must not significantly hinder performance. Therefore, the conductivity and transference numbers of BHCYYb were measured to evaluate it as an electrolyte material. The conductivity of BHCYYb-1711 was determined to be about 50% higher than that of BZCYYb-1711. As the concentration of hafnium was increased, the conductivity decreased as expected but at a faster rate than BZCYYb as the zirconium concentration increased. This resulted in BHCYYb-3511 and BZCYYb-3511 having

approximately the same conductivity and higher concentrations of Zr/Hf resulted in BZCYYb having the higher conductivity. To verify the higher conductivity was due solely to ionic conductivity, the transference numbers were also tested. At SOFC testing temperatures, the transference numbers in hydrogen and SOFC conditions were above 0.9 and the transference increased as the temperature decreased. Due to these positive results, BHCYYb was used to fabricate full cells and their peak power densities of 1.67 W/cm^2 and 1.45 W/cm^2 at 700ºC and 650ºC respectively are equal to that of the highest performance cells in literature.

Based on the positive results achieved as an SOFC electrolyte, the stability of BHCYYb was tested using TGA, XRD and conductivity. In all cases, BHCYYb proved to have higher stability. 30% hafnium was needed for complete stability, yet 30% zirconium would degrade. Based on the higher chemical stability, BHCYYb was used to fabricate electrolysis cells and tested for steam electrolysis and CO_2-H_2O co-electrolysis. For steam electrolysis, round trip efficiencies above 80% were achieved at 0.5 A/cm^2 and above 70% for 1 A/cm^2. For CO_2-H_2O co-electrolysis, BHCYYb-3511 was compared to several different electrolytes including BZCYYb-1711 and BZCYYb-3511. In all cases the cells degraded in less than 50 hours while BHCYYb-3511 was stable for over 100 hours with no discernable degradation.

Finally, several novel dopant systems were studied in the $BaHfO_3$ system to attempt to further improve the performance of $BaHfO_3$ based systems. Both dopants in the A-site and B-site were tested. Unfortunately, A-site doping proved to be impossible with common ceramic processing techniques to due to the alkaline metals evaporating from the structure at ~800ºC. Several B-site dopants were tested as well. Indium proved to be very promising

with the highest conductivity of all the dopants tested in $BaHfO_3$. However, when indium was used in a $BaCeO_3$-$BaHfO_3$ solid solution, the performance was quite poor. Indium is a poor dopant in the $BaCeO_3$ system, so it's advantage with hafnium could not be overcome.

CHAPTER 1. INTRODUCTION

1.1 Motivation

Climate change is considered by a majority, if not all, scientists as humanity's greatest existential crisis.[1]–[5] This crisis is odds with the fact that fossil fuels contribute to every aspect of our economy from power generation, to transportation, to the production of a large number of synthetic materials. With a challenge so large, no one technology can provide a solution. Wind, solar, and other renewable power generation technologies are by far the fastest growing segment of the energy grid but there are still significant challenges.[6] For example, wind and solar are intermittent power sources which increases the need for energy storage and there is still no economical solution for the 40% of transportation, such as air travel or heavy freight, which cannot run on today's battery technology.[7]–[9] One technology, among many, which has potential in efficient electricity generation as well as production of several chemical species is solid oxide fuel cells (SOFCs).

1.2 Role of solid oxide fuel cell technology in a carbon neutral economy

Fuel cells are an extremely efficient method of producing electricity, and when used in a combined heat and power system, they can achieve efficiencies of up to 80%.[10] There are several different types of fuel cell technology. According to the electrolyte materials used, fuel cells are classified into proton exchange membrane (PEM) fuel cells, alkaline fuel cells, phosphoric acid fuel cells, and solid oxide fuel cells (SOFCs).[11] Each of these technologies has their individual advantages and disadvantages. PEM and alkaline fuel

cells operate close to room temperature and phosphoric acid fuel cells operate at only marginally higher temperatures of 150ºC to 200ºC.[12] These temperatures are much lower than those required for SOFC operation. However, the high operation temperature of SOFCs provide several advantages. PEM and phosphoric acid fuel cells require noble metal catalyst such as platinum, greatly increasing their cost.[11] Additionally, PEM and alkaline fuel cells are highly sensitive to carbon dioxide, sulfur, and other chemical species common in fuels.[13] These restrictions limit these fuel cell technologies to operation on pure hydrogen. While hydrogen on its own does not produce carbon dioxide or other greenhouse gases, almost all hydrogen today is produced through steam reforming of natural gas, which does contribute.[14] Partial oxidation reacts hydrocarbons with a very controlled amount of oxygen to create carbon monoxide and hydrogen as shown in Equation (1). This mixture, known as syngas, is the starting material for several modern chemical processes. Specifically the production of methanol and ethylene glycol, which in turn are used in a number of other chemical processes.[15], [16] In hydrogen production the carbon monoxide is a waste product and must be separated from the hydrogen. Gas separation is an extremely energy intensive process which adds to the carbon released into the atmosphere.[17] So, while hydrogen fuel cells themselves do not produce any greenhouse gas, the process by which the hydrogen is created makes them less environmentally friendly than they first appear.[18], [19]

$$C_xH_y + \frac{x}{2}O_2 \Rightarrow xCO + \frac{y}{2}H_2 \quad \textbf{(1)}$$

This highlights one of the major advances of SOFC technology. The high operating temperature allows SOFCs to directly operate on hydrocarbons such as natural gas without

an additional reformer, which gives SOFCs the highest theoretical efficiency of any competing energy generation technology at low cost. Moreover, SOFCs ability to run directly on both natural gas and hydrogen make it an ideal transition technology for the switch from natural gas to hydrogen, as clean hydrogen production technology matures.[20], [21]

While SOFCs have promise as an electricity generation and energy transition technology, there are significant challenges. Another application of SOFC technology is as reversable fuel cells for energy storage or for electrolysis. Electrolysis is the process of using electricity to reverse a chemically unfavorable reaction. Electrolysis can be used to produce several critical species such as hydrogen, syn gas, and ammonia which are currently obtained from natural gas or other fossil fuels.[22]–[28] While electrolysis does not directly produce greenhouse gasses, this process requires more energy to produce the hydrogen than would be gained by reacting the hydrogen or other species. Thus, when traditionally produced electricity is used the net carbon released is still positive. However renewable energy such as solar and wind are quickly becoming cost competitive with traditional coal and natural gas power plants. As the price of renewable energy decreases so does the cost of electrolysis and the cost of hydrogen or syn gas.[12], [13]

This also has the potential to have carry-over effects into the carbon capture industry. If economical, producing syngas from carbon dioxide would have huge impacts on the power and chemical production industries.[25] Currently, carbon dioxide sequestrated from power plants has very limited uses.[29] Most of the time the CO_2 is simply injected into empty oil and gas wells.[30] While there are some limited uses for captured CO_2 such as fracking and enhanced oil recovery, the limited use cases makes carbon capture at power

plants very expensive.[31] If there was an efficient method, such as solid oxide electrolysis cells, for converting that captured CO_2 into syngas which could in turn be sold to chemical companies, carbon capture would become a more cost competitive option for limiting carbon emissions.

1.3 Challenges for SOFC Technology

While solid oxide fuel cell technology is very efficient for energy storage and conversion, there are significant challenges which must be overcome in order to make SOFC technology cost competitive with traditional energy generation technologies. High temperature insulation, high chromium content electrical interconnects, and long start-up times are just some of the challenges facing SOFC technology.[32], [33] The high operating temperature requires the use of exotic materials. For example, electrical connections must be made with metals of high oxidation resistance such as chromium containing stainless steels. However, the chromium used to prevent the stainless-steel oxidation can leach into the gas stream and degrade fuel cell performance.[34], [35] The same is true for the gas seals which are typically made from a boron-based glass. At high temperatures, the boron can also leach into gas stream and poison cells.[36]–[38]

Reduction of the high temperature requirements has been a long-standing challenge, but significant progress has been made. There has been a major shift away from oxygen conducting materials to proton conducting materials. These proton conducing oxides have much lower activation energies, which allows them to retain their performance at lower temperatures.[39] Improvements in the catalytic activity of cathode materials has pushed the required operating temperatures even lower.[40]–[42] It is becoming increasingly

possible to achieve high performance at temperatures at or below 500°C.[43], [44] However, this success in reducing the required operating temperature has revealed new challenges. Specifically, the proton conducing materials which have enabled the reduction of the operating temperature are unstable against CO_2 and water.[45] Moreover, the degradation reactions become more favorable thermodynamically as the temperature is reduced, preventing further decrease in operating temperature while maintaining device stability.[46] This has severely limited the deployment of SOFC technology, especially for electrolysis applications, which require high concentrations of both CO_2 and water. New materials are needed which retain the current performance metrics but are more stable against CO_2, water, and other contaminates in order to increase the competitiveness of SOFC and SOEC technology for efficient energy conversion and storage.

1.4 Research Objectives

The work in this dissertation involves the development of a new proton-conducting SOFC electrolyte material, $BaHf_xCe_{0.8-x}Y_{0.1}Yb_{0.1}O_3$. Specifically, the main objectives of this dissertation research are:

- To develop a new proton conducting material, with higher theoretical stability than current state-of-the-art.
- To evaluate the long-term stability of the newly developed electrolyte material in realistic operating conditions.
- To identify novel dopants for the $BaHfO_3$ system and evaluate their performance.

Achieving these objectives will hopefully provide insight towards the further development of SOFC technology. This type of fundamental information is necessary to drive SOFC

technology towards commercialization. In addition, this work presents initial efforts into further improvements to performance and stability.

1.5 Chapter Organization

Chapter 2 provides the fundamentals of solid oxide fuel cell technology, describes the shift to proton conducting electrolytes, including a review of the current state-of-the-art material, BZCYYb, and discusses the current challenges. Chapter 3 descries the technical approach used to achieve the objectives of this dissertation research, together with experimental details for fabrication and evaluation of the new materials developed. Chapter 4 describes the development of the new family of proton conducing electrolytes and its evaluation as an electrolyte material for fuel cell and electrolysis operation. Chapter 5 describes the stability testing of the new BHCYYb material and compares it to the current state-of-the-art. Chapter 6 attempts to further improve the performance by studying dopants in the $BaHfO_3$ system. Finally, Chapter 7 provides a concluding summary as well as some recommendations for future work.

CHAPTER 2. BACKGROUND

2.1 Solid Oxide Fuel Cell Fundamentals

Fuel cells are an electrochemical method of converting chemical energy into electrical power. To produce electricity, fuel cells use the highly energetic reaction between hydrogen or hydrocarbons and oxygen to produce water. This reaction is highly exothermic and produces a large amount of energy. Fuel cells use electrochemistry to harness and control this reaction by separating the combustion reaction into two half reactions.[10], [47], [48]

There are three active materials needed for fuel cell operation: the anode, the cathode and the electrolyte. Figure 2-1 shows a schematic of a fuel cell and the role of each active material. On the anode, hydrogen is oxidized as shown in Equation (2). On the cathode, the electrons reduce oxygen as shown in Equation (3). The electrolyte only allows ions to pass through, which forces the electrons through an external circuit, which produces power. Finally, the protons and oxygen ions combine to create water.[47]

$$H_2 = 2H^+ + 2e^- \quad \textbf{(2)}$$

$$\frac{1}{2}O_2 + 2e^- = O^{2-} \quad \textbf{(3)}$$

$$2H^+ + O^{2-} = H_2O \quad \textbf{(4)}$$

2.2 Solid Oxide Proton Conducting Electrolytes

As was mentioned, there are three major active components to an SOFC system: the anode, cathode and electrolyte. This work focuses on the electrolyte, of which there are two major types: oxygen conductors and proton conductors. As their names suggest, the major distinguishing factor is the ionic species which they transport. Figure 2-1 shows schematics of fuel cells based on an oxygen conducting and proton conducting electrolyte.

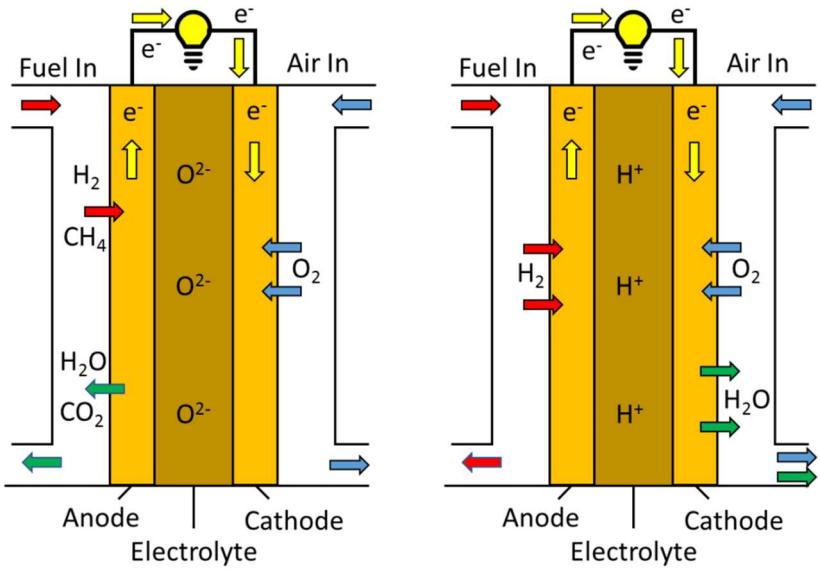

Figure 2-1 Schematic of a solid oxide fuel cell with an oxygen conducting electrolyte (left) and proton conducting electrolyte (right).

Of the two types of electrolytes, proton conductors are widely considered to be the preferred structure due to their lower activation energies and higher conductivities, especially at lower temperatures. The most common SOFC proton conductors have a barium perovskite structure with a chemical formula of $BaMO_3$ where M is a 4+ metal ion

such as cerium.[49]–[51] The perovskite structure consists of a cubic unit cell with the larger of the two metal ions at the unit cell corners in a 12-coordinated site. The oxygen sit at the face centers and the smaller metal ion sits in the octahedral site in the center of the unit cell. The 12- coordinated site is known as the A-site and the octahedral site is the B-site. In oxygen-based perovskites the two metal ions' charge must sum to 6^+ to balance the oxygen. Therefore, for barium-based perovskites, the B-site atom is required to have a 4^+ charge.[52] A schematic of the unit cell of this structure is shown in Figure 2-2(a).

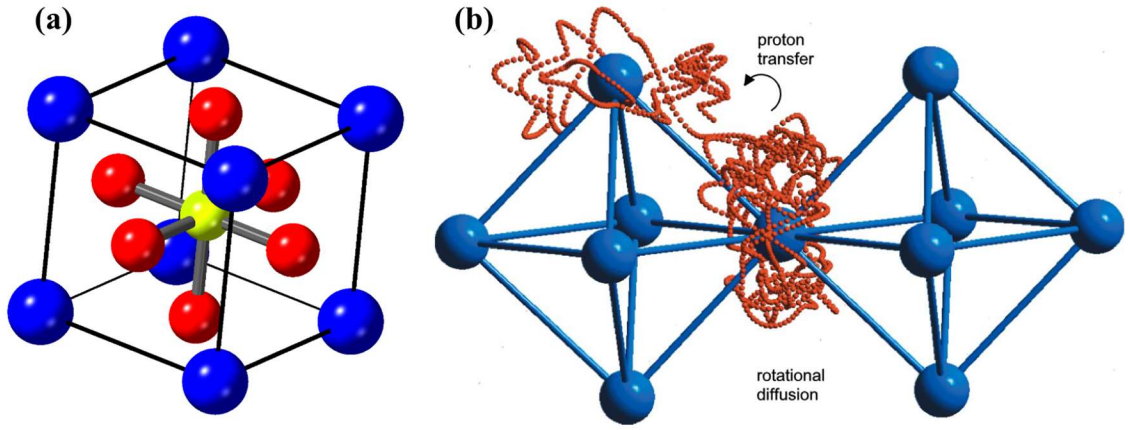

Figure 2-2 (a) Barium perovskite unit cell. Barium is in blue, oxygen is in red, and the 4+ ion is in yellow. (b) Schematic of proton movement through a barium perovskite. (Reprinted with permission from Kreuer, K. D. (2003). *Annual Review of Materials Research*, *33*(1), 333–359. Copyright 2003, Annual Reviews, Inc) [51]

In order to make this structure proton conducing, a fraction of the 4+ metal ions are replaced with 3+ metal ions, this in turn creates oxygen vacancies as shown in Equation (5) Finally, when the oxygen vacancies are exposed to water, the water fills the vacancy with a hydroxyl ion as shown in Equation (6).[53] They hydrogen is then relatively free to

rotate around the oxygen and then hop from oxygen to oxygen if there is a significant enough driving force creating proton conduction as shown in Figure 2-2 (b). [54], [55]

$$Y_2O_3 + O_2 \xrightarrow{BaMO_3} 2Y'_M + V_O^{\cdot\cdot} + 5O_O^x \quad \textbf{(5)}$$

$$V_o^{\cdot\cdot} + O_O^x + H_2O \Rightarrow 2OH_O^{\cdot} \quad \textbf{(6)}$$

2.3 Review of Current State-Of-The-Art Electrolyte Material - BZCYYb

$BaZr_{0.1}Ce_{0.7}Y_{0.1}Yb_{0.1}O_{3-\delta}$ (BZCYYb) has recently become the dominant electrolyte material for solid oxide fuel cells.[56]–[59] BZCYYb's dominance is due to a combination its high conductivity and natural resistance to both coking and sulfur.[60] This has led to significant improvements in the performance of solid oxide fuel cells. Recent papers have reported a peak power density of 0.690 W cm^{-2} at 600ºC in hydrogen[61] and a peak power density of 0.37 W cm^{-2} at 500ºC in methane with no evidence of coking.[62] In both cases BZCYYb was the electrode of choice.

While BZCYYb is an excellent choice as a SOFC electrolyte material in lab scale experiments, it becomes obvious it has several disadvantages when scale-up is attempted. For example, BZCYYb is known to degrade in both CO_2 and H_2O environments and high concentrations of both will be present at the end of any SOFC stack run on hydrocarbons. Furthermore, solid oxide electrolysis cells (SOECs) are gaining popularity[63]–[66] and require materials to be highly stable against CO_2 and H_2O. To increase the stability of BZCYYb, there have been systematic studies of replacing more of the cerium with

zirconium. Several studies have shown the need for 40% to 50% Zr needs to be doped into $BaCeO_3$ to create a stable phase in carbon dioxide or water, depending on exposure conditions and other dopants. While an increase in zirconium content does provide increased stability, it also decreases it's conductivity.[67]–[69] Therefore, novel dopant strategies are needed to maintain the current conductivity while improving the overall stability.

One potential strategy is to replace the zirconium with another element, such as hafnium to create a more stable structure. Thermodynamically, $BaHfO_3$ is more stable than $BaZrO_3$ with respect to carbon dioxide and water vapor as shown in Figure 2-3.[46], [70], [71] The large discontinuity in Figure 2-3(b) is due to the melting of $Ba(OH)_2$ at 680 K. Moreover, hafnium is chemically similar to zirconium, being from the same chemical group and having a similar ionic radius, 85 pm for hafnium compared to 86 pm for zirconium.[72] These chemical and physical similarities should allow hafnium to easily replace zirconium in $BaCeO_3$-$BaZrO_3$ systems currently used for SOFCs and the higher chemical stability should allow less hafnium, compared to zirconium, to achieve acceptable stability, improving overall conductivity.

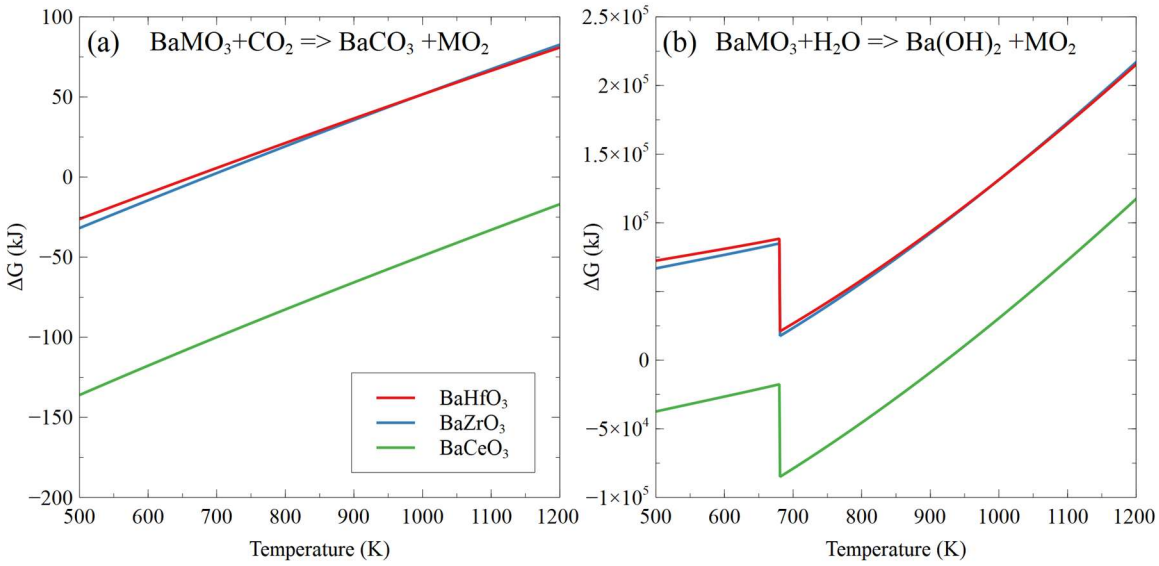

Figure 2-3 Free energy of the reactions between $BaMO_3$ (M = Ce, Zr, or Hf) and (a) CO_2 and (b) H_2O.

CHAPTER 3. TECHNICAL APPROACH

3.1 Material Design Rational

3.1.1 Thermodynamic Evaluation

The stability of a compounds is related to both the thermodynamic free energy of the reaction and the reaction kinetics. While the kinetics of the degradation can give important insight into the degradation mechanism, it is ideal to have a material which is thermodynamically stable and therefore will not degrade over time. The thermodynamic stability of a material is based on the Gibbs free energy of the degradation reaction. The Gibbs free energy of reaction is defined as:

$$\Delta G_{Reaction} = \Sigma\, G_{f(Products)} - \Sigma\, G_{f(Reactants)} \quad \textbf{(7)}$$

The free energy of the products and reactants is the sum of the free energies for formation of each of the products or reactants respectively. Gibbs free energy of formation is defined as:

$$G_f = H_f - TS_f \quad \textbf{(8)}$$

where ΔH_f is the enthalpy of formation and ΔS_f is the entropy of formation. The enthalpy and entropy of formation can be measured experimentally or calculated through first principle calculations.

While calculating the free energy of a reaction can be a very good predictor of stability, it becomes much more difficult to determine for doped or mixed compound such as BHCYYb due to the free energy of mixing. The free energy of formation for a mixture can be expressed as:

$$G_{f\ mixture} = X_a G_{f\ a} + X_b G_{f\ b} + G_{mixing} \quad \textbf{(9)}$$

For ideal mixtures, the enthalpy of mixing is zero and the entropy of mixing is simply the maximum configurational entropy which can be expressed as:

$$\mathrm{S} = -R(X_b \ln(X_a) + X_b \ln(X_b)) \quad \textbf{(10)}$$

$$G_{mixing} = RT(X_b \ln(X_a) + X_b \ln(X_b)) \quad \textbf{(11)}$$

However, ideal mixtures are not common and a better approximation of the systems in this study would be a regular solution. A regular solution is assumed to have an entropy of mixing equal to that of an ideal solution but an enthalpy which differs from that of an ideal solution. Both barium hafnate and barium cerate both has the same crystal structure and therefore is can be assumed the two materials will randomly disperse within each other approximating a regular solution. A regular solution has an enthalpy of mixing of:

$$H_{mixing} = \Omega X_a X_b \quad \textbf{(12)}$$

where Ω is a constant independent of temperature or composition. Therefore, the free energy of mixing for a regular mixture is:

$$G_{mixing} = \Omega X_a X_b + RT(X_b \ln(X_a) + X_b \ln(X_b)) \quad \textbf{(13)}$$

While free energy can provide information about the stability of compounds, it doesn't provide a complete picture. The free energy of a reaction describes the equilibrium condition, but if one or more of the products is absent or at a non-equilibrium concentration in the system, Le Chatelier's principle states that the reaction will progress towards those products. This relationship is described by the equilibrium constant, which relates to the free energy of the reaction by:

$$\Delta G_{reaction} = -RT \ln(K) \quad \textbf{(14)}$$

Where for a general chemical reaction such as $\alpha A + \beta B \Leftrightarrow \gamma C + \delta D$

$$\mathrm{K} = \frac{[C]^{\gamma}[D]^{\delta}}{[A]^{\alpha}[B]^{\beta}} \quad \textbf{(15)}$$

While this is a multivariable equation, it is greatly simplified by the fact that all the products and reactions in the system of interest, apart from the contaminates, are solids. By definition, the activity of condensed phases is one and therefore the equation for the degradation of $BaMO_3$ materials can be simplified to:

$$\mathrm{K} = \frac{1}{P_{contaminate}} \quad \textbf{(16)}$$

This relationship allows the creation of van't Hoff plots which show the relationship between temperature and the critical pressure at which degradation products begin to form.[73]

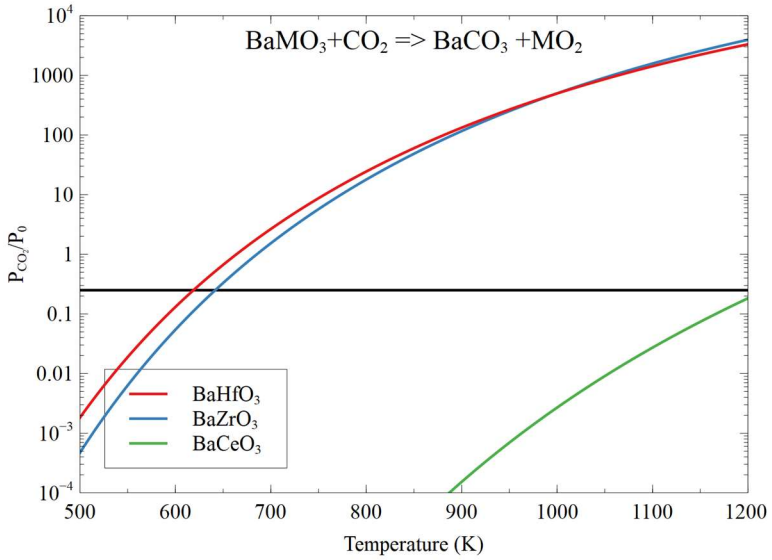

Figure 3-1 van't Hoff plot for the reactions between $BaMO_3$ with CO_2. The black line indicates 0.25 bar CO_2, or approximately 25% at atmospheric pressure. (M=Hf, Zr, Ce)

3.1.2 Material Selection

There are three different dopant schemes to optimizing stability and performance in $BaMO_3$ materials: 4^+ elements into the B-site, 3^+ elements into the B-site, and 1^+ elements into the A-site. Each dopant strategy will be reviewed briefly and the rational for how it will be studied will discussed.

The first dopant system is 4^+ elements into the B-site. $BaCeO_3$ and $BaZrO_3$ solid solutions have been studied extensively and it is well known that the addition of zirconium into the B-site will increase the stability.[67], [69] Additionally, titanium and tin have been studied

with limited success.[74]–[77] Conversely, hafnium has yet to be considered. To initially evaluate the thermodynamic stability of the $BaHfO_3$-$BaCeO_3$ system was compared to the $BaZrO_3$-$BaCeO_3$ system. Figure 3-2 shows van't Hoff plots for $BaHfO_3$, $BaZrO_3$, and $BaCeO_3$ in both CO_2 and H_2O atmospheres. At normal operation temperatures (500 – 700°C) $BaHfO_3$ is more stable than $BaZrO_3$ in both CO_2 and H_2O which shows that a higher stability can be achieved through the replacement of zirconium with hafnium. In the perovskite system.

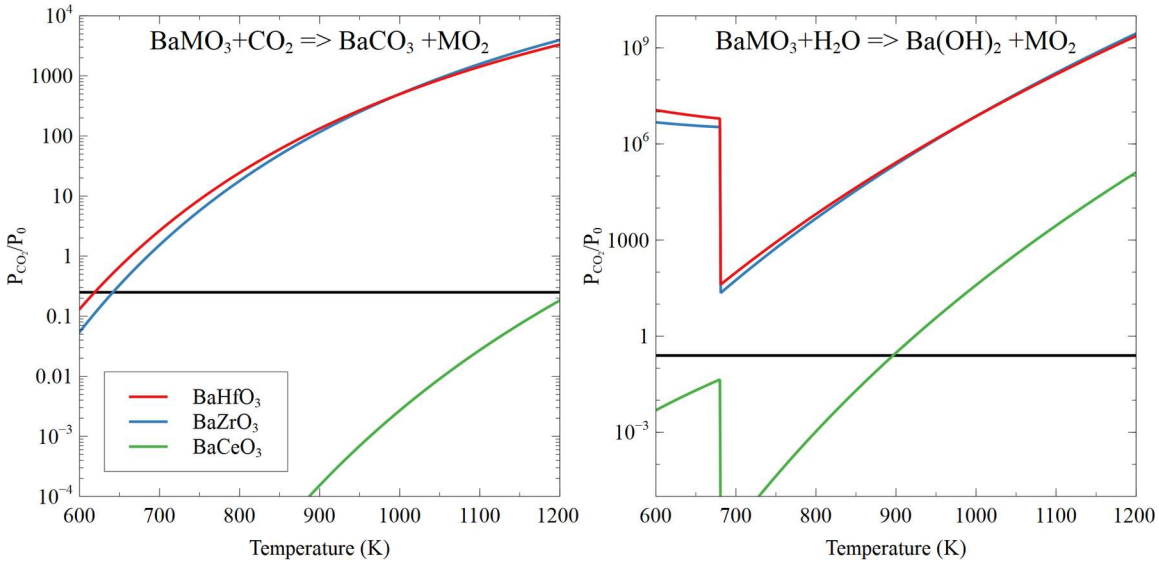

Figure 3-2 van't Hoff plots for $BaMO_3$ reacting with both CO_2 (left) and H_2O (right). (M = Hf, Zr, Ce)

The second dopant system is 3^+ elements in the B-site. The stability and conductivity effects have been widely studied in the $BaCeO_3$ and $BaZrO_3$ systems.[67], [78]–[82] Yttrium and ytterbium have been repeatedly shown to be the best dopants for those systems and are therefore a logical starting point. However, the effects of trivalent dopants in the $BaHfO_3$ system are expected to differ from the $BaCeO_3$ or $BaZrO_3$ systems and a better understanding is necessary to further improve performance.

Lastly, there has been very little experimental work on the effects of 1+ elements doped into the A-site. However, it has been studied extensively with simulations. DFT simulations have shown that A-site dopants in $BaZrO_3$ can have a significant impact on its stability. Moreover, those same simulations have shown that A-site dopants have higher stability with respect to carbon dioxide than yttrium, the most common B-site dopant. [46], [83], [84] While these simulations have shown some interesting results, they are limited to fractions of the lattice and specific concentrations require lattices which are computationally unreasonable. Therefore, experimental exploration is needed to fully understand the effects of A-site dopants on $BaMO_3$ materials.

3.2 Fabrication of Materials, Cell Components, and Single Cells

3.2.1 Fabrication of $BaHf_xCe_{0.8-x}Y_{0.1}Yb_{0.1}O_{3-\delta}$

To begin the process of studying the chemical stability of $BaHf_xCe_{0.8-x}Y_{0.1}Yb_{0.1}O_3$ (BHCYYb) we first began by fabricating high purity BHCYYb powder over the concentration range of $BaHf_xCe_{0.8-x}Y_{0.1}Yb_{0.1}O_3$ where X was varied in 0.1 increments from 0 to 0.8. To fabricate the high purity BHCYYb power, $BaCO_3$, HfO_2, CeO_2, Y_2O_3 and Yb_2O_3 were combined in appropriate mole ratios. The powders were mixed in ethanol using YSZ milling media for at least two hours. The ethanol was evaporated, and the powder was pressed into 32 mm pellet at 15 tons, 15 grams at a time. The resulting pellet was fired to 1100^{o}C for 12 hours. After the initial firing, the powder was ground in a high energy ball mill (Planetary Micro Mill PULVERISETTE 7 premium line) using 10mm media at 850 RPM for 4 cycles of 5 minutes each. Again, the powder was pressed into a 32mm pellet to 15 tons and fired to 1100^{o}C for 10 hours followed by 1450^{o}C for 5 hours.

3.2.2 Combustion method of powder synthesis

An alternative powder fabrication process which is commonly used to produce nano-powders is sol-gel combustion. This process requires mixing EDTA, glycine, and metal ions (as nitrates) in a 1:1.2:1 mole ratio. First a EDTA,-NH_3 buffer solution was created by adding 1M NH_4OH solution dropwise into a 0.1 M solution of EDTA to bring the pH to ~6. Next the metal nitrates, in proper mole ratios, were added slowly. The pH was regularly checked and NH_4OH added as necessary to keep the pH constant. Finally, the glycine was slowly added, again regularly checking the pH and adding NH_4OH as necessary. The solution was then dried on a hot-plate set at 150°C until a gel was formed. Once a gel was achieved, the hot-plate temperature was increased to 400°C until the gel auto-ignited creating a fine white powder. Lastly, the powder was calcined at 1000°C. [59], [85]–[87]

3.2.3 Sintering of BHCYYb

To sinter BHCYYb, 1 weight percent NiO was added a sintering aid.[88] The resulting mixture was ground in a high energy ball mill (10mm media at 850 RPM for 6 cycles of 5 minutes each) to achieve a particle size of approximately 1 micron as shown in Figure 3-3. The resulting powder was pressed into pellets at 60.3 kg/cm^2 (8 metric tons for a 13 mm diameter pellet). The pellets were fired at 1450°C for 5 hours with a ramp rate of 3°C per min heat and cool. This achieved a fully dense pellet as shown in Figure 3-4. For BHCYYb with a hafnium concentration greater than 50%, a sintering temperature of 1500°C was needed.

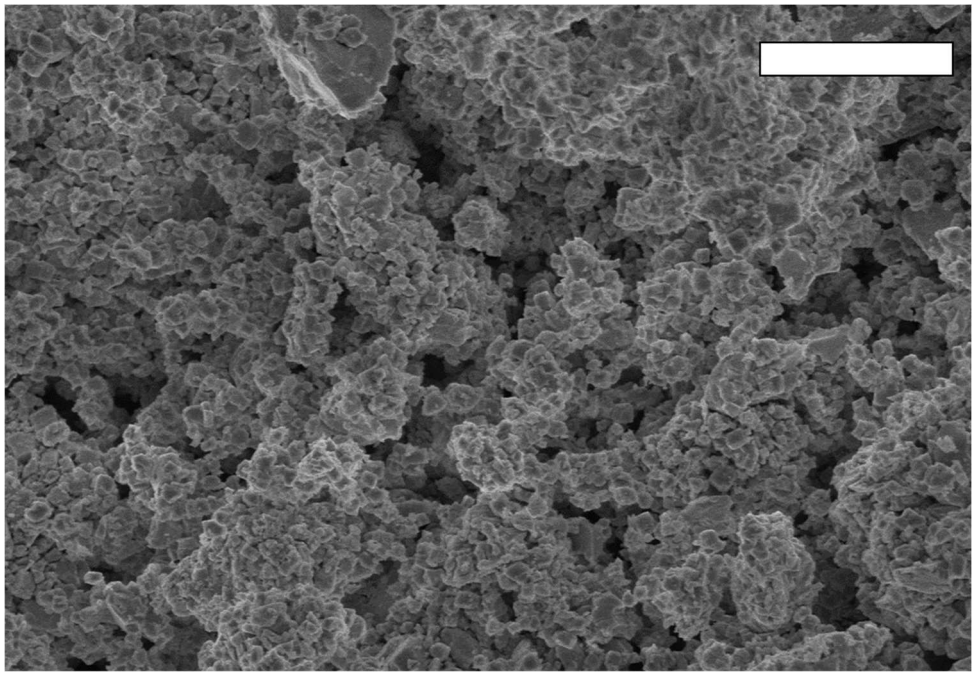

Figure 3-3 SEM images of $BaHf_{0.1}Ce_{0.7}Y_{0.1}Yb_{0.1}O_{3-\delta}$ powder after high energy ball milling. Scale bar is 5 µm.

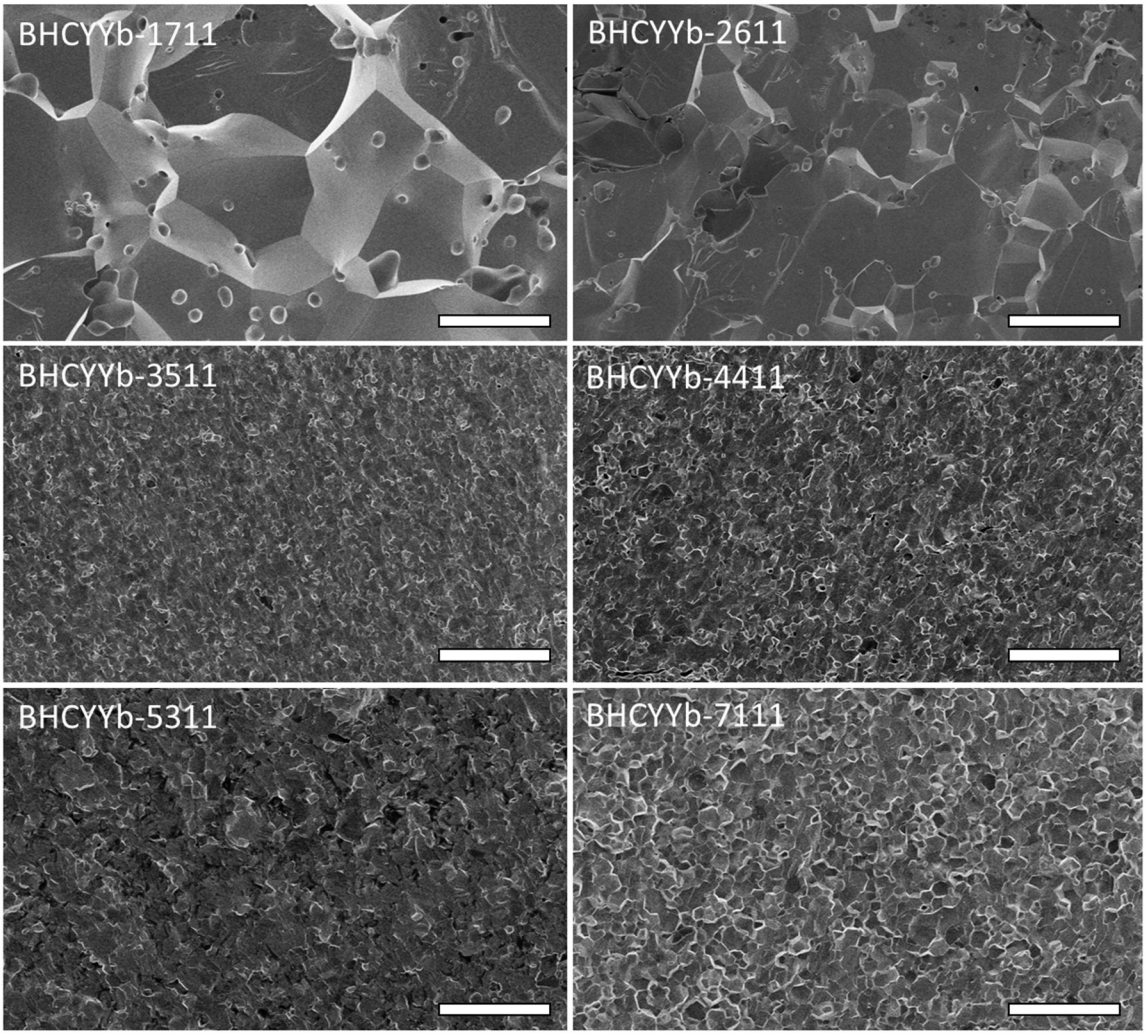

Figure 3-4 SEM images of a $BaHf_xCe_{0.8-x}Y_{0.1}Yb_{0.1}O_3$ pellet cross section after sintering. Scale bars are all 10 µm.

3.2.4 Fuel Cell Fabrication

Half cells with the configuration of Ni-BHCYYb anode supporting layer/Ni-BHCYYb anode functional layer/BHCYYb electrolyte layer were fabricated by the co-tape casting and co-sintering techniques. Specifically, the BHCYYb electrolyte powder, and the mixture of BHCYYb and NiO powder (NiO:YSZ=6:4 by weight) were mixed in ethanol

to form slurries. The slurry for tape casting was ethanol based and contained dispersing agent, binder, plasticizer and other additives, in addition to powder. The electrolyte layer was cast onto the Mylar film first. After drying, the anode functional layer was cast on top of the electrolyte layer, followed by the anode supporting layer. The tri-layer was then dried and co-sintered at 1400 °C for 5 hours in air. A $PrBa_{0.5}Sr_{0.5}Co_{1.5}Fe_{0.5}O_{5+\delta}$ (PBSCF) was added by screen printing the mixture of PBSCF powder and terpineol (5wt% ethyl cellulose) onto the electrolyte layer and firing at 950 °C for 2 hours in air. The PBSCF was synthesized by the combustion method described above.

3.3 Physical Characterization of Materials

3.3.1 X-ray Diffraction

XRD was used to confirm the phase of the materials and identify the degradation phases. X-rays are diffracted by the crystal lattice. Bragg's Law defines the wavelengths at which the diffracted x-rays will constructively interfere:

$$n\lambda = 2dsin\theta \tag{17}$$

Where n is the diffraction harmonic, λ is wavelength, d is inter-planar spacing, and θ is scattering angle. The x-ray intensity is measured as a function of 2θ. By comparing the position and intensity of the peaks to information in either the ICDD PDF-4+ database or the Crystallographic Open Database, the phase or phases present can be determined.

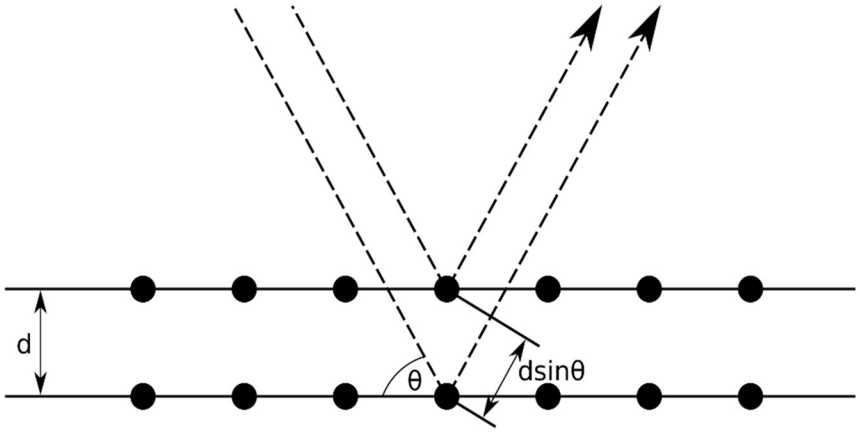

Figure 3-5 Schematic of how Bragg's Law determines lattice spacing. (Reproduced from public domain image courtesy of Wikimedia Commons)[89]

In addition to simply phase identification, Rietveld refinement can be performed on the x-ray diffraction pattern to determine information about the material. Most common the lattice parameters are determined, but information about crystallite size, strain, and elemental composition can also be determined with carful refinement. Moreover, if refinement is completed on a mixture of phases, the ratio of phases can be determined, although the other information gained, such as lattice parameter, become less accurate as the number of phases increases. Refinement will be completed in the Highscore Plus software package made by Panalytical.

3.3.2 Thermo-Gravimetric Analysis (TGA)

Thermo-gravimetric analysis (TGA) is a common technique for determining the temperature at which reactions occur by monitoring the mass of a sample as a function of temperature. In the case of BHCYYb, the sample would be exposed to CO_2 and if the sample reacted with the CO_2 the mass would increase as the sample degraded to $BaCO_3$. However, in the case of BHCYYb, there were two complications which needed to be

addressed in order to accurately study the stability. The first complication was that BHCYYb and similar materials are more stable at higher temperatures than at lower temperatures.[70] Therefore, if the TGA was run using the standard practice of increasing the temperature from room temperature to the temperature range of interest, the results would be skewed. To address this issue, the sample would be studied during cooling rather than heating. In order to reach the starting temperature without first reacting the sample, the analysis chamber would be flushed with argon. Once completely purged, the sample was quickly heated to the initial temperature of 1000°C. At 1000°C the gas was switched to CO_2 and the temperature slowly reduced to 400°C at 1°C per minute. The temperature and gas profiles for the experiments is shown in Figure 3-6 (a). A cooling rate of 1°C per minute was chosen to address the second major concern, the slow kinetics of the degradation reaction. Figure 3-6 (b) shows the cooling of BZCYYb-1711 in CO_2 with cooling rates from 10°C per minute to 0.5°C per minute. As the cooling rate decreases, the amount of degradation increases as well as the temperature at which the degradation occurs. However, once the cooling rate is 1°C per minute, decreasing it further does not change the degradation profile. Therefore, 1°C per minute was chosen for all the TGA experiments.

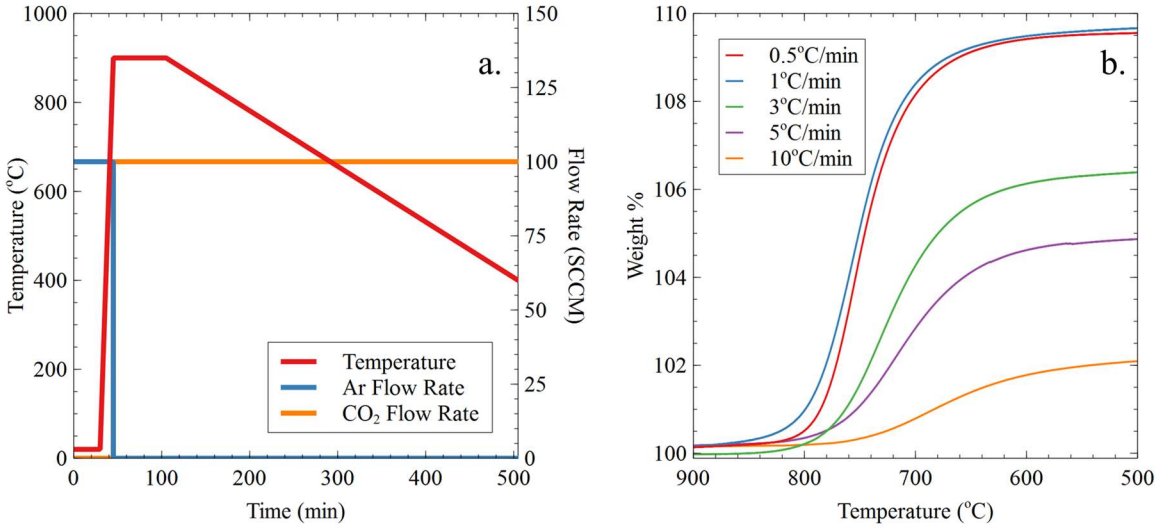

Figure 3-6 (a) Standard temperature and gas flow profiles for the TGA stability experiments. (b) Effect of the cooling rate on mass increase of BZCYYb in CO_2.

3.3.3 Long-Term Chemical Stability

While the TGA discussed above will provide an effective first test of BHCYYb's stability, it has a couple of limitations. The first is that SOFCs and similar systems have more complex gas mixtures. Specifically, they have high concentrations of hydrogen and water present, neither of which can be used in the TGA. The second is that SOFCs need to operate over extended periods of time at least thousands of hours. Therefore, the TGA results need to be verified over longer periods of time to ensure there is no degradation with kinetics too slow to be detected with the TGA.

In order to test the long-term chemical stability of BHCYYb, dense pellets fabricated according to the procedure above. These dense pellets were then exposed to various gas environments for 500 hours at 700°C. Due to BHCYYb's higher stability at higher temperatures, all temperature ramps and cooling was done in pure argon and the contaminate gases introduced once the furnace reached the test temperature. After

exposure, XRD was performed on the dense pellets. The XRD provided two pieces of valuable information. The first is the phases of the degradation products. The second is the relative extent of the degradation. Rietveld refinement was used to determine the amount of BZCYYb or BHCYYb remaining after exposure to the degradation environment and because x-rays penetrate BHCYYb and the degradation products to approximately the same extent the amount of BHCYYb detected relative to the degradation products is related to the extent of the degradation and therefore the degradation rate.

3.3.4 Long-Term Conductivity

Finally, once the long-term chemical stability was known, the long-term conductivity was needed to verify it would follow similar trends as the chemical stability. To determine this, dense pellets of BZCYYb and BHCYYb were prepared as discussed earlier. Once dense pellets were obtained, silver electrodes were applied to opposite sides. Silver was chosen as it is considered inert in these conditions and should not degrade over the course the tests. The pellets were then exposed to 25% CO_2, 25% H_2O, and 50% H_2 at 700^oC for 500 hours. The conductivity was recorded approximately every 24 hours over the course of the 500-hour test using electrochemical impedance spectrometry.

3.4 Electrochemical Characterization

3.4.1 Conductivity

Conductivity measurements were made on dense pellets. Silver electrodes were added using silver paste and adhered by firing at 800^oC for 2 hours. Ionic conductivity was measured with electrochemical impedance spectroscopy (EIS). In simplified terms, EIS

measures the impedance of the cell by applying a small AC bias (eg 10mV) around a fixed voltage over a frequency range and measuring the magnitude and phase of the current response. The impedance contributions of the different aspects can be modeled by equivalent circuit elements of resistors, capacitors, and inductors. Total impedance is referred to as "Z" and is written as vector shown below:

$$\mathrm{Z} = Z_{real} - jZ_{imaginary} \tag{18}$$

The real component of impedances comes from the resistive elements and is frequency independent. The imaginary components are from the capacitance and inductive elements and are frequency dependent. These relationships are shown below where R is resistance, L is inductance, C is capacitance, ω is frequency of the applied voltage and j is the imaginary unit $\sqrt{-1}$

$$Z_{real} = R \tag{19}$$

$$Z_{im,L} = j\omega L \tag{20}$$

$$Z_{im,C} = -\frac{1}{\omega C} \tag{21}$$

There are several approaches to plotting the resulting data, but the most useful for the applications in the work is the Nyquist plot, or a plot of the real impedance vs negative imaginary impedance. Figure 3-7 (a) shows a simple circuit and Figure 3-7 (b) shows its Nyquist plot. In actuality, the equivalent circuits are much more complicated with several resistor-capacitor pairs, which can often overlap in the Nyquist plot. Moreover, diffusion can also create an impedance element known as a Warburg impedance. It will result in a

linear relationship with a slope of -1/2 between the real and imaginary impedance.[90] To simplify the interpretation of the EIS spectra, the first intercept (R1) is considered to be the "bulk" resistance, or the resistance through the material, and the difference between the first and second intercept (R2) is considered to be the "polarization" resistance, which is caused by the reactions at the electrode surfaces. For the majority of the EIS performed in this work, only the bulk resistance is considered.

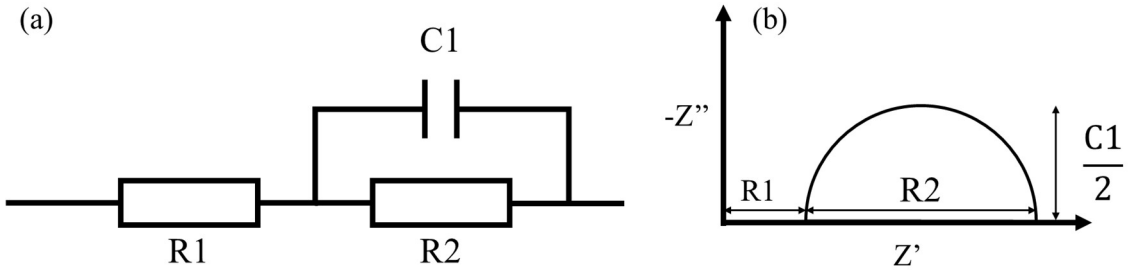

Figure 3-7 A simple circuit (a) and it's equivalent Nyquist plot (b).

3.4.2 Transference Numbers

EIS only provides the total resistance. It does not distinguish between different types of charge carriers. However, for the development of an electrolyte, it is crucial to ensure that the is minimal electronic conductivity. The ratio of the different current carriers is known as the transference number.

The transference number can be determined by exposing each side of the cell to different gasses or different gas concentrations. Figure 3-8 shows a schematic of the testing apparatus for the transference number tests. The different gas composition will induce a voltage across the cell due to the difference in chemical potential. This open circuit voltage can be expressed as:

$$V_{OC} = -\frac{1}{F}\sum_{K}\int_{I}^{II}\frac{t_k}{z_k}d\mu_k^* \quad \textbf{(22)}$$

Where the chemical potential of species *k* is:

$$\mu_k^* = \tilde{\mu}_k + z_k\tilde{\mu}_e \quad \textbf{(23)}$$

$\tilde{\mu}_k$ is the electrochemical potential of species *k*, $\tilde{\mu}_e$ is the electrochemical potential of electrons, t_k is the transference number for species *k*, and z_k is the charge number of species *k*.[91]

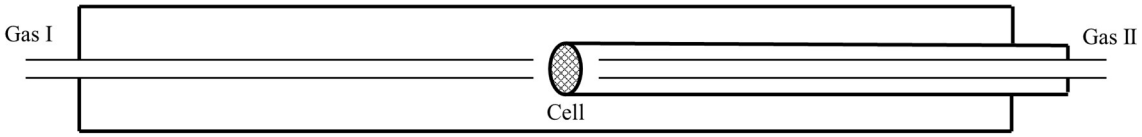

Figure 3-8 Schematic of testing apparatus for transference number tests.

In this work, only the total ionic transference number was determined (ie, the sum of both protons and oxygen ions). The transference number was determined for a hydrogen environment as well as a SOFC operating environment: hydrogen with 3% water on one side and 20% oxygen (air) on the other. For the hydrogen environment, Equation (22) can be solved to the standard Nernst equation shown in Equation (24)

$$V_{OC} = -t_{ion}\frac{RT}{2F}\ln\left(\frac{P_{H_2}^{II}}{P_{H_2}^{I}}\right) \quad \textbf{(24)}$$

For the SOFC operating environment with pure hydrogen on side of the cell and 20% oxygen on the other, we can use the similar Nernst equation for oxygen, shown in Equation (25) The oxygen concentration on the hydrogen side was calculated thermodynamically[70] which has been shown to have good agreement with values measured with a YSZ oxygen sensor.[92]

$$V_{OC} = t_{ion} \frac{RT}{4F} \ln\left(\frac{P_{O_2}^{II}}{P_{O_2}^{I}}\right) \quad \textbf{(25)}$$

3.4.3 Fuel Cell and Electrolysis Cell Testing

Cells were tested by first sealing to an alumina tube support using Aremco Ceramabond 552. The cells were then placed into the testing furnace and heated to 800ºC. Once at temperature, the fuel side of the cell was flushed with argon to remove any oxygen. Next hydrogen with 3% water was introduced to the anode for at least 4 hours to fully reduce the nickel oxide. After reduction, the furnace temperature was reduced to the desired operating temperature. For SOFC testing, the gases were hydrogen with 3% water on the anode and ambient air on the cathode. For steam electrolysis, fuel side gas was hydrogen with 3% water and the oxygen side gas was synthetic air with 12% water. Finally, for CO_2-H_2O co-electrolysis, the fuel side gas was 16% CO_2, 84% H_2 with the gas mixture hydrated to 3% water. The oxygen side gas was syntactic air with 3% water. The voltage and current control were performed by an Arbin potentiostat. Cells were evaluated for their performance through voltage sweeps at 5 mV/second and recording the current response and calculating power produced or required (for electrolysis). Additionally, for electrolysis

cells, the round-trip power efficiency was also calculated. The round-trip power efficiency is the ratio of power in fuel cell mode at a set temperature and current density to the power required to operate in electrolysis mode under the same conditions. Finally, the long-term performance of the reversable fuel cells and electrolysis cells were performed at constant current densities of both 0.5 A/cm^2 and 1 A/cm^2.

CHAPTER 4. A NEW PROTON CONDUCTING BARIUM PEROVSITE ELECTROLYTE BASED ON BARIUM CERATE AND BARIUM HAFATE

4.1 Research Objectives

There has been a shift away from hydrogen operated SOFCs to multi-purpose systems, which can operate on hydrocarbon fuels as well as operate in electrolysis mode to produce a variety of gases including hydrogen, syn-gas, ammonia, and others. However, the current state-of-the-art materials were developed for the hydrogen system and lack stability against contaminates which are becoming more common in the new use-cases, specifically extremely high concentrations of CO_2 and water. There is a need to develop new materials which are stable in these environments but do not hinder device performance. To that end, this chapter will attempt to achieve the following objectives:

1. Develop a new proton conducting material, with higher theoretical stability, through the replacement zirconium with hafnium in the BZCYYb system.
2. Demonstrate the newly developed material's performance as an electrolyte for SOFCs and SOECs.

4.2 Structure and Lattice Parameters of BHCYYb

After it was verified that the $BaHfO_3$-$BaCeO_3$ system was more theoretically stable than that of the $BaZrO_3$-$BaCeO_3$ system, zirconium was replaced by hafnium in the BZCYYb system and it was determined if the new, BHCYYb material would retain the same

structure as BZCYYb. Figure 4-1 shows the XRD of BHCYYb at different hafnium concentrations. The XRD spectrum matches that of a fully cubic perovskite with a space group of $Pm\bar{3}m$. As the hafnium concentration increases, the peaks positions shift to higher two thetas, which indicates a decrease in the lattice parameter. This is as would be expected as hafnium has a smaller ionic radius that cerium; 85 pm for hafnium and 101 for cerium.[72] The lattice parameters were calculated using Rietveld refinement in the HighScore Plus software. When plotted against the concentration of hafnium in the B-site as shown in Figure 4-2, it can be seen the lattice parameters follow a linear relationship in agreement with Vegard's law,[93] further confirming the desired materials were obtained.

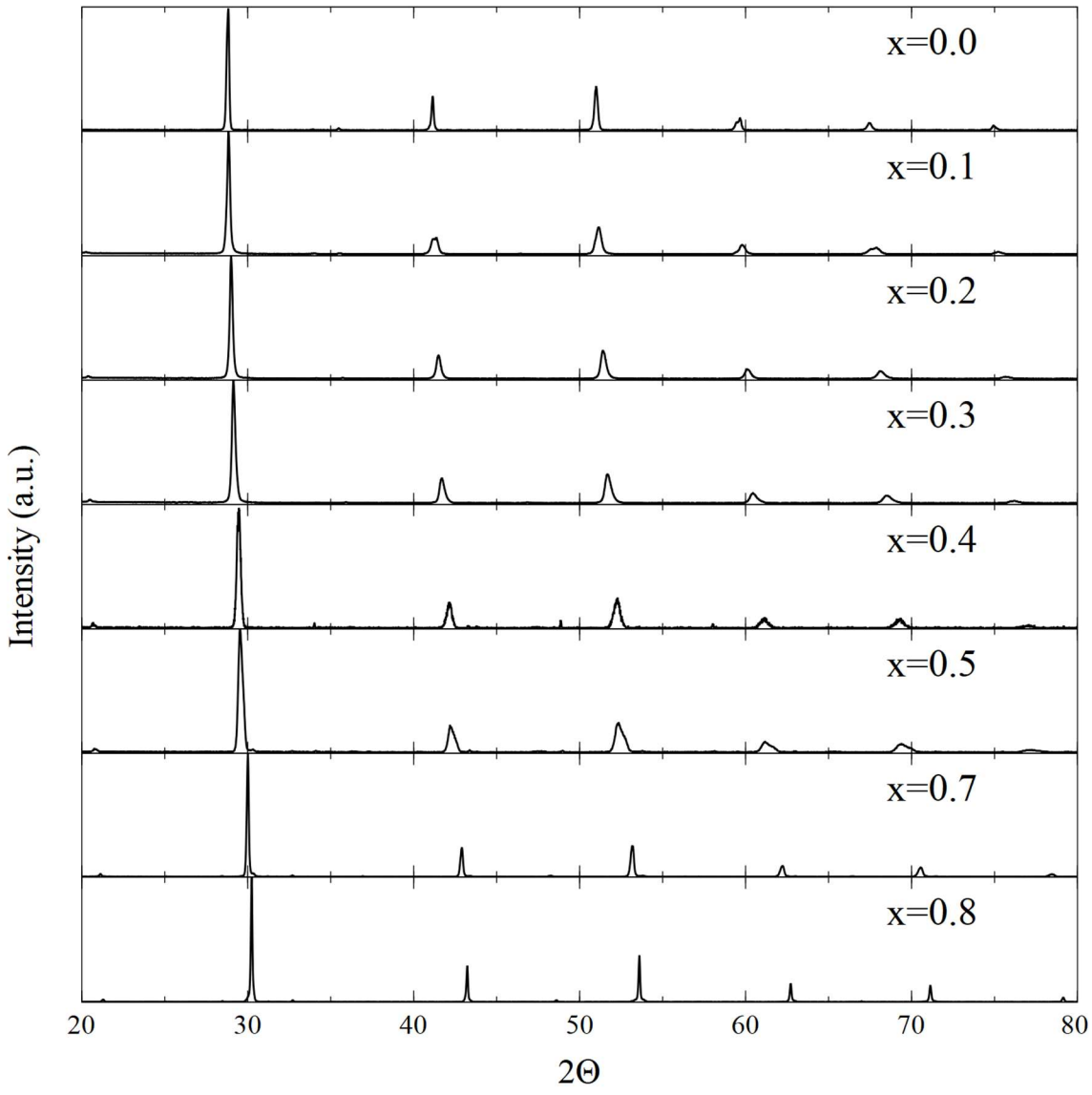

Figure 4-1 X-ray diffraction spectrum of $BaHf_xCe_{0.8-x}Y_{0.1}Yb_{0.1}O_3$ for different concentrations of hafnium.

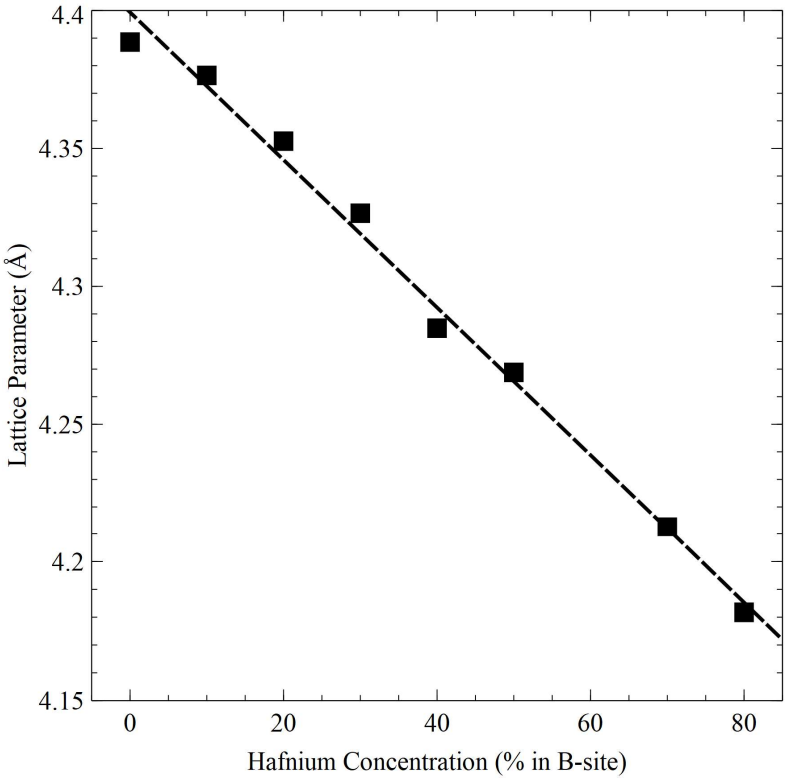

Figure 4-2 Lattice parameters of $BaHf_xCe_{0.8-x}Y_{0.1}Yb_{0.1}O_{3-\delta}$ as a function of hafnium concentration

4.3 Conductivity and Activation Energy

Once the desired material was obtained and the structure was verified to be correct, the conductivity and activation energy needed to be compared to that of the current state-of-the-art material, BZCYYb. Figure 4-3 shows example Nyquist plots of the EIS scans for $BaHf_{0.1}Ce_{0.7}Y_{0.1}Yb_{0.1}O_{3-\delta}$. The conductivity of BHCYYb in 3% H_2O in Ar at different hafnium concentrations is shown in Figure 4-4. The conductivity is inversely proportional to the concentration of hafnium, except for BHCYYb-7111. Interestingly, at higher temperatures BHCYYb-7111 has higher conductivity than BHCYYb-5311 and about the same conductivity as BHCYYb-4411. This is due to the increase in activation energy caused by the higher hafnium concentration. The activation energy is calculated using the

Arrhenius equation for ionic conductivity shown in Equation (26). The Arrhenius equation can be rearranged to match a linear equation with the slope equal to activation energy over the Boltzmann constant shown in Equation (27). The best fit lines and activation energies are shown in Figure 4-5. The activation energy of BHCYYb-7111 is almost twice that of BHCYYb-1711. While the higher activation at high hafnium concentration energy results in higher conductivities at higher temperatures it also results in the conductivity quickly dropping to unacceptable levels at lower temperatures.

$$\sigma = \left(\frac{\sigma_0}{T}\right) \exp\left(-\frac{E_a}{kT}\right) \tag{26}$$

$$\ln(\sigma T) = -\frac{E_a}{K} * \frac{1}{T} \tag{27}$$

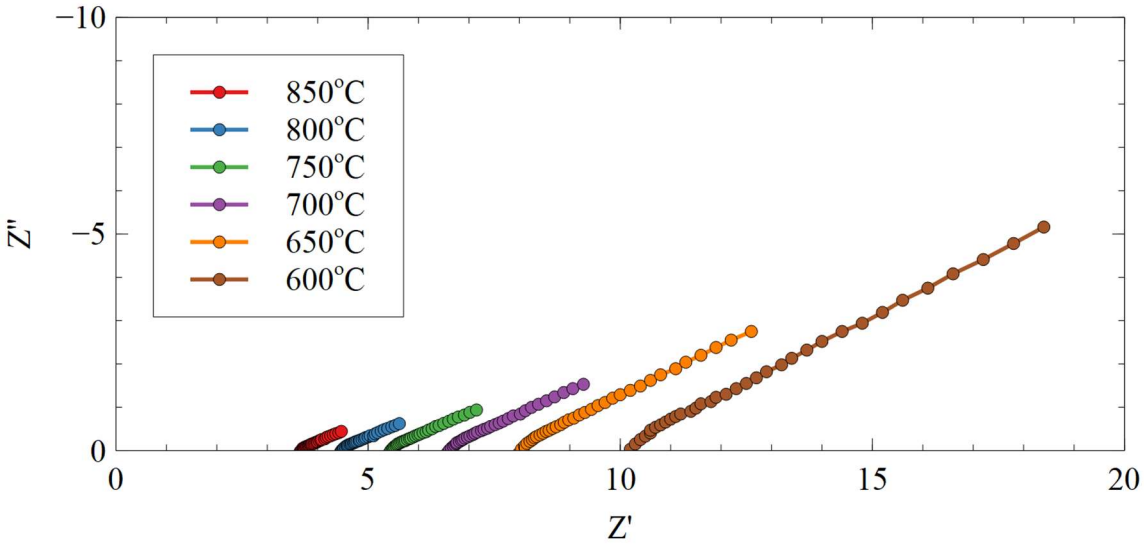

Figure 4-3 Nyquist plots of the impedance spectroscopy of $BaHf_{0.1}Ce_{0.7}Y_{0.1}Yb_{0.1}O_{3-\delta}$ in 3% H_2O in Ar

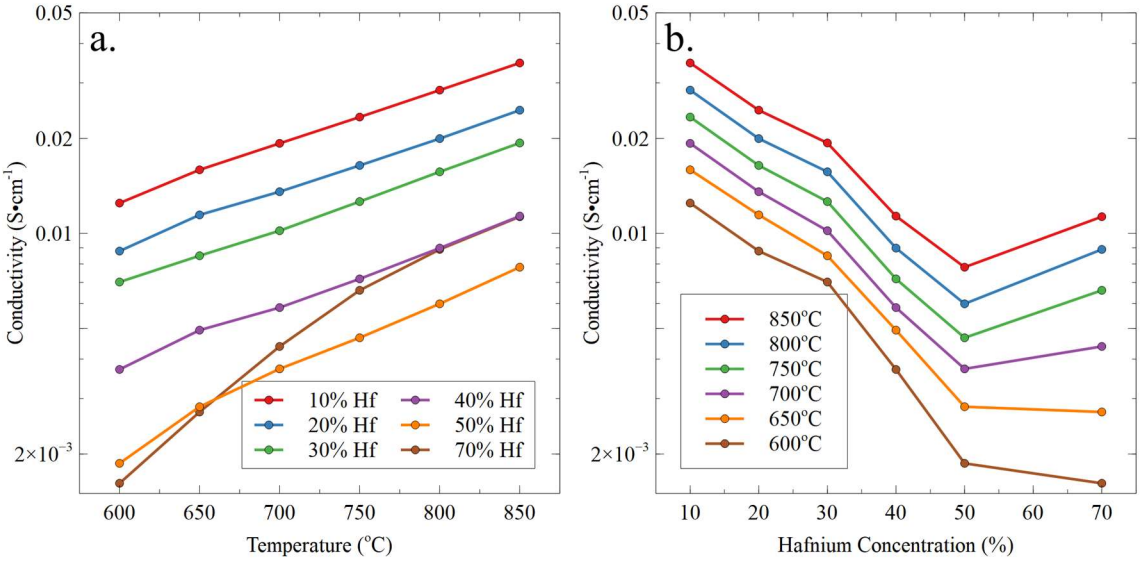

Figure 4-4 Conductivity of $BaHf_xCe_{0.8-x}Y_{0.1}Yb_{0.1}O_{3-\delta}$ in 3% H_2O in Ar as a function of temperature (a) and hafnium concentration (b).

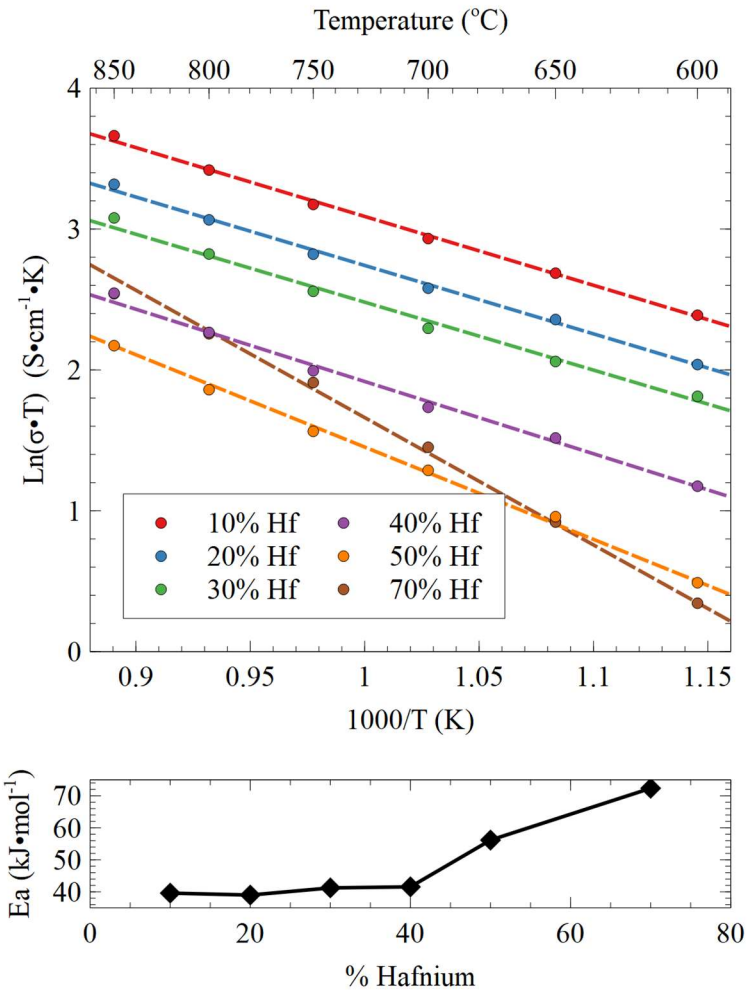

Figure 4-5 Conductivity of $BaHf_xCe_{0.8-x}Y_{0.1}Yb_{0.1}O_{3-\delta}$ in 3% H_2O in Ar plotted according to the Arrhenius equation for ionic conductivity (top) and activation energy of $BaHf_xCe_{0.8-x}Y_{0.1}Yb_{0.1}O_{3-\delta}$ (bottom)

When the conductivity of BHCYYb is compared to the state of the art BZCYYb, shown in Figure 4-6, a couple of interesting trends emerge. First, we see that the activation energy of both BZCYYb and BHCYYb is approximately the same. However, when the conductivity is compared as a function of dopant concentration, we see that at low hafnium or zirconium concentrations, the hafnium doped material outperforms the zirconium doped. As the concentration is increased, the conductivity decreases as would be expected for both

zirconium and hafnium. Yet the hafnium doped version decreases at a higher rate than the zirconium doped version. At 30% doped, both materials have approximately the same conductivity and at high dopant concentrations, the zirconium outperforms that of the hafnium variant.

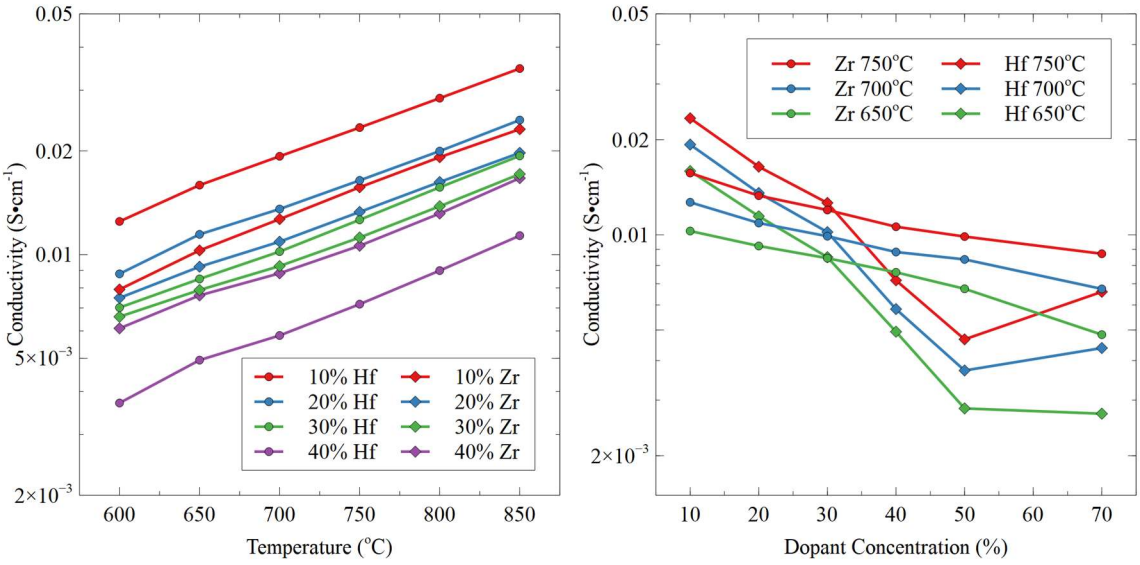

Figure 4-6 Conductivity of $BaZr_xCe_{0.8-x}Y_{0.1}Yb_{0.1}O_{3-\delta}$ (circles) and $BaHf_xCe_{0.8-x}Y_{0.1}Yb_{0.1}O_{3-\delta}$ (diamonds) in argon with 3% H_2O. Left: Conductivity from 10% to 40% hafnium or zirconium as a function of temperature in argon with 3% H_2O. Right: Conductivity as a function of dopant concentration for 650°C, 700°C, and 750°C.

One possible explanation is supported by recent DFT calculations.[94] Conductivity is a function of both the charge carrier concentration and the mobility of those charge carriers. Figure 4-7 (a) shows the proton concentrations of $BaZrO_3$ and $BaHfO_3$ and Figure 4-7 (b) shows the proton jump rates, an analog for mobility. $BaHfO_3$ has a much higher proton concentration but lower proton jump rate. This suggests that hafnium and zirconium effect the charge carrier concentrations and mobilities differently. Hafnium enhances water uptake over zirconium and therefore has a higher charge carrier concentration but, the Hf-

Y-Hf structure traps protons more strongly than the Zr-Y-Zr structure. As the zirconium or hafnium concentration increase, the trapping effect overwhelms the increase in charge carriers resulting in an overall lower conductivity. Moreover, since the trapping effect is stronger in $BaHfO_3$, hafnium will decrease the conductivity more as its concentration is increased.

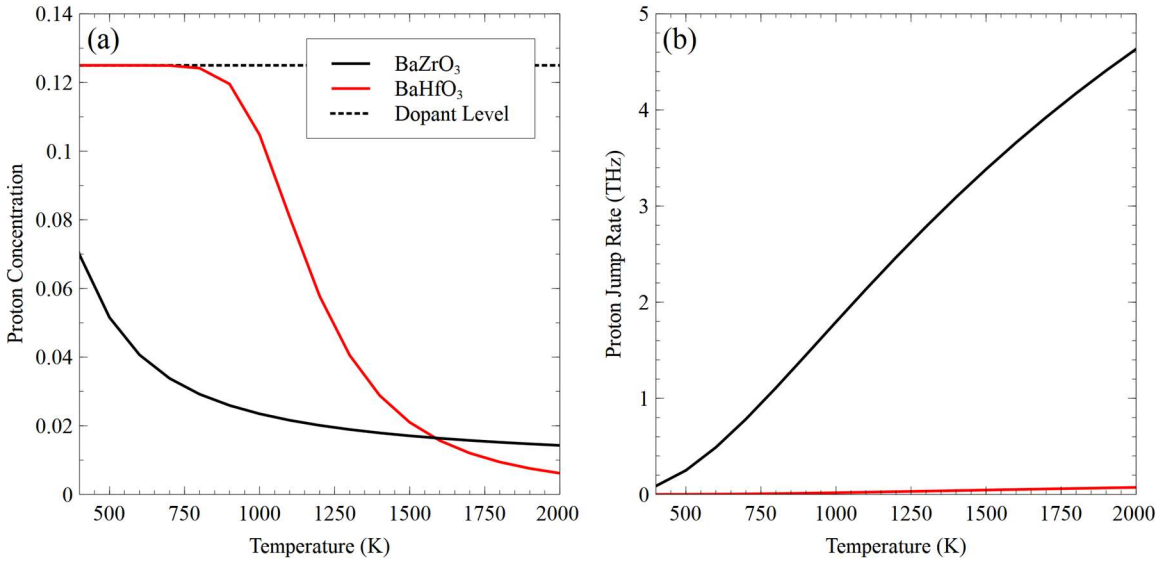

Figure 4-7 Proton concentration (a) and proton jump rate (b) of $BaZrO_3$ and $BaHfO_3$

4.4 Transference Number

As was mentioned above, another important criterion for an electrolyte material in addition to conductivity is its transference number, or ratio of ionic to electronic conductivity. If there is any significant electronic conductivity, the electrolyte cannot effectively separate the anionic and cathodic reactions reducing the overall performance. The transference number of BHCYYb was measured in two different gas environments. First, it was measured in a hydrogen atmosphere (20% and 5% with Ar balance). This is due to

electrolyte materials often being used in a cermet with nickel on the anode side of cells. The ionic transference numbers are shown in Figure 4-8. As the temperature is decreased, the transference number increases. This is common behavior for many ionic conductors and is caused by the intrinsic decrease in bandgap at higher temperatures.[95] Additionally, we see that BHCYYb-1711 has the lowest transference number across temperatures. This is most likely due to the higher reducibility of cerium compared to hafnium, which results in slightly higher electronic conductivity.[96]

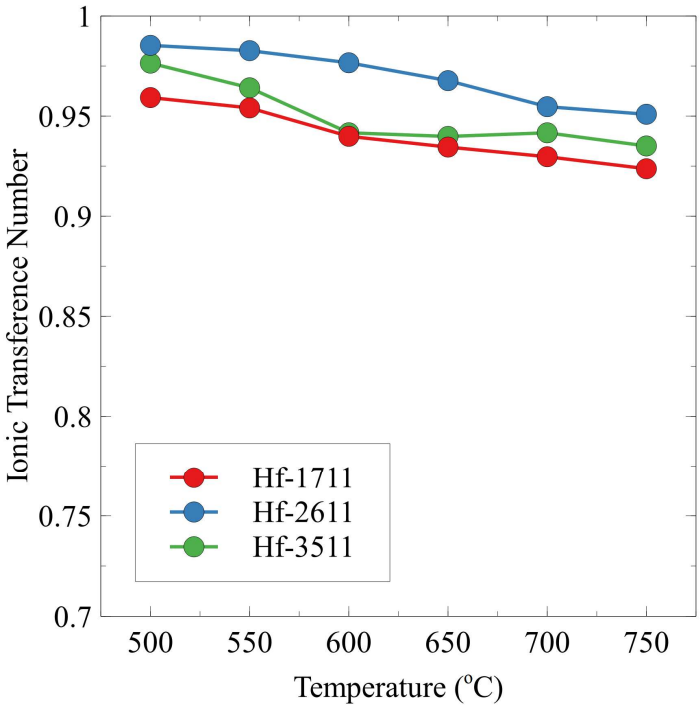

Figure 4-8: Total ionic transference number of BHCYYb in 20% H_2//5% H_2 with argon balance from 500°C to 750°C

In addition to a hydrogen atmosphere, the transference number was also determined for a "SOFC" atmosphere. The SOFC atmosphere represents realistic operating conditions and consists of ambient air on one side of the cell (20% oxygen, 80% nitrogen) and hydrogen with 3% water on the other. The transference number for the SOFC environment is shown

in Figure 4-9. In this case, the expected behavior of a decreasing ionic transference number as the temperature increases is seen, but the decrease is more pronounced. This is most likely caused by the increase in the oxygen partial pressure. At any given temperature, an increase in the oxygen partial pressure will fill the oxygen vacancies created by the trivalent dopants. In order to balance the charge of the filled vacancies, holes must be formed as shown in Equation (28). The holes mobility increases faster with increasing temperature than ionic species so the increase in electronic conductivity is more pronounced at higher temperatures.[95] This is also supported by the ionic transference numbers for $BaCe_{0.95}Y_{0.05}O_3$ which have been shown to be close to ~0.9 in hydrogen atmospheres but ~0.6 in oxygen atmospheres.[91] Finally, we can see that increasing the concentration of hafnium decreases the transference number.

$$\frac{1}{2}O_2 + V_o^{\cdot\cdot} \Rightarrow O_O^X + 2h^{\cdot} \quad \textbf{(28)}$$

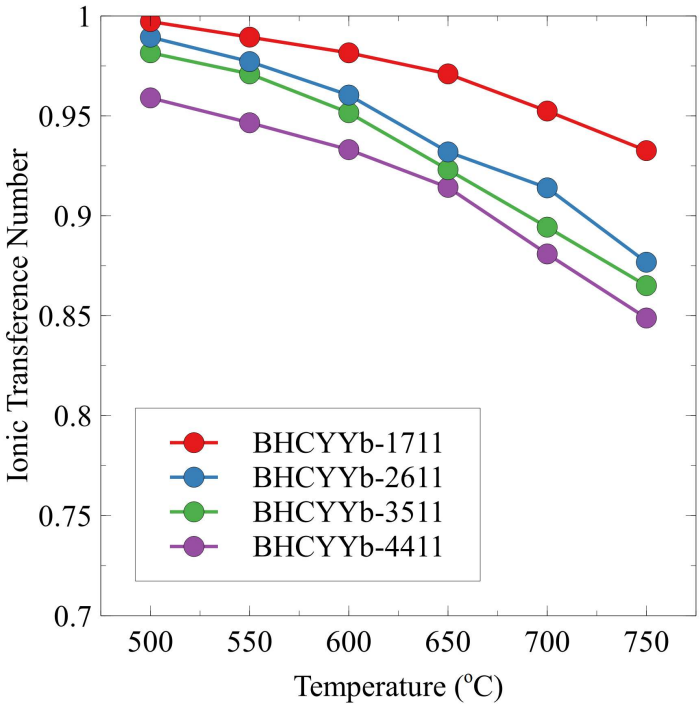

Figure 4-9: Total ionic transference number of BHCYYb in an SOFC environment (H_2 with 3% H_2O//ambient air) from 500°C to 750°C

4.5 Full Cell Performance

Finally, BHCYYb was used to fabricate full cells in order to test its performance under realistic operating conditions. Figure 4-10 shows the current-voltage and power curves for BHCYYb-1711 and BHCYYb-3511 at 700°C and 650°C as well as the EIS curves at those temperatures. BHCYYb-1711 had a peak power density of 1.67 W/cm^2 and 1.45 W/cm^2 at 700°C and 650°C. BHCYYb-3511 had slightly lower performance at 1.37 W/cm^2 and 1.16 W/cm^2 at 700°C and 650°C respectively. The EIS data shows this is due to higher bulk resistance in the BHCYYb-3511 cell while the polarization resistance remains approximately the same. This implies that the lower performance is due to the electrolyte

and not the anode or cathode. BHCYYb-3511 has been shown to have a lower conductivity than BHCYYb-1711 so it would follow that the BHCYYb-3511 cells would have higher bulk resistance. However, while the BHCYYb-3511 does have lower overall performance, the performance is similar to other proton conducing SOFCs reported in literature as shown in Figure 4-11.[60], [61], [97]–[99]

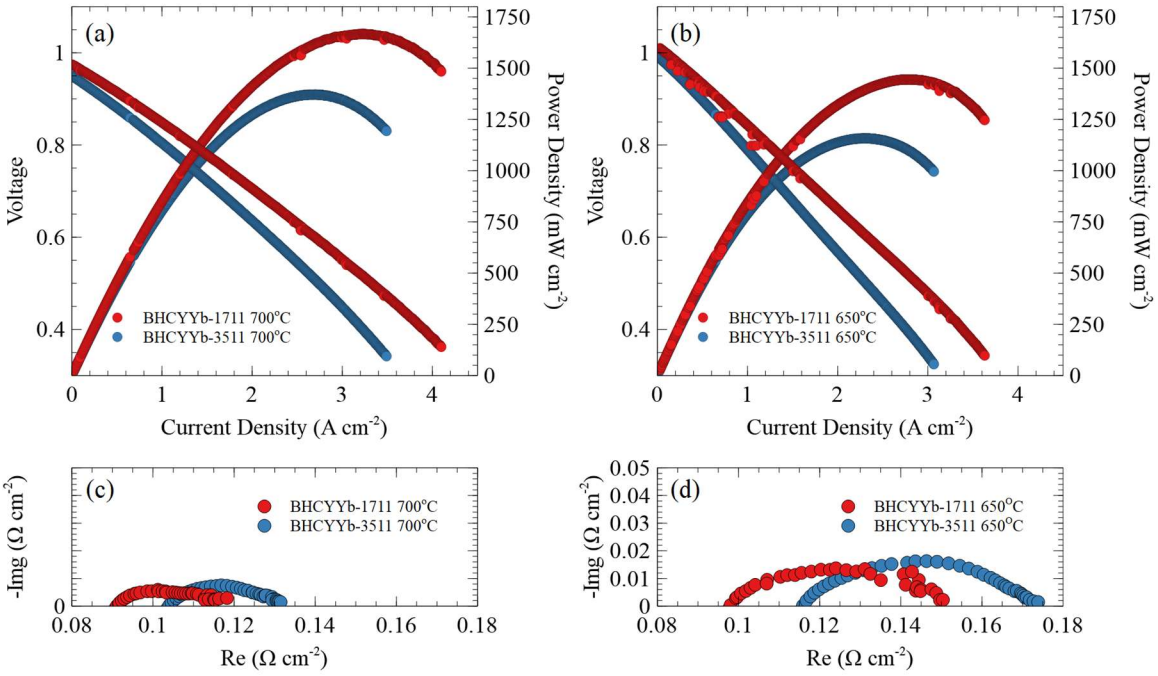

Figure 4-10: (a)-(b) Current-voltage and power curves for BHCYYb-1711 and BHCYYb-3511 at 700°C and 650°C respectively. (c)-(d) Electrochemical impedance spectrometry curves of BHCYYb-1711 and BHCYYb-3511 at 700°C and 650°C respectively.

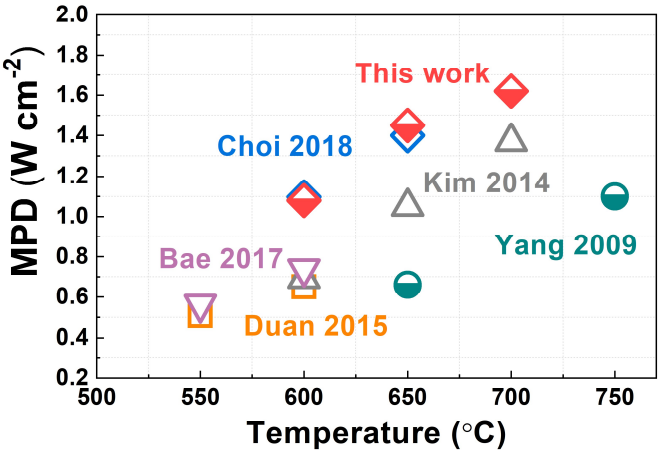

Figure 4-11: Maximum power density of BHCYYb-1711 full cell compared to other high performing proton conducting SOFCs. [60], [61], [97]–[99]

4.6 Conclusions

Thermodynamics has suggested that when zirconium is replaced with hafnium in BZCYYb, the stability should increase. Therefore, a new material family, $BaHf_xCe_{0.8-x}Y_{0.1}Yb_{0.1}O_3$ (BHCYYb) was fabricated. The conductivity and activation energy of this new material was determined to be higher than the current state-of-the-art BZCYYb at low Zr/Hf concentrations (10% and 20%). However, as the Zr/Hf concentrations increased, both BZCYYb's and BHCYYb's conductivity decreased but BHCYYb decreased at a faster rate. This led to the 30% doped BHCYYb and BZCYYb having approximately the same conductivity and BZCYYb had higher conductivity at high Zr/Hf concentrations. In addition to conductivity, the transference number of BHCYYb was measured in hydrogen and in an SOFC condition (air//H_2 with 3% H_2O). At SOFC operating temperatures the transference number was above 0.9. It was shown that as the temperature was increased the transference number dropped as would be expected because of temperature effect on the bandgap. Additionally, a higher hafnium concentration increased the transference

number in hydrogen but decreased in an SOFC condition. Finally, BHCYYb was used to fabricate a full lab-scale fuel cell. The performance of this cell was similar or better to that of current top performing SOFCs in literature. However, as hafnium was increased, the performance of the cells decreased due to the decrease in bulk conductivity. Overall, BHCYYb has been shown to be an excellent proton conducting electrolyte with performance similar to current state-of-the-art materials.

CHAPTER 5. IMPROVED STABILITY OF BARIUM PEROVSKITES BY REPLACEMENT OF ZIRCONIUM WITH HAFNIUM

5.1 Research Objectives

In the previous chapter, a new material was developed and tested as an electrolyte for SOFCs and SOECs. However, this development was predicated on the notion that the replacement of zirconium with hafnium would improve the stability of the material. Theoretical calculations indicate that this material should have the increased stability, but those calculations were based on implied models in pure gas environments and it is important to test new materials in realistic conditions as there are often differences between simplified models and realistic operating conditions. Therefore, this chapter will attempt to meet the following objectives:

1. Evaluate the long-term stability of the newly developed BHCYYb electrolyte material in realistic operating conditions.
2. Identify the degradation mechanisms of barium perovskite proton conducting electrolytes in realistic operating conditions.

5.2 Stability Verification Through TGA

To initially test the stability of the new BHCYYb material in comparison to BZCYYb, TGA was performed in pure CO_2. CO_2 was chosen over H_2O for two reasons: firstly, both BZCYYb and BHCYYb are theoretically more reactive to CO_2 than H_2O; secondly, H_2O

is very difficult to introduce into a TGA as the phase change from liquid to vapor can disrupt the very sensitive mass measurements. Figure 5-1 shows the weight gain of the BZCYYb (a) and BHCYYb (c) as it reacts with the CO_2 to form $BaCO_3$ and CeO_2. Figure 5-1 (b) and (d) show the derivatives of the cooling curves with the peaks representing the temperature at which the material becomes unstable. The TGA confirms that BZCYYb and BHCYYb are more stable at higher temperatures. It also shows that BHCYYb is more stable than BZCYYb. At 10% dopant concentration, both BZCYYb and BHCYYb degrade quite significantly. At 20%, they both again degrade but we start to see that BHCYYb degrades to a lesser extent. Moreover, the derivative peaks for BHCYYb are broader and less intense, indicating the degradation reaction rate is slower. Finally, at 30%, BHCYYb is completely stable, with a slight decrease in weight due to intrinsic vacancy formation, while BZCYYb still degrades. This shows that hafnium doped BHCYYb has a higher stability that BZCYYb against CO_2.

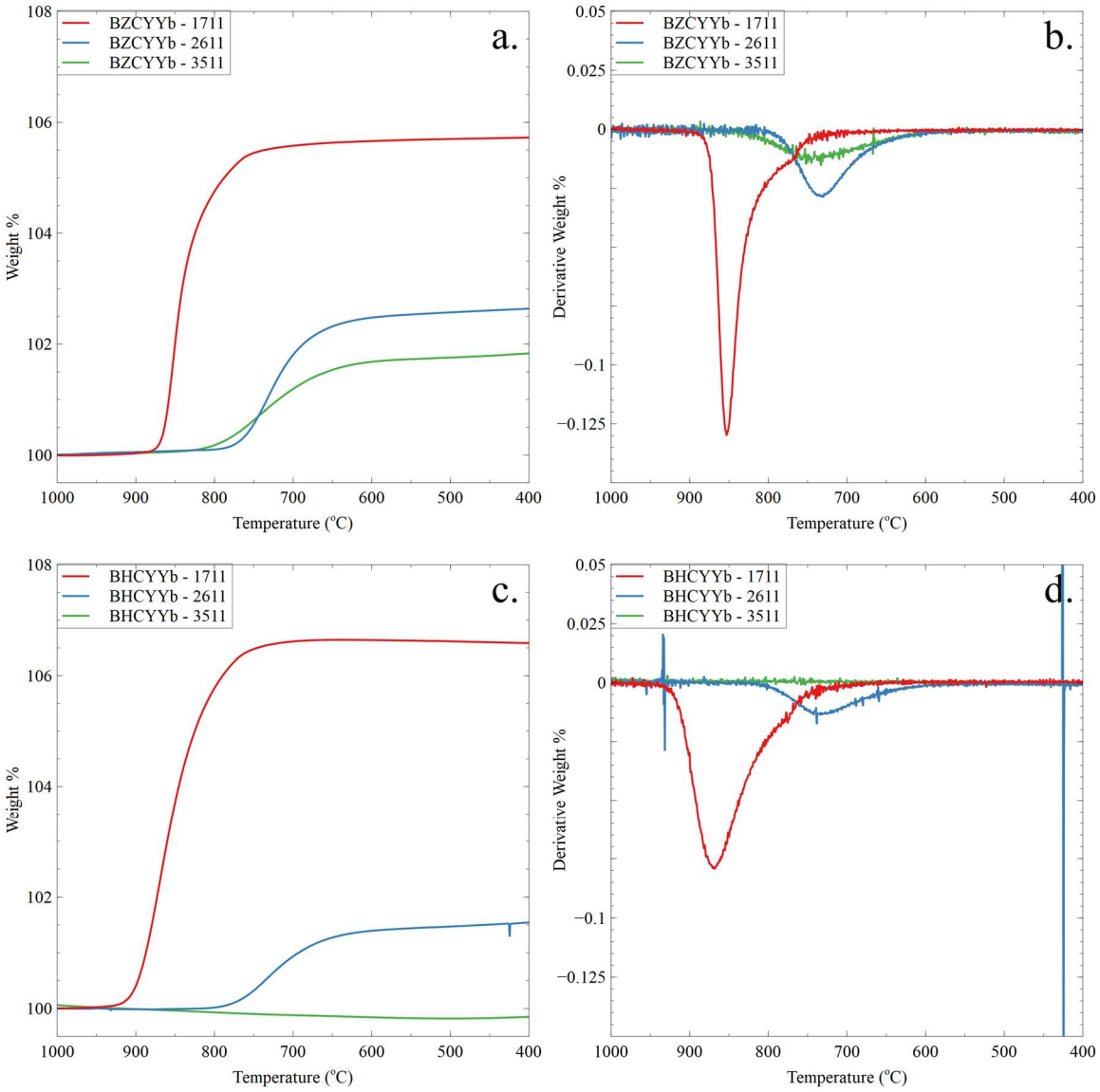

**Figure 5-1 Thermogravimetric analysis of $BaHf_xCe_{0.8-x}Y_{0.1}Yb_{0.1}O_{3-\delta}$ (a) and $BaZr_xCe_{0.8-x}Y_{0.1}Yb_{0.1}O_{3-\delta}$ (c) powders cooled in pure CO_2 from 1000°C to 400°C. The derivatives of the cooling curves are shown in (b) and (d) **

In order to identify the degradation phase, Raman spectroscopy was performed on the powders after the TGA tests and the spectra are shown in Figure 5-2. There are several peaks present in the Raman spectra. The peaks at 693 cm^{-1}, 1060 cm^{-1}, and 1423 cm^{-1}can be attributed to barium carbonate.[100] The peaks at 470 $cm^{-1}$and 1175 cm^{-1}can be attributed to CeO_2.[101] Most likely the CeO_2 phase is a solid solution between CeO_2 and

ZrO_2 or HfO_2 respectively. Moreover, the yttrium and ytterbium are most likely in the fluorite phase. This is supported by the shoulder on the 693 cm^{-1} peak.[102] The broad peak at ~600 cm^{-1} can be attributed to the perovskite phase.[103] In addition to identifying the degradation phases as $BaCO_3$ and CeO_2, the Raman also verifies the hafnium-based material is more stable than the zirconium-based material. For the 30% zirconium doped material, there is clearly a $BaCO_3$ peak present at 1060 cm^{-1} but no peak is present in the 30% hafnium doped material.

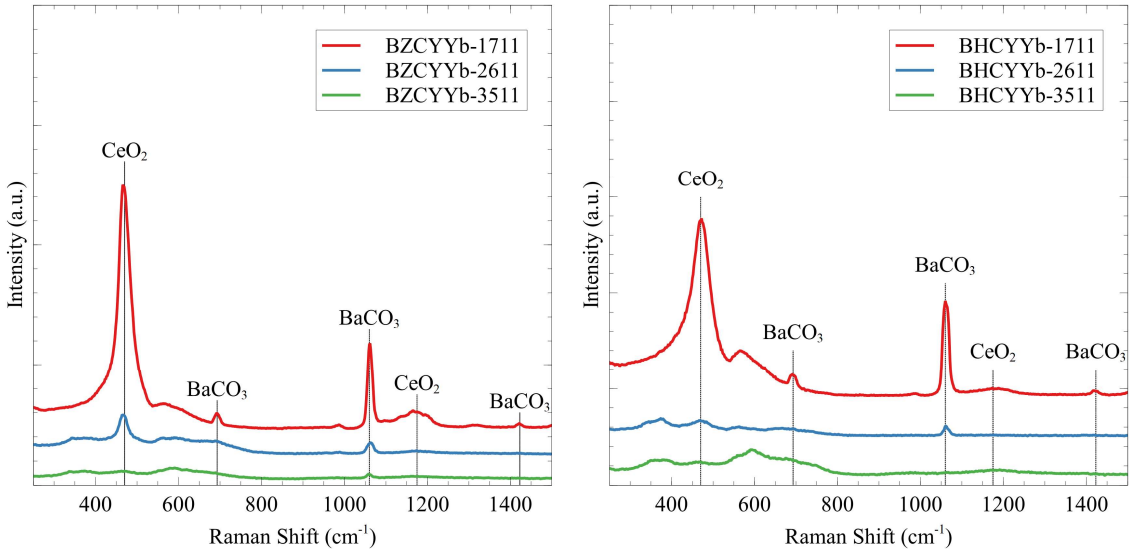

Figure 5-2 Raman spectra of BHCYYb and BZCYYb powders after TGA analysis in CO_2. $BaCO_3$ and CeO_2 peak positions are shown.

5.3 Long-Term Chemical Stability

After the TGA analysis it was obvious hafnium had potential to improve stability. However, evaluation under more real-world conditions was needed. In addition to CO_2, water is very common in proton conducting electrolytes. Therefore, the stability of BHCYYb was compared to that of BZCYYb after long term exposures to both CO_2 and

water independently and together. XRD and Rietveld refinement was used to determine the extent of degradation after exposure as described earlier. The results for of the refinement are tabulated in Table 5-1 and Table 5-2.

Figure 5-3 and Figure 5-4 show the XRD patterns of BHCYYb and BZCYYb respectively after exposure to 25% CO_2 in argon at 700 ^oC for 500 hours. The results match those from the TGA analysis. Both 10% hafnium and 10% zirconium degrade significantly. At 20% the difference is more significant with BHCYYb only degraded 28% where as BZCYYb degraded 66%, again showing that BHCYYb is more stable. Finally, at 30% and 40% dopant concentrations, both BHCYYb and BZCYYb showed minimal degradation, within the resolution of the XRD analysis.

Figure 5-5 and Figure 5-6 show the XRD patterns of BHCYYb and BZCYYb respectively after exposure to 25% H_2O in argon at 700 ^oC for 500 hours. There does not appear to be any detectable degradation form water along to either BHCYYb or BZCYYb at any dopant concentration. This is in line with the thermodynamic predictions carried out earlier which suggested that barium perovskites are more susceptible to CO_2 degradation than they are to water. The boiling point of $Ba(OH)_2$ is 780^oC so it is possible that barium hydroxide is formed but is not seen in the x-ray diffraction due to evaporation. However, if this was occurring at high rates, CeO_2 would be expected to be present in the finial x-ray diffraction patterns. The absence of CeO_2 indicates that any formation of $Ba(OH)_2$ is minor. Due to the lack of obvious degradation, Rietveld refinement was not carried out on these samples.

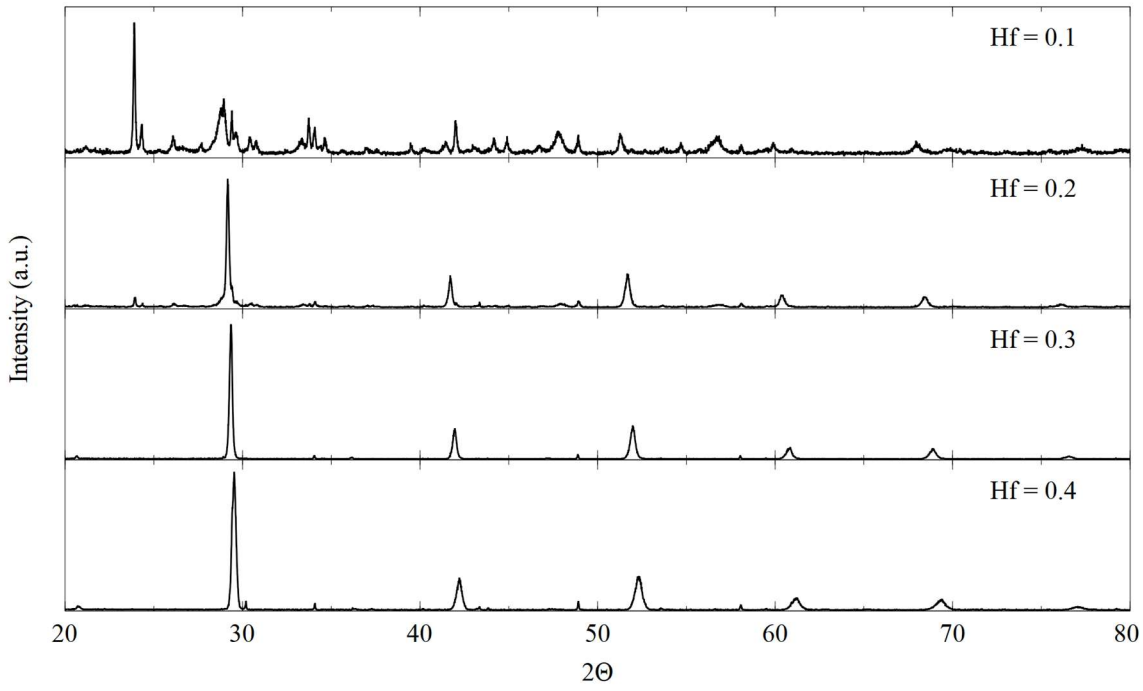

Figure 5-3 X-ray diffraction patterns of dense $BaHf_xCe_{0.8-x}Y_{0.1}Yb_{0.1}O_{3-\delta}$ pellets after exposure to 25% CO_2 75% Ar at 700°C for 250 hours.

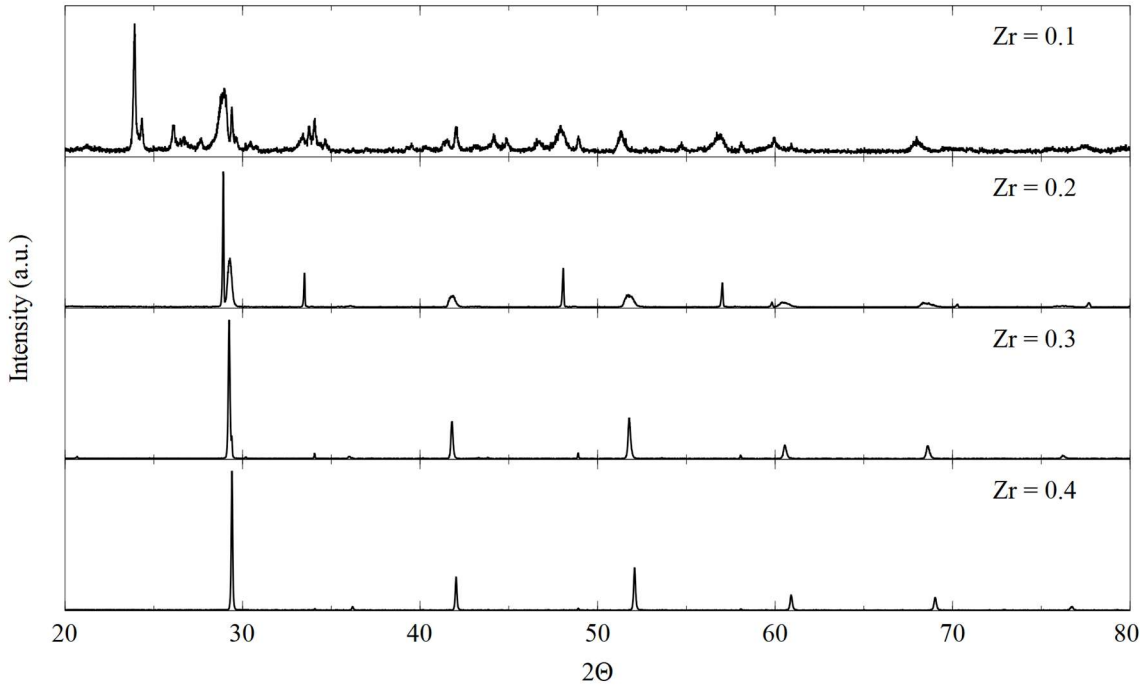

Figure 5-4 X-ray diffraction patterns of dense $BaZr_xCe_{0.8-x}Y_{0.1}Yb_{0.1}O_{3-\delta}$ pellets after exposure to 25% CO_2 75% Ar at 700°C for 250 hours.

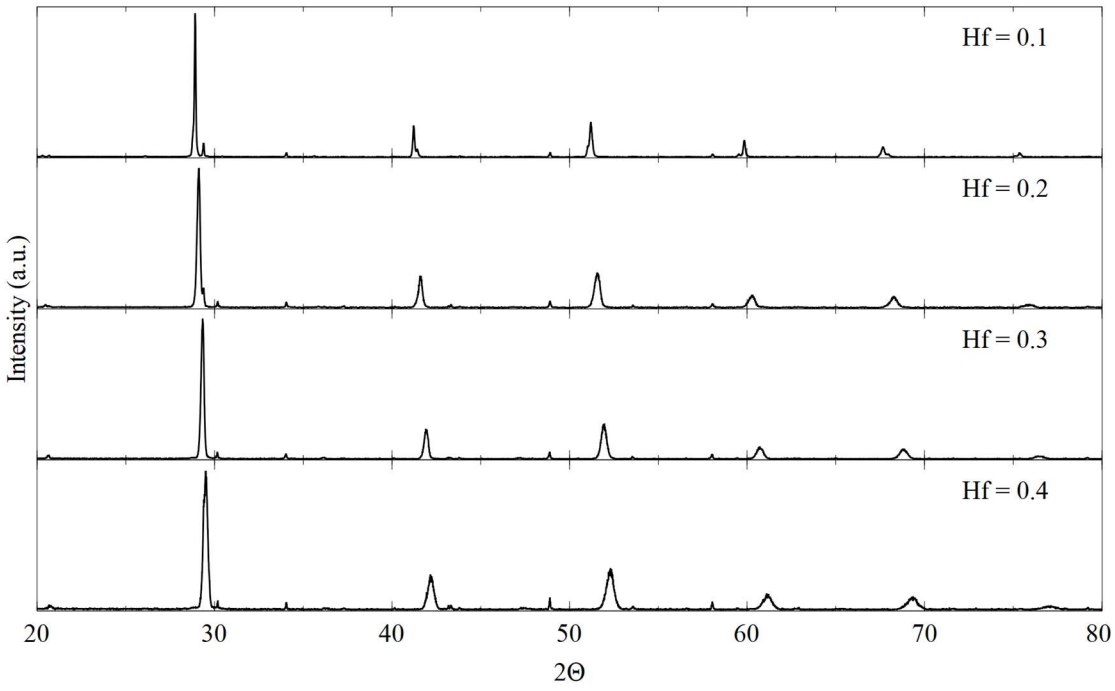

Figure 5-5 X-ray diffraction patterns of dense $BaHf_xCe_{0.8-x}Y_{0.1}Yb_{0.1}O_{3-\delta}$ pellets after exposure to 25% H_2O 75% Ar at 700°C for 250 hours.

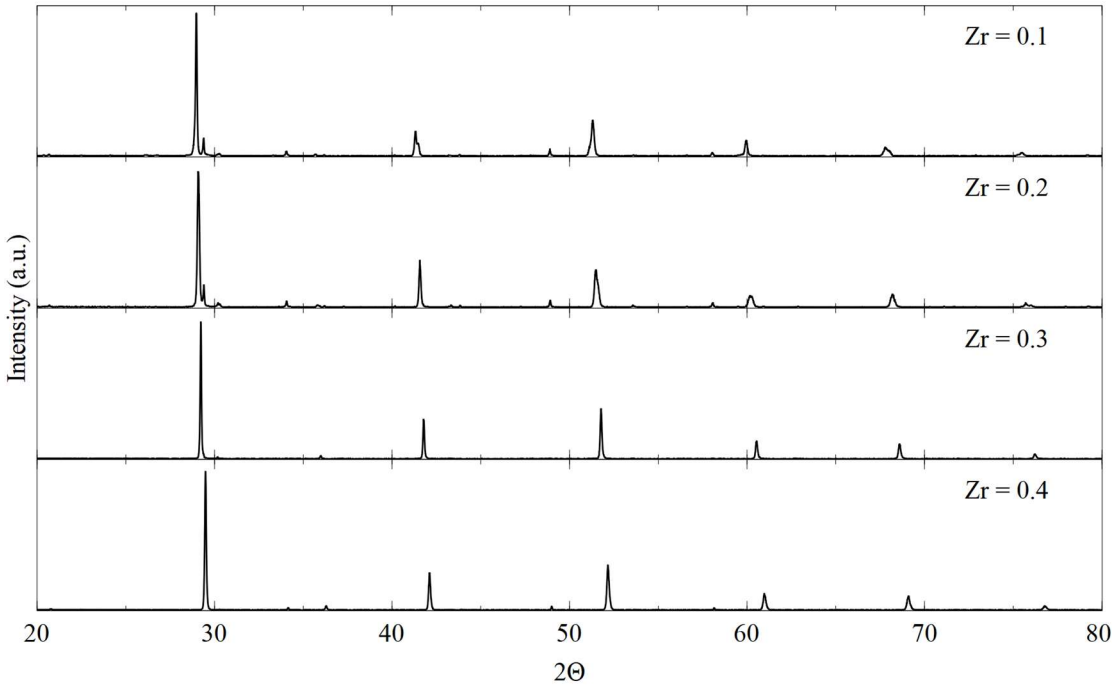

Figure 5-6 X-ray diffraction patterns of dense $BaZr_xCe_{0.8-x}Y_{0.1}Yb_{0.1}O_{3-\delta}$ pellets after exposure to 25% H_2O 75% Ar at 700°C for 250 hours.

Finally, Figure 5-7 and Figure 5-8 show the XRD patterns of BHCYYb and BZCYYb respectively after exposure to 25% CO_2, 25% H_2O, and 50% H_2 at 700 ^oC for 500 hours. The degradation follows the same trend as with the 25% CO_2 in argon but in all cases, the degradation is more severe. One possible explanation is a synergistic effect between the water and CO_2. While the reaction of barium perovskites with water is not thermodynamically favourable, it is possible that the high water concentration is driving the formation of a small amount of $Ba(OH)_2$. The concentration of water would be further increased by the reduction of CO_2 to CO by the hydrogen as show in Figure 5-9. The increased water concentration would further drive the formation of $Ba(OH)_2$ through Le Chatelier's principle. Finally, the reaction of $Ba(OH)_2$ with CO_2 to form $BaCO_3$ is very energetically favourable. This reaction with CO_2 removes the $Ba(OH)_2$ from the system driving further production of additional $Ba(OH)_2$ and accelerating the degradation. Another possible explanation which is less straightforward is a synergistic effect between the CO_2 and hydrogen. Hydrogen is known to reduce cerium in BZCYYb and BHCYYb as was shown with the transference number measurements. Either this reduction or the resulting increase in oxygen vacancies may cause increased degradation. However, further long-term studies and computer simulations are needed to fully understand the degradation mechanism.

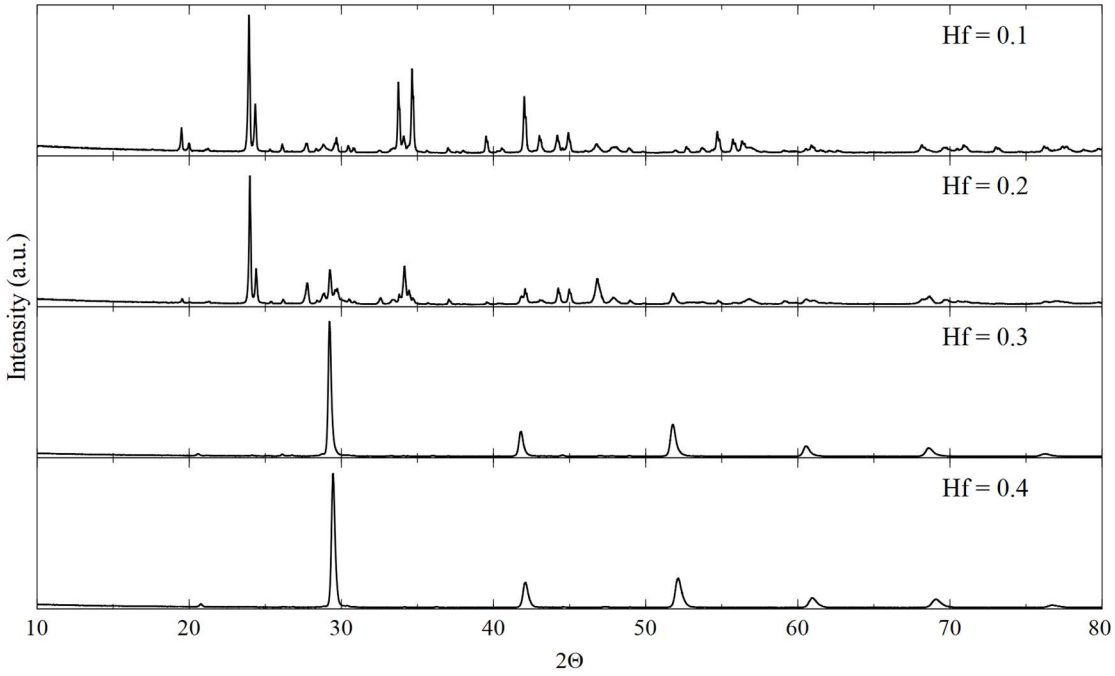

Figure 5-7 X-ray diffraction patterns of dense $BaHf_xCe_{0.8-x}Y_{0.1}Yb_{0.1}O_{3-\delta}$ pellets after exposure to 50% H_2 25% CO_2 & 25% H_2O at 700°C for 500 hours.

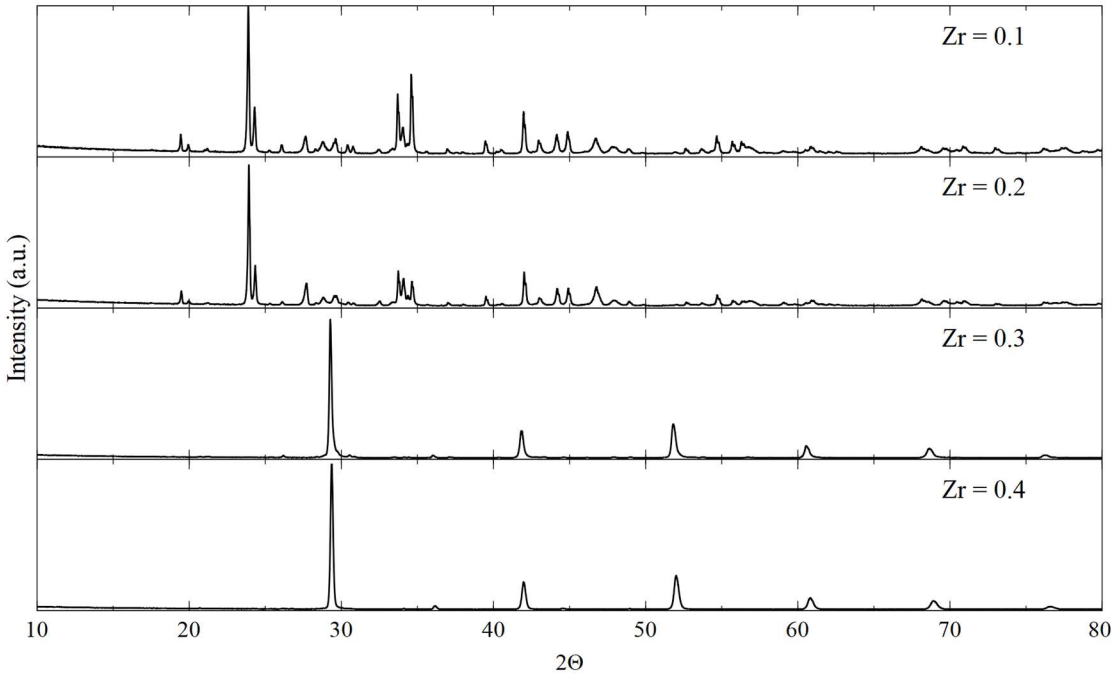

Figure 5-8 X-ray diffraction patterns of dense $BaZr_xCe_{0.8-x}Y_{0.1}Yb_{0.1}O_{3-\delta}$ pellets after exposure to 50% H_2 25% CO_2 & 25% H_2O at 700°C for 500 hours.

Table 5-1 Weight percent of the degradation phases present in BHCYYb after exposure to degradation conditions as determined by Rietveld refinement.

Concentration of Hf in B-site	0.1	0.2	0.3	0.4
25% CO_2 in Ar	84.2%	28.0%	1.5%	3.5%
25% CO_2, 25% H_2O, & 50% H_2	100%	80.1%	7.6%	1.1%

Table 5-2 Weight percent of the degradation phases present in BZCYYb after exposure to degradation conditions as determined by Rietveld refinement.

Concentration of Zr in B-site	0.1	0.2	0.3	0.4
25% CO_2 in Ar	84.1%	65.6%	1.2%	2.0%
25% CO_2, 25% H_2O, & 50% H_2	99.9%	93.5%	9.9%	0.2%

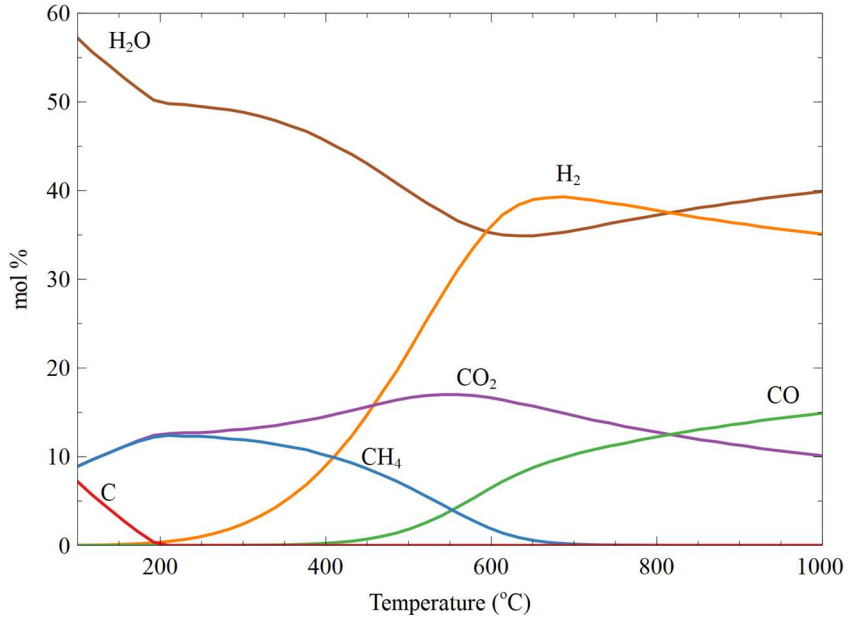

Figure 5-9 Thermodynamic equilibrium concentration of gasses of a 25% CO_2, 25% H_2O, 50% H_2 starting gas mixture.[70]

5.4 Long-Term Conductivity Under Degradation Conditions

Once the long-term chemical stability was determined, the long-term conductivity was tested. Figure 5-10 shows the conductivity of BHCYYb and BZCYYb with 10%, 20%, 30%, and 40% conductivity over the course of 500 hours when exposed to 25% CO_2, 25% H_2O, and 50% H_2 at 700ºC. We can see that at 10% for both zirconium and hafnium, the conductivity rapidly decreases over the first 100 hours. While the degradation rate does slow after the initial 100 hours, it does continue for the remainder of the test. At 20% we again see both BHCYYb and BZCYYb degrade, although at slower rates than the 10%. The degradation is steadier throughout the test, rather than an initial sharp decrease. At 30% we see that the both BZCYYb and BHCYYb appear very steady throughout the test. BHCYYb appears to have a higher conductivity throughout the test but based on the results presented earlier in Figure 4-6 BHCYYb and BZCYYb at 30% dopant level should have similar initial conductivities. It is possible that there was some initial degradation in the zirconium sample, which was not captured in the first datapoint, or the BZCYYb sample used in this test has unusually low conductivity. Finally, at 40% dopant concentration, both materials are very steady throughout the entire 500 hours, but their conductivity is lower than that of the 30% samples.

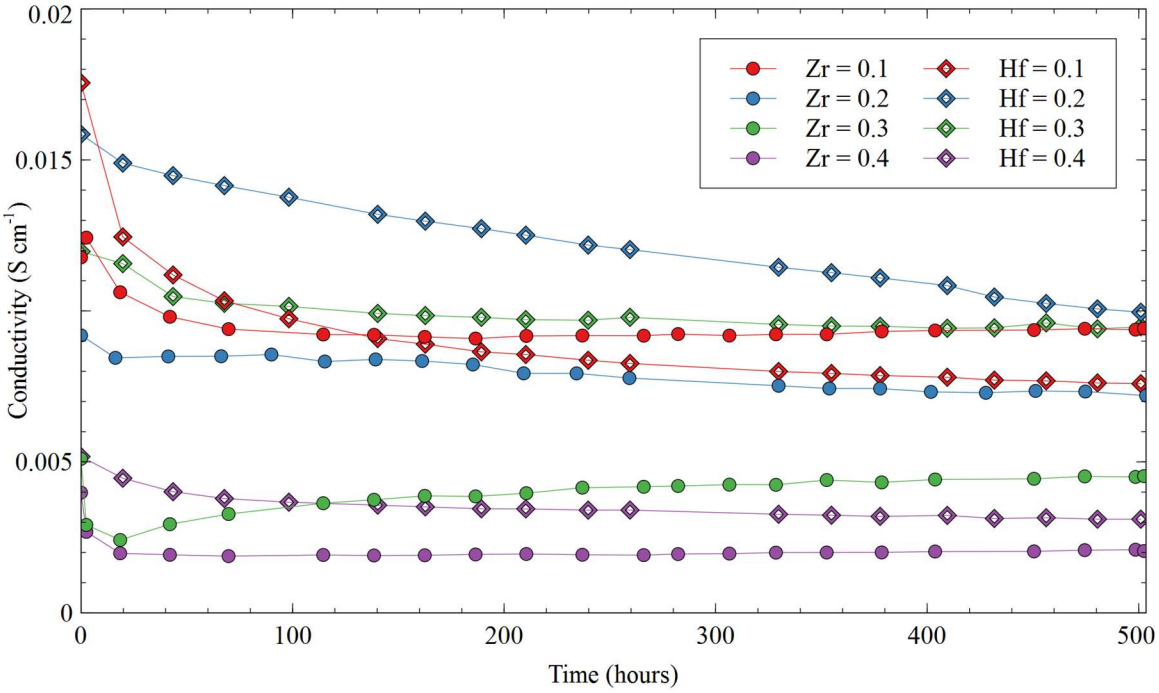

Figure 5-10 Conductivity of BHCYYb and BZCYYb over 500 hours when exposed to 25% CO_2, 25% H_2O, and 50% H_2

5.5 Electrolysis Performance

Lastly, the performance of BHCYYb was tested as an electrolyte for electrolysis operation. Electrolysis requires high concentrations of water, for hydrogen production, and/or carbon dioxide, for syn gas production. The first tests were on steam electrolysis to produce hydrogen. Cells were fabricated with BHCYYb-3511 as the electrolyte and PBSCF as the cathode. The current voltage curves for an electrolysis cell with humidified hydrogen on the fuel side and 3% H_2O on the air side are shown in Figure 5-11. The round-trip power efficiencies at 0.5 A/cm^2 are 88%, 85%, and 79% at 700°C, 650°C, and 600°C respectively. The round-trip efficiencies are slightly lower at 1 A/cm^2. They are 78%, 72%, and 62% at 700°C, 650°C, and 600°C respectively.

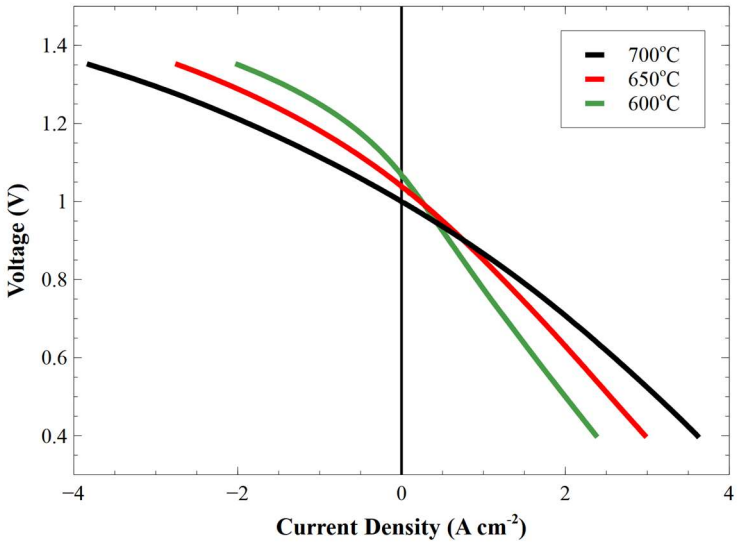

Figure 5-11 Current-voltage curves for an electrolysis cell with BHCYYb-3511 as the electrolyte at 700°C, 650°C, and 600°C with H_2 on the fuel side and air on the oxygen side, both gases contained 3% H_2O.

Once the initial performance had been established, the long-term stability of the cell needed to be tested. Two different stability tests were conducted. First a reversable fuel cell test where the cell was cycled between SOFC and SOEC mode every two hours at 0.5 A/cm^2 and 600°C shown in Figure 5-12(a). A small amount of degradation was observed in fuel cell operation, but that degradation did not affect the electrolysis performance, which was stable throughout the test. Additionally, the material was tested in electrolysis mode for over 1000 hours at 1 A/cm^2. The long-term stability, shown in Figure 5-12(b) was shown to be very stable with little to no degradation over the entire 1000 hours.

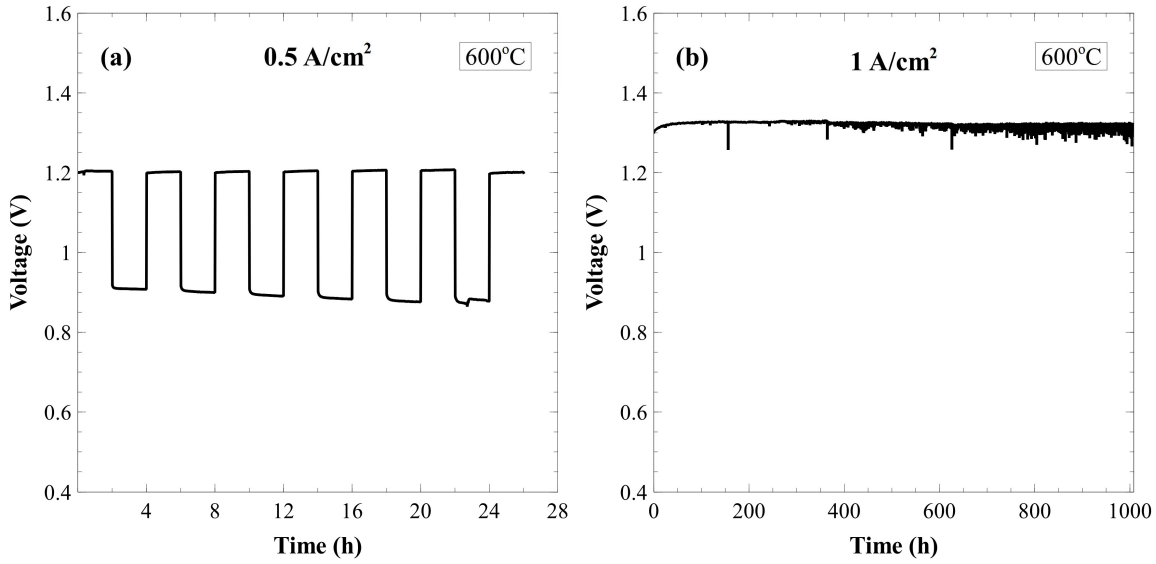

Figure 5-12 (a) BHCYYb-3511 cell tested as a reversible fuel cell at 0.5 A/cm^2, alternating between SOFC and SOEC operation every 2 hours. (b) long term stability tests of BHCYYb-3511 based electrolysis cell tested at 1 A/cm^2 and 0.5 A/cm^2.

Lastly, the performance of BHCYYb was tested as an electrolyte for CO_2-H_2O co-electrolysis. Co-electrolysis is used to produce syn-gas ($CO+H_2$) which is used for most modern chemical production. It could also provide a more economically viable method of carbon capture at fossil fuel power plants. Based on the stability tests performed previously, it was known that BHCYYb is quite stable against water, so the high stability seen in the steam electrolysis was expected. However, BHCYYb is much more susceptible to carbon dioxide, especially at low hafnium concentrations. Therefore, stability was tested for both BHCYYb-1711 and BHCYYb-3511. Figure 5-13(a) shows the current voltage curves of the cell in 16% CO_2 in hydrogen (gas mixture humidified to 3% water) on the fuel side and humidified air on oxygen size. Figure 5-13(b) shows the long-term performance for CO_2-H_2O co-electrolysis using BHCYYb-3511 as the electrolytes at 600°C and 0.5 A.cm^2 and that is compared to cells with BZCYYb-1711 and BZCYYb-

3511 used as the electrolyte. We can see that both BZCYYb based cells degraded within 50 hours while the BHCYYb cell is stable for close to 100 hours.

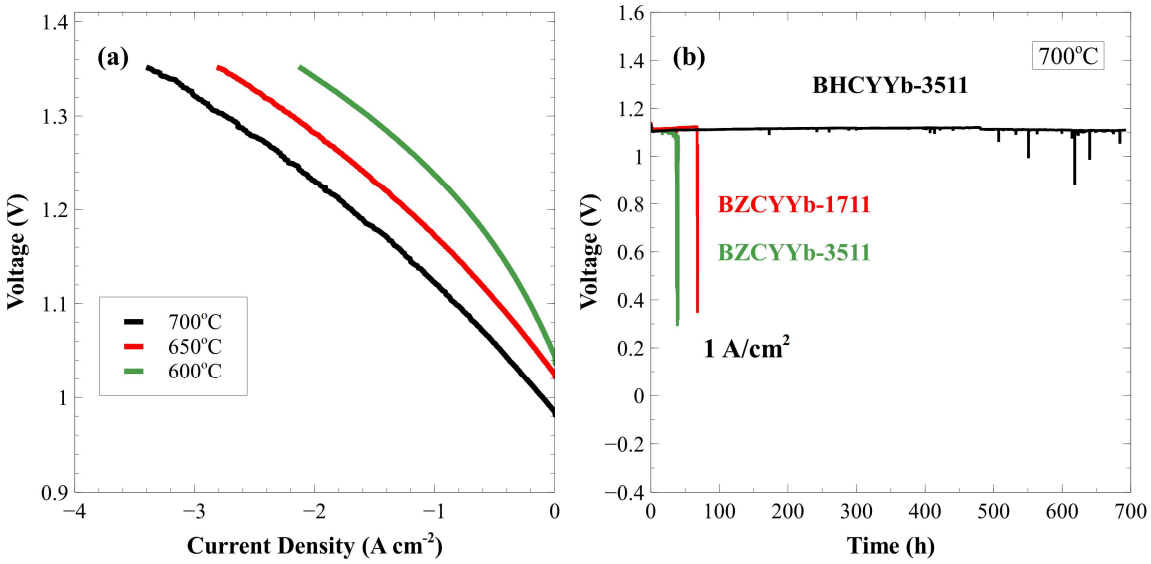

Figure 5-13 (a) Current-voltage curves of BHCYYb-3511 as the electrolyte for CO_2-H_2O co-electrolysis. (b) Long-term performance of BHCYYb-1711 and BHCYYb-3511 as electrolytes for CO_2-H_2O co-electrolysis at 600°C and 0.5 A/cm^2.

5.6 Conclusions

Overall, $BaHf_xCe_{0.8-x}Y_{0.1}Yb_{0.1}O_{3-\delta}$ appears to have slightly higher stability than that of $BaZr_xCe_{0.8-x}Y_{0.1}Yb_{0.1}O_{3-\delta}$ and 30% hafnium is needed to stabilize the material at any concentration of CO_2, but 40% zirconium is needed. The initial TGA results showed that at a 30% dopant level, BHCYYb is completely stable in CO_2 with no barium carbonate formation while BZCYYb does form a small amount of barium carbonate. The long-term chemical stability tests showed again that BHCYYb is more stable than BZCYYb with less degradation at the same dopant levels. The long-term tests also revealed the degradation products and mechanism. When the conductivity of BHCYYb and BZCYYb were tested in realistic operating conditions, the conductivity trend matches that of the chemical

stability. 10% and 20% BHCYYb and BZCYYb both degrade with 20% degrading at a slower rate. At 30% both BHCYYb and BZCYYb appear relatively stable with little to no degradation but BHCYYb shows a higher conductivity, indicating it would outperform BZCYYb in high CO_2 environments.

Both Raman spectroscopy and XRD showed that the major degradation products were $BaCO_3$ and doped CeO_2. It was shown water has little to no degradation effect at any level of doping, but CO_2 significantly degrades the 10% and 20% doped samples. However, when samples are exposed to realistic operating conditions with CO_2, H_2O and H_2, the degradation is exacerbated, but with the same degradation products. This is possibly due to the formation of CO, a much more reactive species than CO_2.

Finally, BHCYYb was used as an electrolyte material for reversable fuel cell and SOEC operation. The round-trip efficiency for hydrogen was 79% at 0.5 A/cm^2 at 600ºC which is comparable to similar cells made from BZCYYb and the same is true at higher current densities and higher temperatures. In CO_2-H_2O co-electrolysis, BHCYYb-3511 continues to perform well, with stable performance up to 700 hours. When compared to BZCYYb-1711 and BZCYYb-3511 the performance is approximately the same within experimental error. However, both BZCYYb cells degrade within the first 50-100 hours while the BHCYYb-3511 cell is stable for up to 700 hours.

CHAPTER 6. DOPANTS IN THE BARIUM HAFNATE SYSTEM

6.1 Research Objectives

In the previous two chapters, it was shown that BHCYYb had a higher stability than BZCYYb and similar conductivity. While hafnium and zirconium are chemically similar, it is still possible that yttrium and ytterbium are not the best dopants for the $BaHfO_3$ system and there is further room to improve the conductivity of hafnium-based barium perovskites using novel dopants. Therefore, this chapter will attempt to:

1. Identify novel dopants for the $BaHfO_3$ system and evaluate their performance.
2. Optimize the concentration of any promising dopants.

6.2 Theoretical Evaluation of Dopants

There are two distinct classes of dopants into the perovskite system: A-site and B-site. An A-site dopant consists of replacing a barium with a singly charged alkali metal ion. A B-site dopant would replace either a hafnium or cerium ion with a 3+ metal ion. DFT evaluations of a variety of A-site and B-site dopants were carried out by Lei Zhang and the conclusions from his calculations are shown in Figure 6-1 and Figure 6-2.[94] From these DFT calculations we can see that in the SOFC operating temperature range (~550-750 ^oC) potassium, rubidium, and cesium all outperform the reference "BHO-ref" case. However, for B-site dopants, we can see that no dopant outperforms the reference case. (The "BHO-ref" is not un-doped $BaHfO_3$. Rather it is a non-physical $BaHfO_{2.875}$ which is used as a reference point for comparison)

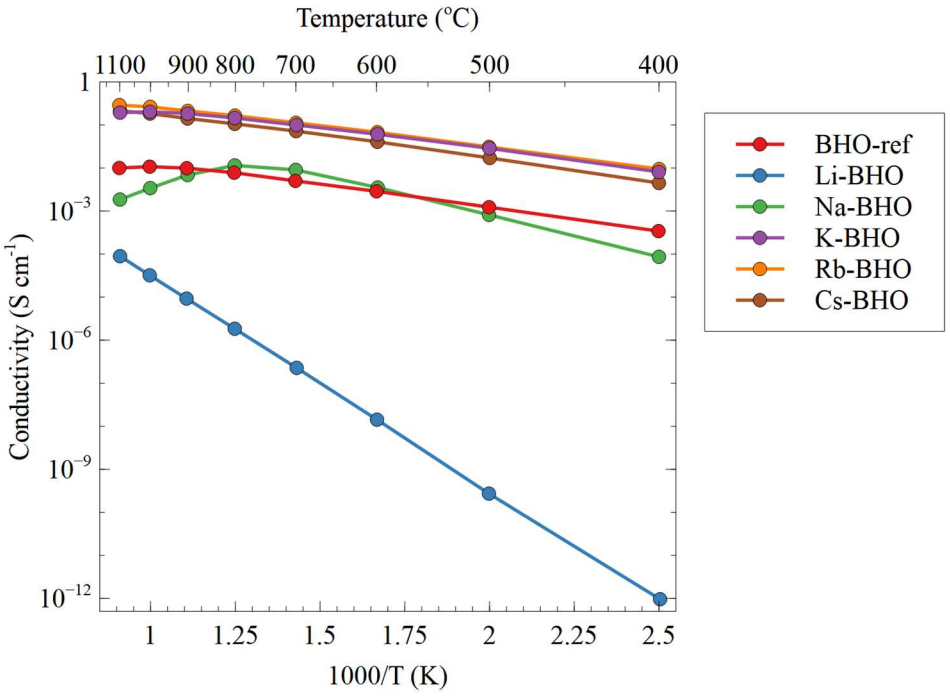

Figure 6-1 Estimation of the conductivity of $A_{0.125}Ba_{0.875}HfO_{2.875}$, where A = Li, Na, K, Rb, Cs. The estimations are based on DFT calculations of hydration and proton mobility. Pure BHO is a benchmark representing an oxygen deficient $BaHfO_{2.875}$.

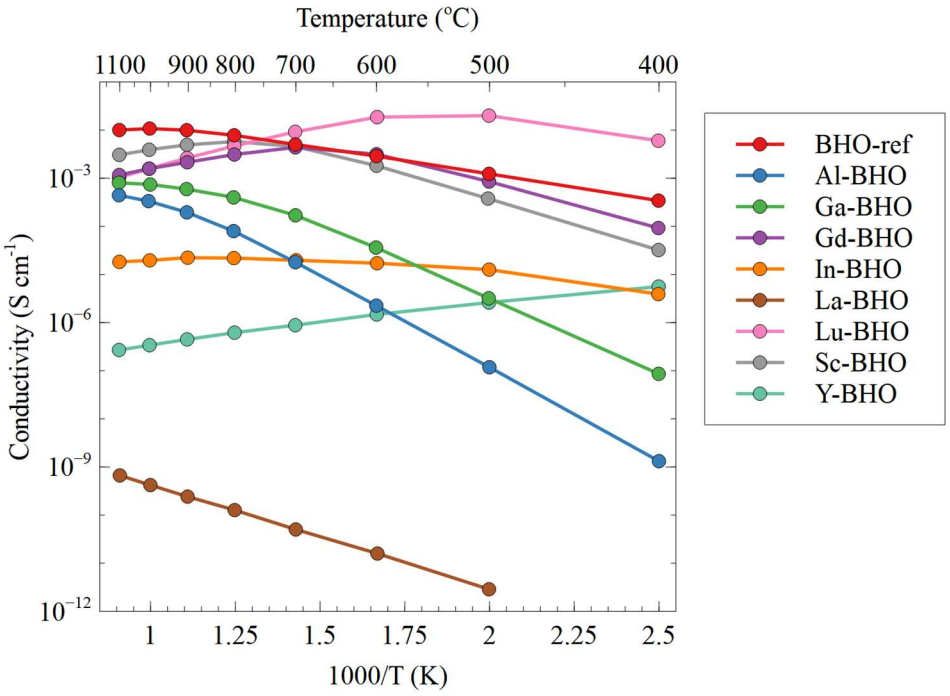

Figure 6-2 Conductivity of $BaHf_{0.875}X_{0.125}O_3$ as determined via DFT calculations where X is a tri-valent dopant.

6.3 A-site Dopants

Based on the theoretical calculations, A-site dopants were studied first. Initially, the solid-state reaction method described previously was used to attempt to fabricate the A-site doped $BaHfO_3$. However, it was quickly realized that the instability of the A-site dopants required a lower temperature synthesis method. Therefore, the glycine-nitrate combustion process was used.

Unfortunately, using the lower temperature combustion method also did not result in an A-site doped material. Initially, only potassium doped $BaHfO_3$ was attempted due to potassium's similar ionic radius to barium, likely increasing its stability, and the DFT

estimation it would be the best performing dopant.[52], [72], [94] Figure 6-3(a) shows XRD scans of the combustion powder before and after calcination. It can clearly be seen that initially there is a significant amount of barium carbonate and hafnium oxide present. After the calcination step at 1000 ^{o}C only the perovskite phase is present. However, as can be seen from the XPS spectrum in Figure 6-3(b), there is no potassium present after the 1000^{o}C calcination step. Finally, TGA of the combustion powder was performed (Figure 6-3(c)). There are two clear major mass loss events at ~725^{o}C and ~800^{o}C. The first mass loss event can be attributed to the conversation of the barium carbonate to the perovskite phase and the corresponding loss of CO_2. The second mass loss is therefore likely the loss of the potassium. This is also supported by the higher decomposition temperature of potassium carbonate relative to barium carbonate: 891^{o}C and 811^{o}C respectively.[104]

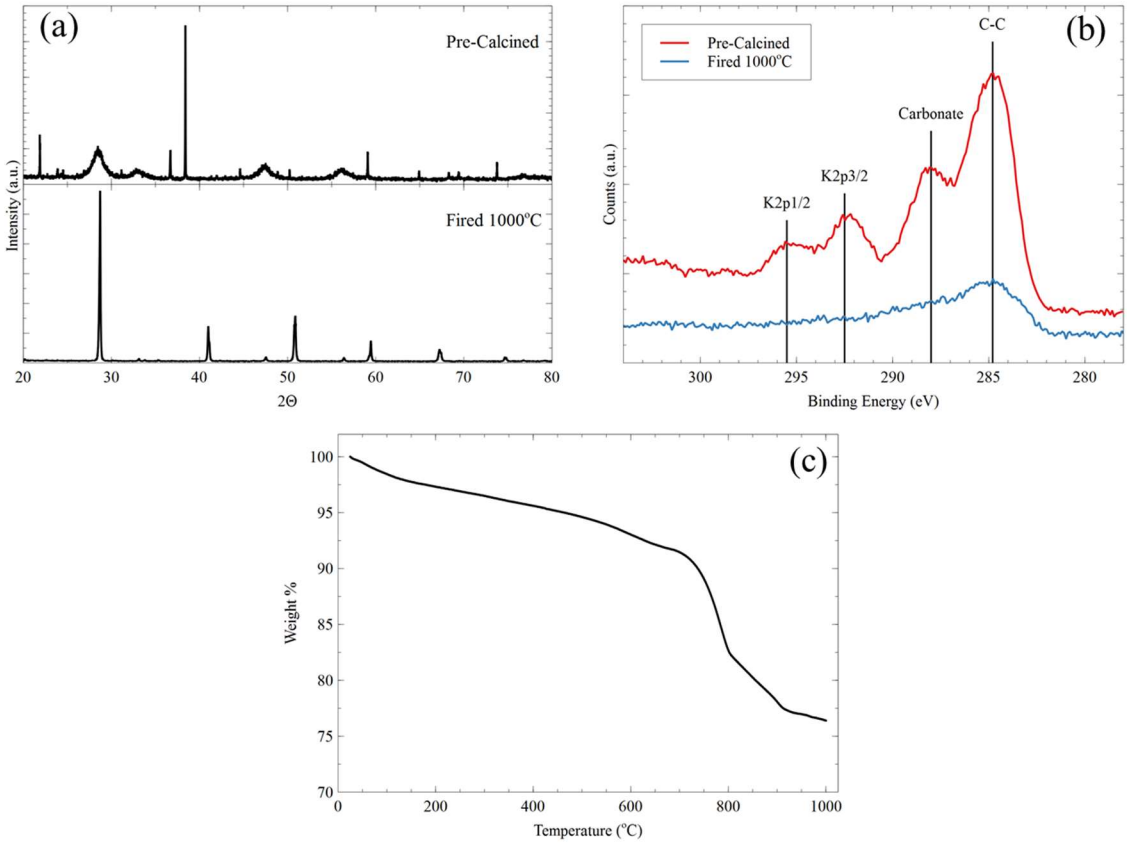

Figure 6-3 Analysis of the combustion fabrication process for $K_{0.125}Ba_{0.875}HfO_3$. (a) XRD spectrum of $K_{0.125}Ba_{0.875}HfO_3$ before and after calcination at 1000°C. (b) XPS spectra of the C1s and K2p binding energies for $K_{0.125}Ba_{0.875}HfO_3$ before and after calcination. (c) TGA profile of $K_{0.125}Ba_{0.875}HfO_3$ before calcination.

Overall, while A-site doped barium hafnate looks very promising, they have proved to be too difficult to fabricate through classical ceramic processing techniques. The temperature at which the potassium evaporation occurs is very close to the temperature required to react the barium carbonate into the perovskite phase. Therefore, it would be very difficult to fabricate phase pure material. More exotic processing techniques may be able to fabricate the material successfully but were not explored at this time.

6.4 B-Site Dopants

While the theoretical calculations predicted that A-site dopants would result in higher performance, they were unable to be fabricated. Therefore, B-site dopants were also studied. Several different dopants were chosen to be studied: yttrium, ytterbium, lutetium, gadolinium, scandium, and indium. These elements were chosen not only due to their high potential results from computations, but also because they represented different types potential dopants. Yttrium and ytterbium were chosen due to their use in the current state of the art electrolyte, BZCYYb. lutetium and gadolinium were both chosen as lanthanides with full and half-full f-orbitals respectively. Finally, scandium has empty d-orbitals and indium has full d-orbitals.

Before the conductivity of the B-site doped material could be tested, they needed to be sintered. $BaHfO_3$ has a higher melting point and therefore sintering temperature than that of $BaZrO_3$ or $BaCeO_3$.[104] Furthermore, the B-site dopant itself can change the sintering temperature, even with the addition of 1 weight percent NiO as a sintering aid. For example, yttrium and ytterbium doped $BaHfO_3$ both required 1650^{o}C to fully densify while gadolinium and lutetium were both fully dense at 1450^{o}C (all samples were sintered for 5 hours). Scandium and indium were both sintered at 1600^{o}C. Figure 6-4 shows the XRD patterns of the B-site doped $BaHfO_3$ after sintering at their respective sintering temperatures and Figure 6-5 shows SEM images of their cross sections which show they are all phase pure and fully dense.

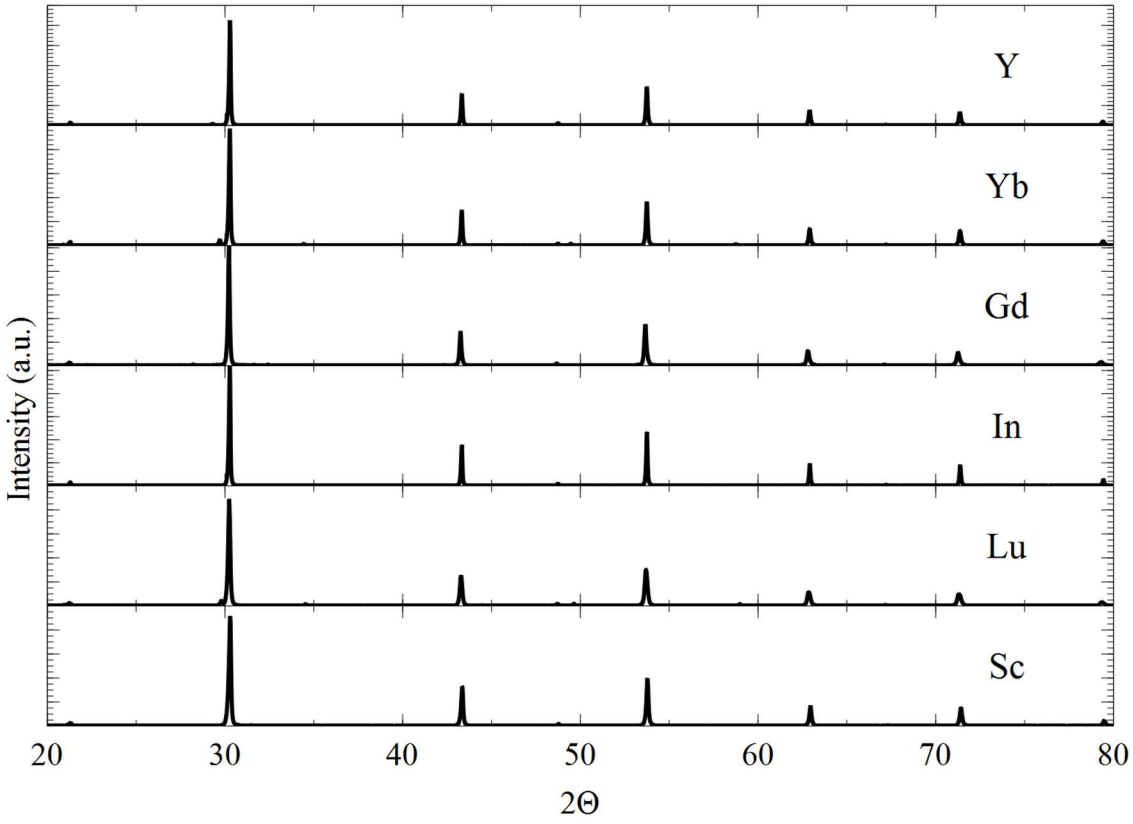

Figure 6-4 XRD of $BaHf_{0.875}X_{0.125}O_3$ (X = Y, Yb, Sc, In, Gd, and Lu) which shows all are the fully cubic perovskite phase.

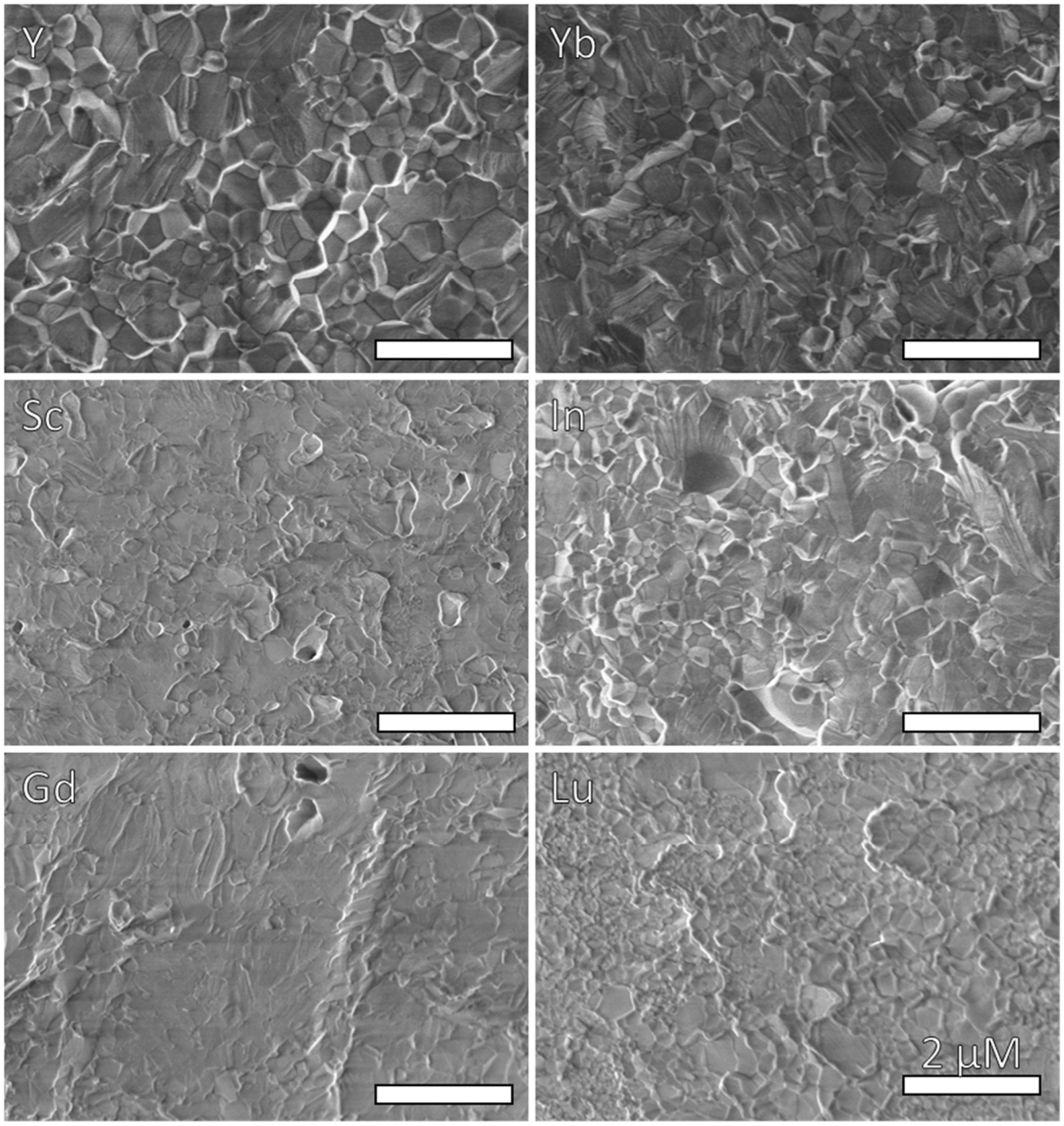

Figure 6-5 SEM images of sintered $BaHf_{0.875}X_{0.125}O_3$ (X = Y, Yb, Sc, In, Gd, and Lu)

After all the different dopants were fully sintered, EIS was used to test their conductivity in argon with 3% water. The conductivity results are shown in Figure 6-6 along with BHCYYb with 10% and 70% hafnium for reference. Surprisingly, yttrium and ytterbium perform the worst out of all the dopants, even though they are the preferred choice for barium cerate-based systems.[80], [82] Lutetium, gadolinium, and scandium all perform

approximately the same but with scandium outperforming slightly, especially at higher temperatures. Finally, indium out-performs all the other dopants by a significant margin. When compared to the BHCYYb, $BaHf_{0.875}In_{0.125}O_3$ outperforms the 70% hafnium BHCYYb, which has a higher concentration of trivalent elements in the B-site.

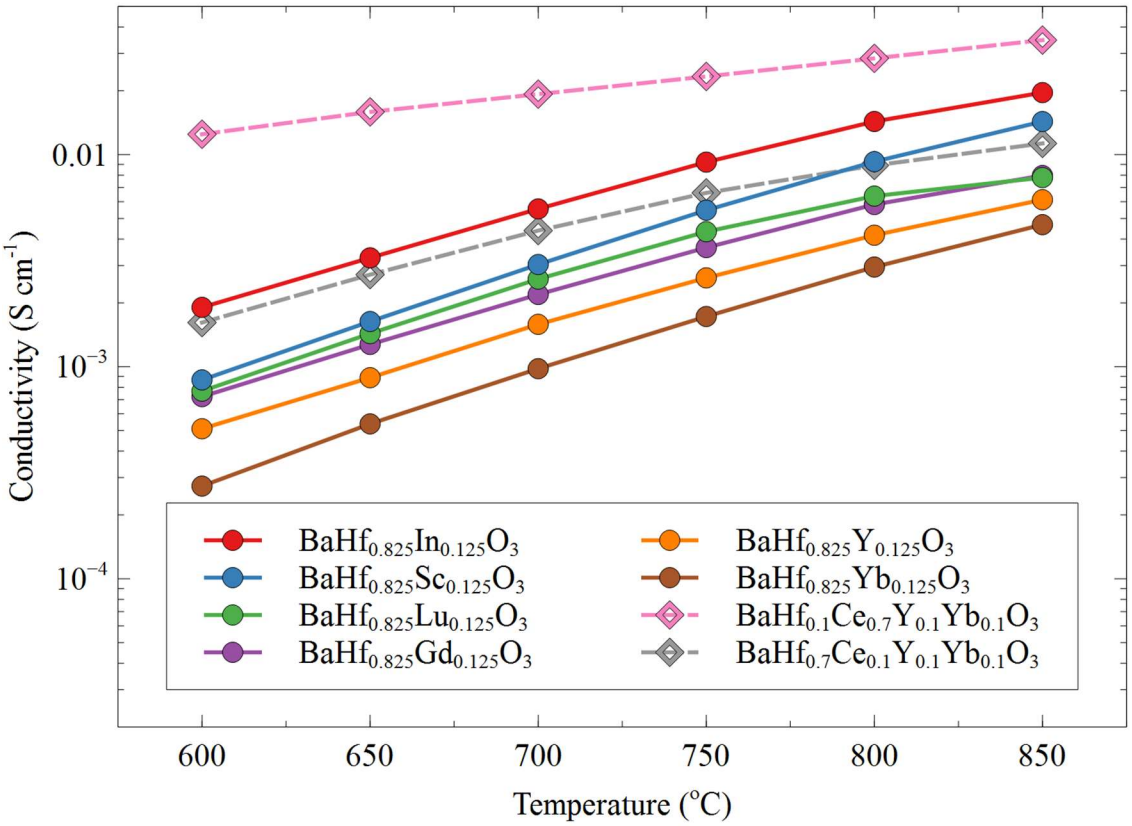

Figure 6-6 Conductivity of $BaHf_{0.875}X_{0.125}O_3$ (X = Y, Yb, Sc, In, Lu, Gd) and BHCYYb in argon with 3% water.

6.5 Optimization of the Indium Concentration in $BaHfO_3$

After indium was identified as an improvement over yttrium and ytterbium in the $BaHfO_3$ system, it was important to optimize the concentration of indium. This is due to the tradeoff between an increase in charge carriers and the trapping effect. The increase in the dopant concentration increases the number of charge carriers, due to an increase in the number of oxygen vacancies formed. However, the mobility of the charge carriers is hindered by the charge centers created by the replacement of a cerium or hafnium ion with indium. These charge centers will "trap" the mobile species and reduce mobility. At even higher concentrations, the dopant will reduce the symmetry of the structure and in extreme cases, results in a different phase. Figure 6-7 shows the XRD of $BaHf_xIn_{1-x}O_{3-\delta}$ which shows that the material retains its cubic perovskite phase up 37.5% indium, the highest concentration tested.

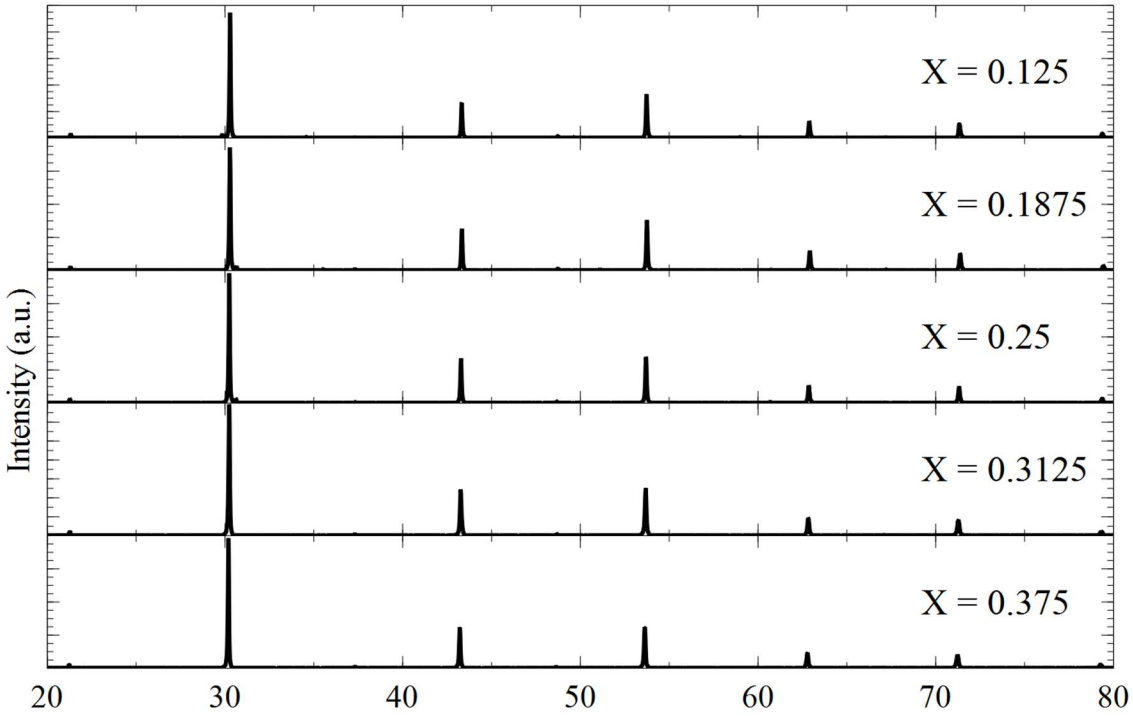

Figure 6-7 X-ray diffraction patterns of $BaHf_{1-x}In_xO_3$ which show the material maintains the cubic perovskite structure up to 37.5% indium doping.

To determine the optimal concentration of indium dopant, the indium concentration was varied between 12.5% and 37.5% and the results are shown in Figure 6-8. We can see that the optimal dopant amount varies slightly as a function of temperature. At 600 ^oC and 650 ^oC there is little to no difference in conductivity as a function of indium concentration. This is likely because most of the charge carriers do not have enough thermal energy to overcome the trapping effect and the increase in dopant does not create mobile charge carriers. As the temperature is increased, we see a peak in the conductivity emerge at ~20% indium. 20% is in line with other dopants in similar systems such as $BaZrO_3$ and $BaCeO_3$.

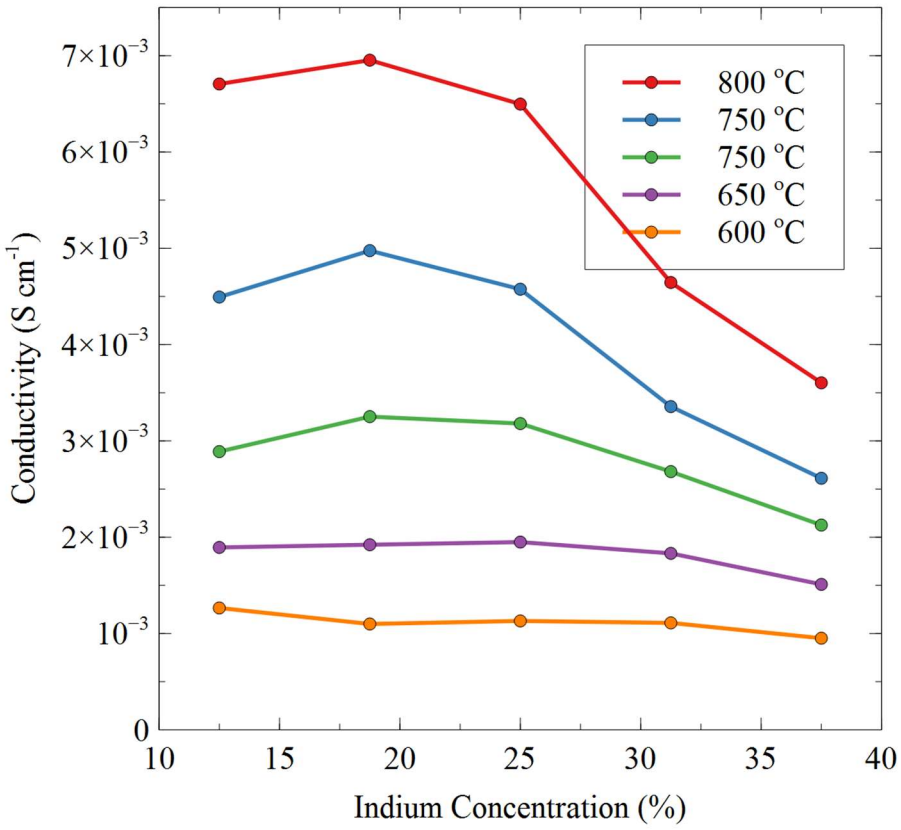

Figure 6-8 Concentration of $BaHf_{1-x}In_xO_{3-\delta}$ as a function of indium concentration and temperature.

Based on the results above, the logical next step was to attempt to further increase the conductivity by replacing some of the hafnium with ceria. As the effect of indium is different in the $BaCeO_3$ system from the $BaHfO_3$ system, two different systems were studied: $BaHf_{0.1}Ce_{0.7}Y_{0.2-x}In_xO_{3-\delta}$ and $BaHf_{0.4}Ce_{0.4}Y_{0.2-x}In_xO_{3-\delta}$. Yttrium was chosen as a co-dopant as it has been shown to be one of the best performing trivalent dopants in the $BaCeO_3$ system. Figure 6-9 shows the conductivities of the two different BHCYIn systems tested. Unfortunately, it appears that in all cases the addition of indium will decrease the conductivity.

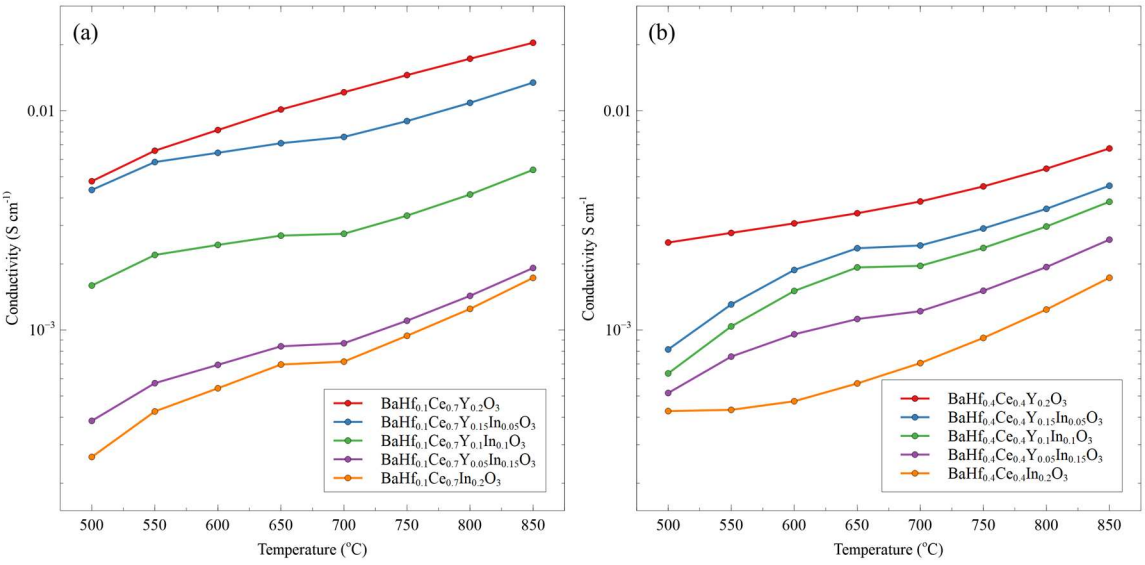

Figure 6-9: Conductivity of (a) $BaHf_{0.1}Ce_{0.7}Y_{0.2-x}In_xO_{3-\delta}$ and (b) $BaHf_{0.4}Ce_{0.4}Y_{0.2-x}In_xO_{3-\delta}$ in 3% H_2O in argon.

There have been many studies into the effect of different dopants in the $BaCeO_3$ system and indium has performed poorly. It appears that the low conductivity of indium in $BaCeO_3$ will outweigh the positive effect of indium in the $BaHfO_3$ system. One possible explanation for these results is the trade-off between charge carrier concentration and mobility. In $BaCeO_3$ indium has been shown to increase the hydration and therefore the charge carrier concentration but the trapping effect caused by the charge center restricts the number of mobile charge carriers. The net effect is an overall reduction in the conductivity of indium doped $BaCeO_3$ compared to other dopants such as yttrium. A major difference between indium doped $BaCeO_3$ and indium doped $BaHfO_3$ is the relative differences between the ionic radius of indium and cerium or hafnium. Indium has an ionic radius of 94 pm compared to 101 pm for cerium and 85 pm for hafnium.[72] The difference in ionic radii in indium doped $BaCeO_3$ would restrict the lattice around the indium, enhancing the trapping effect. In indium doped $BaHfO_3$, the opposite would be true. The lattice would

expand and reduce the trapping effect. This is supported by yttrium's ionic radius of 104 pm, which is larger than both hafnium and cerium.

6.6 Conclusions

Several different types of dopants were studied in the $BaHfO_3$ system, both dopants in the barium site and the hafnium site. Unfortunately, most dopants proved to be unsuccessful for various reasons. Alkali metal A-site dopants were shown to be impossible to dope into the structure using common ceramic processing techniques. This was shown to be due to the low degradation and evaporation of alkali oxides. The evaporation of potassium from $K_{0.125}Ba_{0.875}HfO_3$ was shown to occur at ~800°C while the temperature required to react $BaCO_3$ into the perovskite structure is ~725°C. These temperatures are too low to perform much of the standard ceramic material processing such as sintering (1450°C), adhering of cathode material (1000°C), or adhering of silver current collectors (800°C).

In addition to A-site dopants, tri-valent B-site dopants were also studied. Several different dopants were studied, and indium was determined to have the highest conductivity with the conductivity of $BaHf_{0.875}In_{0.125}O_3$ being higher than even $BaHf_{0.7}Ce_{0.1}Y_{0.1}Yb_{0.1}O_{3-\delta}$. The concentration of indium in $BaHfO_3$ was optimized to be 20%. Finally, $BaHf_{0.1}Ce_{0.7}Y_{0.2-x}In_xO_{3-\delta}$ and $BaHf_{0.4}Ce_{0.4}Y_{0.2-x}In_xO_{3-\delta}$ were tested but unfortunately the detrimental effects of indium in the $BaCeO_3$ system out weighted the advantage of it in the $BaHfO_3$ system and any addition of indium into the mixed $BaCeO_3$-$BaHfO_3$ system resulted in a decrease in conductivity.

CHAPTER 7. CONCLUSIONS AND RECOMMENDATIONS

7.1 Summary of Results

This work describes the development and testing of a new family of solid oxide proton conducting electrolytes, $BaHf_xCe_{0.8-x}Y_{0.1}Yb_{0.1}O_3$ (BHCYYb), and compares its stability and performance to the current state-of-the-art. BHCYYb was rationally designed through the thermodynamic evaluation of barium perovskites to determine their relative stability and it was found that $BaHfO_3$ has the highest intrinsic stability. In addition to the study of the BHCYYb family of materials, doped $BaHfO_3$ was also studied to attempt to further improve performance but it unfortunately proved unfruitful.

After initial thermodynamic calculations were performed, the first tests were on the performance of the BHCYYb system. The conductivity, activation energy, transference number, and fuel cell performance were studied. The conductivity of BHCYYb was found to be similar to that of BZCYYb but varied depending on the concentration of hafnium/zirconium. For example, at low concentrations (10% or 20%) BHCYYb had a higher conductivity than that of BZCYYb. However, as the concentration of Hf/Zr increased the conductivity of both BZCYYb and BHCYYb decreased but BHCYYb decreased at a faster rate. This resulted in BZCYYb and BHCYYb having approximately the same conductivity at 30% Zr/Hf and BZCYYb had the higher conductivity at higher concentrations of Zr/Hf. In addition to conductivity, the transference number, or fraction of ionic to electronic conductivity, was measured. It was seen that transference number decreased as the temperature increased and increased as the concentration of hafnium increased. However, at SOFC operating temperatures, the transference number was above

90% which is sufficient for a high performing material. Finally, BHCYYb was used to fabricate full lab scale fuel cells. The performance of these cells was comparable or higher than that of other proton conducting solid oxide fuel cells, verifying BHCYYb's performance as a proton conducting electrolyte.

After BHCYYb's performance was verified as a proton conducing electrolyte, the stability of BHCYYb was compared to that of BZCYYb. Stability was initially measured with TGA which showed that BHCYYb with 30% hafnium was stable against CO_2 but BZCYYb with 30% zirconium still degraded. Next long-term tests were conducted in 25% CO_2, 25% H_2O, 50% H_2 where chemical stability and conductivity were measured. Again, it was shown that BHCYYb was more stable than that of BZCYYb. Moreover, the major degradation products were shown to be $BaCO_3$ and $Hf_xCe_{1-x}O_3$. When BHCYYb was used as an electrolyte material for SOEC operation for both hydrogen production and CO_2-H_2O co-electrolysis, the cells were stable for several hundred hours while BZCYYb based cells degraded within the first 50 hours.

Finally, doped $BaHfO_3$ was studied to attempt to further improve the performance of barium hafnate based proton conductors. Dopants were attempted in both the barium site (A-site) and the hafnium site (B-site). Several different B-site dopants were tested, and indium doping was shown to have significantly higher conductivity than yttrium or ytterbium doping. However, when indium was used in a mixed $BaHfO_3$-$BaCeO_3$ system, the conductivity was significantly worse than yttrium doping. Most likely due to indium's poor performance in the $BaCeO_3$ system. Lastly, potassium was attempted to be doped into the barium site. However, this proved to be very unstable and it was shown that the potassium evaporates from the structure at a similar temperature to that of the conversion

of carbonates to oxides (~800ºC). This makes fabrication and post-processing of the material impossible with traditional ceramic processing techniques.

Overall, BHCYYb was shown to be an excellent solid oxide proton conducting electrolyte material with better or comparable conductivity and transference numbers than that of the current state-of-the-art BZCYYb. Moreover, BHCYYb has higher stability against CO_2 and water than BZCYYb which makes BHCYYb an excellent choice for applications such as SOFC operation on hydrocarbons or the electrolysis of CO_2.

7.2 Recommendations for Future Work

Based on the results presented in this work, there are three major directions possible to further improve and optimize the performance of BHCYYb and related $BaHfO_3$ materials: further study under both SOFC and SOEC operation, the effect of surface coatings, and further optimization of dopants.

The logical next step for studying BHCYYb is to test it in more real-world applications. This work showed its potential as an SOFC electrolyte using hydrogen as fuel. However, BHCYYb's true strength lies with its stability so tests using hydrocarbon fuels such as natural gas are needed to further verify its stability. Additionally, more robust and longer term tests in SOEC mode to electrolyze CO_2 into syngas or other similar electrolysis process are needed. Finally, if those are successful, it will be important to move beyond lab-scale and test BHCYYb as part of cell stack where fuel utilization will create a wider range of gas conditions and stability is of higher priority.

While BHCYYb does provide some advantages to both performance and stability over BZCYYb, there is still a significant trade-off between stability and performance based on the concentration of hafnium. A traditional method for limiting this trade-off is the use of surface coatings. For example, the fuel cell could be fabricated out of a high conductivity version of BHCYYb (10% hafnium). To protect this from degradation, a higher stability version of BHCYYb would be coated onto the surface of the cell. This would protect the cell from degradation while allowing most of the cell to maintain its high conductivity. There would be several methods by which surface coating could be applied such as atomic layer deposition, surface sol-gel, or simple nitrate infiltration. Of these methods, atomic layer deposition may be the simplest to implement as hafnium oxide has commonly available ALD precursors. However, ALD of complex, multi-doped structure is difficult and rarely performed. Nitrate infiltration is most commonly used for these complex systems. However, hafnium nitrate is not readily available, which could make initial studies difficult.

Finally, the $BaHfO_3$ system is far from fully studied and significant work could still be performed to explore further dopants. The current dopants of yttrium and ytterbium were the worst performing ternary dopants tested. While indium is a poor choice due to its' low conductivity in the $BaCeO_3$ system, other ternary dopants such as lutetium may provide higher performance in the $BaCeO_3$-$BaHfO_3$ system. Moreover, computations suggest that A-site dopants should outperform any B-site dopants so there is significant potential to improve performance through novel processing techniques.

APPENDIX A. SINTERING AIDS FOR BARIUM HAFNATE

A.1 Introduction

One of the most important aspects of developing a new electrolyte material is ensuring the material is fully dense. If there is porosity in the material it can drastically decrease performance. Firstly, if the electrolyte is porous, the gas from the anode and cathode can mix. In the best case, this will decrease the open circuit voltage and therefore performance. At worst, this can be an explosion hazard, although unlikely at lab-scales. Additionally, even if the material is gas tight with only closed porosity the pores will increase the path ions have to travel. This will decrease the conductivity and therefore decrease the overall cell performance.

Barium perovskites require very high sintering temperatures, especially $BaZrO_3$ and $BaHfO_3$. These high temperatures, typically around 1500-1600^oC cause additional problems such as barium evaporation from the structure. This has been overcome for BZCYYb using NiO as a sintering aid. NiO will react with the barium and yttrium to form BaY_2NiO_5. BaY_2NiO_5 has a melting point of around 1450-1500^oC.[105] This relatively low melting point combined with the reaction between the NiO and the BZCYYb has reduced the required sintering temperature to as low as 1400^oC.

While NiO has performed as an excellent sintering aid for BZCYYb and other yttrium doped barium perovskites, the introduction of novel dopants into the $BaHfO_3$ structure will likely reduce the effectiveness of NiO as a sintering aid due to the absence of yttrium and the inability to form the BaY_2NiO_5 phase. In order to effectively sinter these newly

developed materials, additional sintering aids were tested and compared to NiO as sintering aids for $BaHfO_3$. Specifically, CuO and $LiNO_3$ were tested at 1 wt%, 2.5 wt%, and 5 wt% in addition to NiO. CuO was chosen due to the low melting point of the BaO-CuO system, ~ 875°C.[106], [107] Additionally, Amsif *et al* showed that the application of CuO had minimal impact on conductivity of various B-site doped barium cerates.[108] $LiNO_3$ was chosen due to the fact that it completely evaporates from the structure during the sintering process and therefore does not affect the final conductivity.[109] Most importantly neither CuO or $LiNO_3$ rely on yttrium to be present in order to enhance the sintering process.

A.2 Technical Approach

To test the effectiveness of CuO, and $LiNO_3$ as sintering aids, 1 wt%, 2.5 wt% and 5 wt% of CuO, and $LiNO_3$ were mixed into $BaHfO_3$, which was prepared using the standard solid-state reaction process. To ensure the sintering aids were well mixed, they were processed with high energy ball milling after the sintering aid was added to the $BaHfO_3$. The powders were then pressed into pellets and fired at various temperatures (1500°C, 1550°C, 1600°C, and 1650°C) for 5 hours. The pellets were then fractured, and the fractured cross-section was analyzed via SEM.

A.3 Results and Discussion

Figure A-1, Figure A-2, and Figure A-3 show cross sections of $BaHfO_3$ sintered at various temperatures using $LiNO_3$ as a sintering aid at 1 wt%, 2.5 wt%, and 5 wt% respectively. At all concentrations of $LiNO_3$, the higher sintering temperature resulted in larger particle sizes due to the faster grain growth at elevated temperatures. Additionally, the higher the sintering temperature, the higher the density of the material. However, increasing the

sintering aid did not increase the density. We do see a slight increase in density as the concentration of $LiNO_3$ is increased from 1 wt% to 2.5 wt%. However, increasing the concentration further to 5 wt% resulted in a lower density. This is mostly likely due to the extremely low boiling point of $LiNO_3$ at 600°C. The high concentration of $LiNO_3$ acted as a pore former at 5 wt% and increased the porosity compared to lower concentrations.

Figure A-4, Figure A-5, and Figure A-6 show cross sections of $BaHfO_3$ sintered at various temperatures using CuO as a sintering aid at 1 wt%, 2.5 wt%, and 5 wt% respectively. Again, we see larger particle sizes at higher sintering temperatures but there does not appear to be any increase in density at the higher sintering temperatures. There does appear to be an increase in density as we increase the CuO concentration but unfortunately even at 5 wt% and 1650°C the material is not completely dense.

Due to the lack of success with CuO and $LiNO_3$, NiO was attempted as a sintering aid even in the absence of yttrium. Figure A-7 shows the cross section of $BaHfO_3$ with 1 wt% and 2 wt% NiO as sintering aid fired at 1500°C. We can see that even the 1500°C and 1 wt% the material is dense. Increasing the concentration to 2 wt% increases the grain size slightly but otherwise maintains a similar morphology.

One possible explanation for the success of NiO over CuO or $LiNO_3$ is the higher eutectic temperature of the NiO-BaO system compared to the eutectic temperature of the BaO-CuO system or the melting point of $LiNO_3$. The eutectic temperature of the NiO-BaO system is ~1100°C.[110] An eutectic temperature closer to the final sintering point helps to prevent the evaporation of the sintering aid and results in an overall denser material.

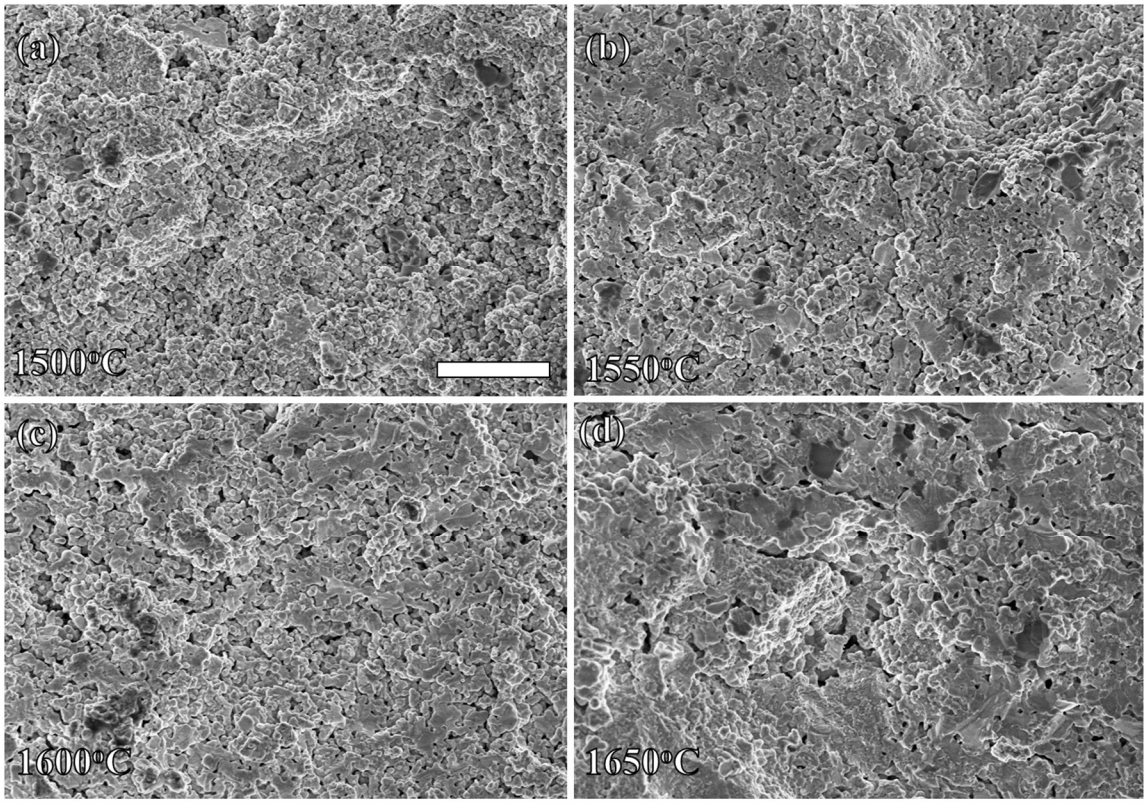

Figure A-1 SEM images of $BaHfO_3$ cross sections after sintering at (a) 1500°C, (b) 1550°C, (c) 1600°C, and (d) 1650°C for 5 hours with 1 wt% $LiNO_3$ added as a sintering aid. Scale bar is 5 µm

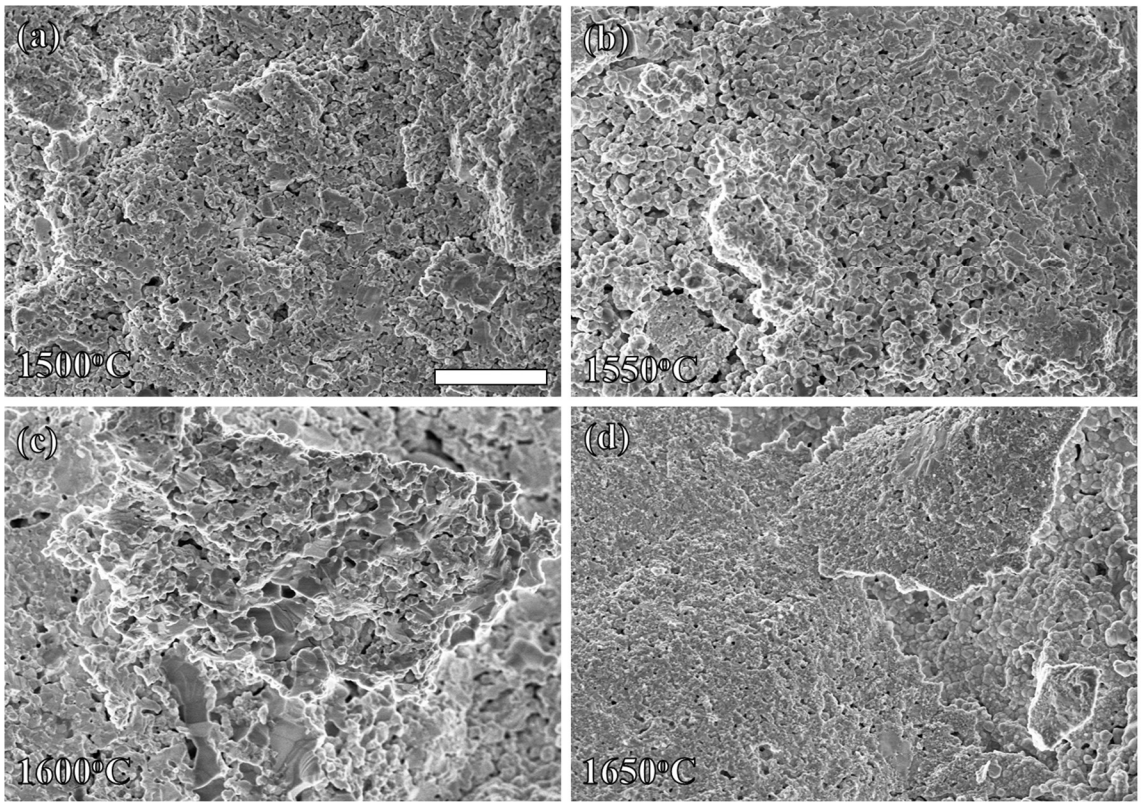

Figure A-2 SEM images of $BaHfO_3$ cross sections after sintering at (a) 1500°C, (b) 1550°C, (c) 1600°C, and (d) 1650°C for 5 hours with 2.5 wt% $LiNO_3$ added as a sintering aid. Scale bar is 5 µm

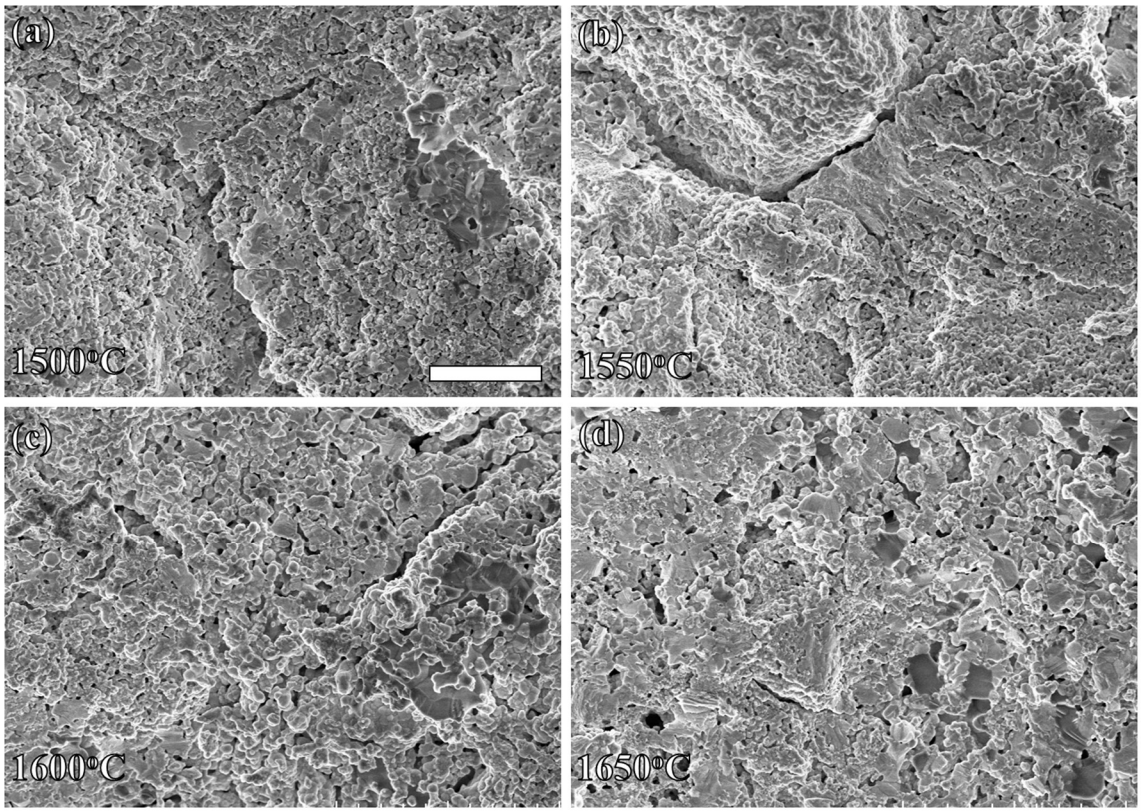

Figure A-3 SEM images of $BaHfO_3$ cross sections after sintering at (a) 1500°C, (b) 1550°C, (c) 1600°C, and (d) 1650°C for 5 hours with 5 wt% $LiNO_3$ added as a sintering aid. Scale bar is 5 µm

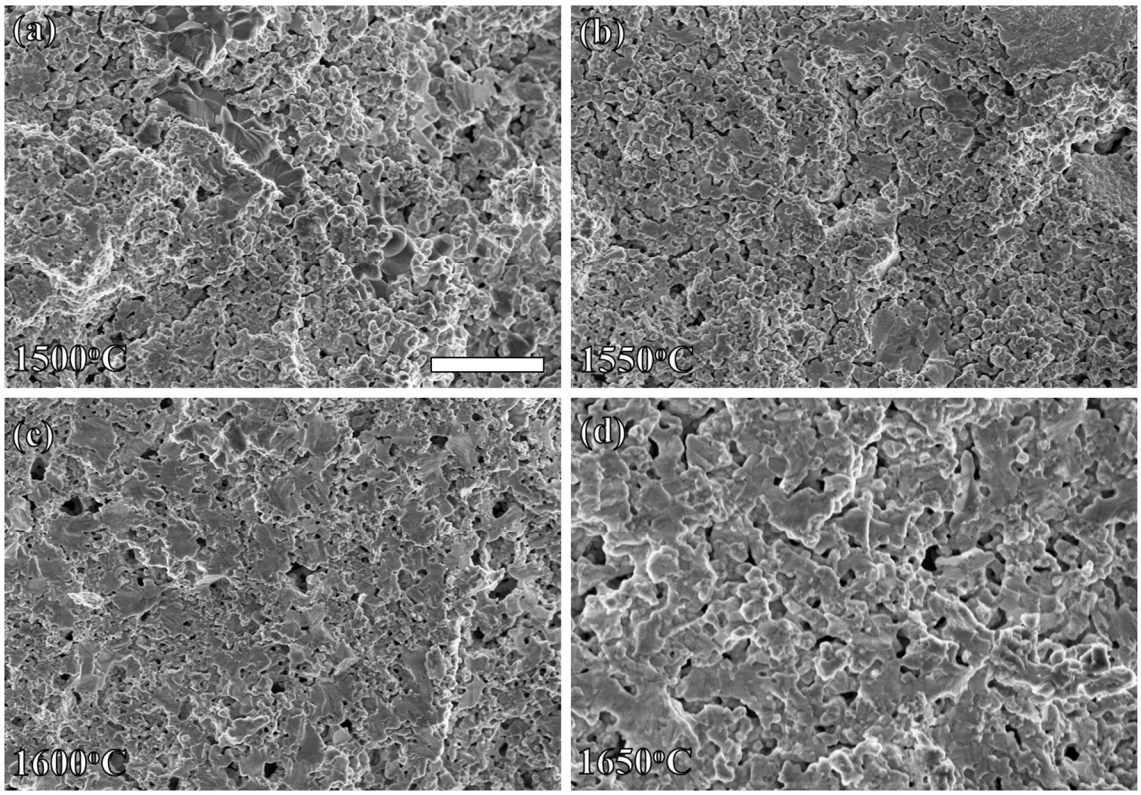

Figure A-4 SEM images of $BaHfO_3$ cross sections after sintering at (a) 1500°C, (b) 1550°C, (c) 1600°C, and (d) 1650°C for 5 hours with 1 wt% CuO added as a sintering aid. Scale bar is 5 µm

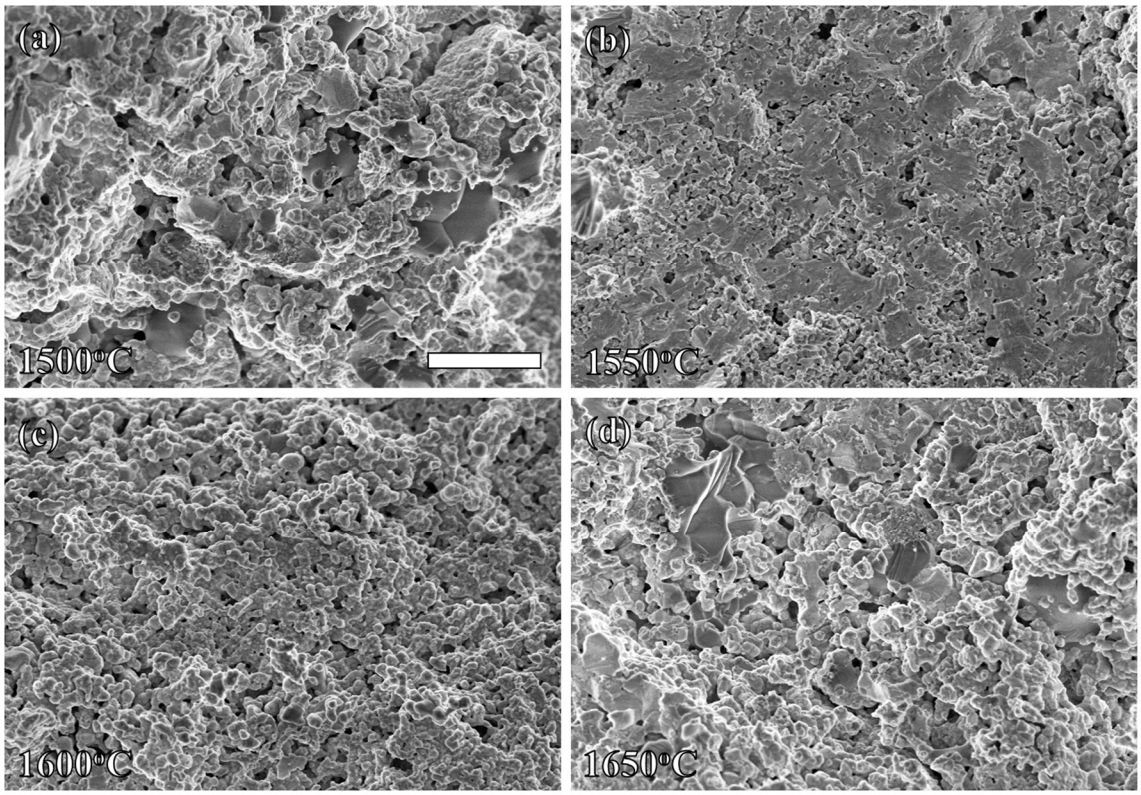

Figure A-5 SEM images of $BaHfO_3$ cross sections after sintering at (a) 1500°C, (b) 1550°C, (c) 1600°C, and (d) 1650°C for 5 hours with 2.5 wt% CuO added as a sintering aid. Scale bar is 5 µm

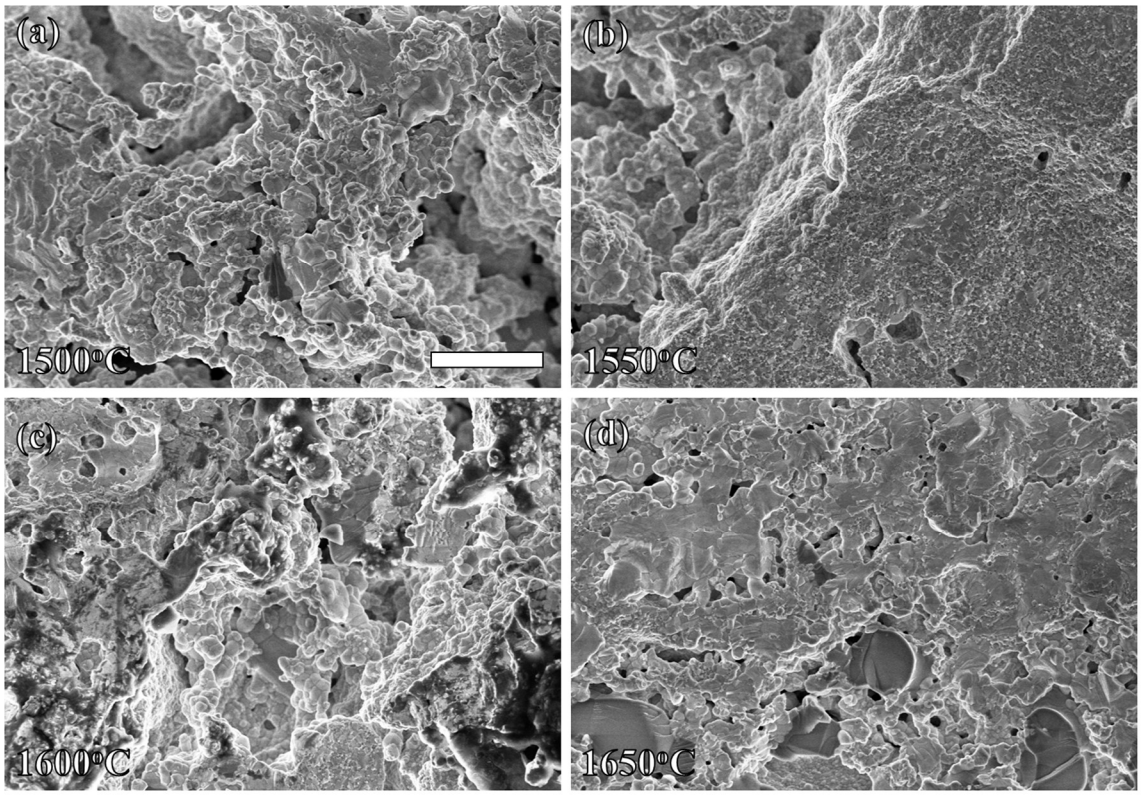

Figure A-6 SEM images of $BaHfO_3$ cross sections after sintering at (a) 1500°C, (b) 1550°C, (c) 1600°C, and (d) 1650°C for 5 hours with 5 wt% CuO added as a sintering aid. Scale bar is 5 µm

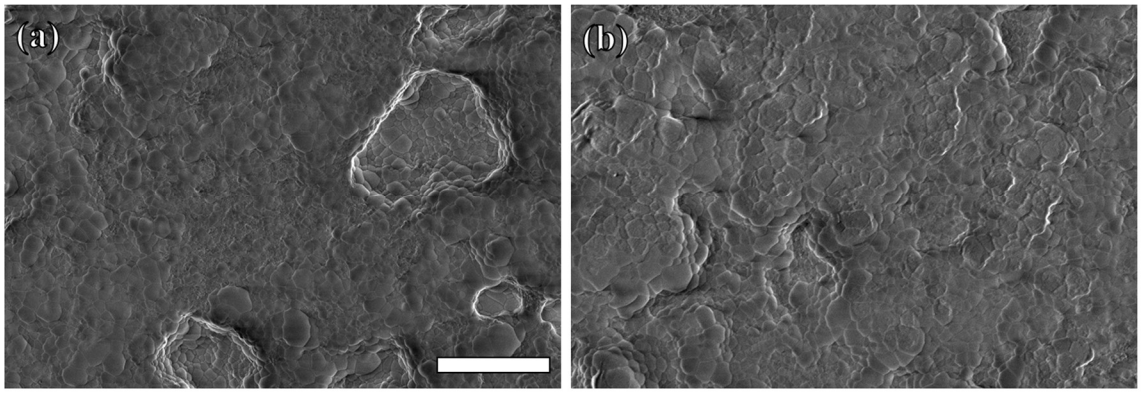

Figure A-7 SEM images of $BaHfO_3$ cross sections after sintering at 1500°C 5 hours with (a) 1 wt% NiO and (b) 2 wt% NiO added as a sintering aid. Scale bar is 5 µm

A.4 Conclusions

Three different sintering aids, $LiNO_3$, CuO, and NiO, for $BaHfO_3$ were tested at a variety of temperatures and concentrations. An increase in temperature always resulted in larger particle sizes and higher densities at the same sintering aid concertation. $LiNO_3$ slightly increased density at low concentrations but higher concentrations acted as a pore-former due to the low boiling point of $LiNO_3$. CuO performed slightly better with higher apparent densities, although full density was not achieved. Finally, NiO was shown to still be the most effective sintering aid, even in the absence of yttrium. Fully dense pellets were achieved at 1500°C with 1 wt% NiO. The success of NiO is attributed to the 1100°C eutectic temperature of the BaO-NiO system.

APPENDIX B. CONSTANTS AND METHODS USED FOR THERMODYNAMIC CALCULATIONS

B.1 Constants for Fitted Thermodynamic Data

Thermodynamic data gathered from *Thermochemical Data of Pure Substances, 3rd Edition* by Barin Ihsan[71] and other literature sources. The exact source is cited for each material. The data was fitted to the Shomate equation as shown in equation (29) using the MATLAB curve fitting toolbox.

$$G = a * t * \ln(t) + b * t + c * t^2 + d * t^3 + e * t^4 + f * t^{-1} + g \quad \textbf{(29)}$$

Where G is given in kJ and where

$$t = \frac{Temperature\ (K)}{1000} \quad \textbf{(30)}$$

Table B-1 Constants for the Shomate equation (equation (29)) fitted to tabulated thermodynamic data

	CO_2 [71]	H_2O [71]	$BaCO_3$ [71]	$Ba(OH)_2$ (<681 K) [71]
a	-34.84	-23.23	-87.08	186.5
b	-209.00	-190.3	-107.2	282.6
c	-14.77	-10.84	-25.68	-801.6
d	2.032	-0.7124	0.7208	-500
e	-0.1497	-0.01672	-0.3803	-163.5
f	0.3756	-0.2586	0.7114	1.005
g	-407.9	-248	-1249	-932.5

	$Ba(OH)_2$ (>681 K) [71]	$BaZrO_3$ [46], [71]	ZrO_2 [71]	BaCeO3 [111]
a	155.4	-123.4	-100.4	-120.3
b	-141.9	-135.9	-75.6	-158.9
c	11.62	-3.659	37.2	-7.899
d	-2.289	-0.1952	-12.66	0.6193
e	0.2337	0.02504	1.947	-0.1123
f	1.004	1.114	1.395	0.5658
g	-989.5	-1846	-1134	-1727
	CeO_2 [71]	$BaHfO_3$ [46], [71]	HfO_2 [71]	
a	-54.52	-122.5	-71.55	
b	-28.16	-133.5	-64.24	
c	-57.69	-8.64	-5.131	
d	21.7	0.6451	0.1452	
e	-3.628	-0.1081	-0.01686	
f	1.811	0.8386	0.6301	
g	-1120	-1902	-1171	

B.2 MATLAB Code for Producing 2- Dimensional van't Hoff Plots

The below code is for the calculation of the reaction between $BaZr_xCe_{1-x}O_3$ and CO_2. However, it can be easily modified for any solid solution system and any contaminate for which the thermodynamic constants can be obtained.

```
clear;
Start=298;
End=1273;
E=(End-Start)+1;
for Q=1:E
    T=Q-1+Start;
    t=T/1000;
    %all euations should be in Absolute free energy and in kJ
    %final calcuation will *1000 to convert to J
    % absolute free energy of CO2
    a=-34.84;
    b=-209;
    c=-14.77;
    d=2.032;
    e=-0.1497;
    f=0.3756;
    g=-407.9;
    Gco=(a*t*log(t)+b*t+c*t^2+d*t^3+e*t^4*f*t^-1+g)*1000;

    % free energy of BaCO3
```

```
    a=-87.08;
    b=-107.2;
    c=-25.68;
    d=0.7208;
    e=-0.3803;
    f=0.7114;
    g=-1249;
    Gba=(a*t*log(t)+b*t+c*t^2+d*t^3+e*t^4*f*t^-1+g)*1000;

    % formation energy of ZrO2
    a=-100.4;
    b=-75.6;
    c=37.2;
    d=-12.66;
    e=1.947;
    f=1.395;
    g=-1134;
    Gzr=(a*t*log(t)+b*t+c*t^2+d*t^3+e*t^4*f*t^-1+g)*1000;

    %formation energy of CeO2
    a=-54.52;
    b=-28.16;
    c=-57.69;
    d=21.7;
    e=-3.628;
    f=1.811;
    g=-1120;
    Gce=(a*t*log(t)+b*t+c*t^2+d*t^3+e*t^4*f*t^-1+g)*1000;

    % formation energy of BaZrO3
    a=-123.4;
    b=-135.9;
    c=-3.659;
    d=-0.1952;
    e=0.02504;
    f=1.114;
    g=-1846;
    Gbzr=(a*t*log(t)+b*t+c*t^2+d*t^3+e*t^4*f*t^-1+g)*1000;

    %formation energy of BaCeO3
    a=-120.3;
    b=-158.9;
    c=-7.899;
    d=0.6193;
    e=-0.1123;
    f=0.5658;
    g=-1727;
    Gbce=(a*t*log(t)+b*t+c*t^2+d*t^3+e*t^4*f*t^-1+g)*1000;

    for Con=1:999
        x=Con/1000;
        R=8.3145;
        %calculate the formation energy of ZrxCe1-xO2
        omega=0;
        Gmixcezr=R*T*((x)*log(x)+(1-x)*log(1-x))+(omega*x*(1-x)); %G of
mixing for Zr in CeO2
```

```
        Gcezr=Gmixcezr+(x*Gzr)+((1-x)*Gce); % energy of formation of
ZrxCe1-xO2
        %calculate the formation energy of BaZrxCe1-xO3
        omega=0; %for BaZrO3 into BaCeO3
        Gmixbzcyyb=R*T*((x)*log(x)+(1-x)*log(1-x))+(omega*x*(1-x)); % G
of mixing for Ce&Zr in BaZrxCe1-xO3
        Gbzcyyb=Gmixbzcyyb+(x*Gbzr)+((1-x)*Gbce);

        Grxn=(Gba+Gcezr-Gbzcyyb-Gco)/1000;
        K=exp(-Grxn*1000/(8.314*T));
        Pco=1/K;
        FreeEnergy{Con,Q}=Grxn;
        Constant{Con,Q}=K;
        Pressure{Con,Q}=Pco;
    end

end
FreeEnergyTable = cell2table(FreeEnergy);
PressureTable = cell2table(Pressure);
writetable(FreeEnergyTable,['BaZrO3_BaCeO3_CO2_Free_Energy.csv']);
writetable(PressureTable,['BaZrO3_BaCeO3_CO2_Pressure.csv']);
```

APPENDIX C. COPYRIGHT AGREEMENT LETTERS

Permission for Figure 2-2(B)

Annual Reviews, Inc LICENSE TERMS AND CONDITIONS

Jul 30, 2019

This is a License Agreement between Georgia Institute of Technology -- Ryan Murphy ("You") and Annual Reviews, Inc ("Annual Reviews, Inc") provided by Copyright Clearance Center ("CCC"). The license consists of your order details, the terms and conditions provided by Annual Reviews, Inc, and the payment terms and conditions.

All payments must be made in full to CCC. For payment instructions, please see information listed at the bottom of this form.

License Number	4638911074282
License date	Jul 30, 2019
Licensed content publisher	Annual Reviews, Inc
Licensed content title	Annual review of materials research
Licensed content date	Jan 1, 2001
Type of Use	Thesis/Dissertation
Requestor type	Academic institution
Format	Print, Electronic
Portion	chart/graph/table/figure
Number of charts/graphs /tables/figures	1
The requesting person/organization is:	Ryan Murphy
Title or numeric reference of the portion(s)	Figure 6
Title of the article or chapter the portion is from	Proton-Conducting Oxides
Editor of portion(s)	N/A
Author of portion(s)	K.D. Kreuer
Volume of serial or monograph.	33
Page range of the portion	333-359
Publication date of portion	August 2003
Rights for	Main product
Duration of use	Life of current and all future editions
Creation of copies for the disabled	no
With minor editing privileges	yes
For distribution to	Worldwide
In the following language(s)	Original language of publication
With incidental promotional use	no
The lifetime unit quantity of new product	Up to 499
Title	A NEW FAMILY OF PROTON CONDUCTING ELECTROLYTES WITH ENHANCED STABILITY FOR REVERSIBLE FUEL CELL OPERATION: BaHfxCe0.8-xY0.1Yb0.1O3
Institution name	Georgia Institute of Technology

REFERENCES

[1] J. S. Carlton, R. Perry-Hill, M. Huber, and L. S. Prokopy, "The climate change consensus extends beyond climate scientists," *Environ. Res. Lett.*, vol. 10, no. 9, 2015.

[2] K. Rice *et al.*, "Consensus on consensus: a synthesis of consensus estimates on human-caused global warming," *Environ. Res. Lett.*, vol. 11, no. 4, p. 048002, 2016.

[3] P. T. Doran and M. K. Zimmerman, "Examining the Scientific Consensus on Climate Change," *Eos, Trans. Am. Geophys. Union*, vol. 90, no. 3, p. 22, 2009.

[4] W. R. L. Anderegg, J. W. Prall, J. Harold, and S. H. Schneider, "Expert credibility in climate change," *Proc. Natl. Acad. Sci.*, vol. 107, no. 27, pp. 12107–12109, 2010.

[5] J. L. Powell, "Climate Scientists Virtually Unanimous," *Bull. Sci. Technol. Soc.*, vol. 35, no. 5–6, pp. 121–124, Oct. 2015.

[6] U.S Energy Information Administration, "Annual Energy Outlook 2018," 2018.

[7] The Core Writing Team, R. K. Pachauri, and L. A. Meyer, "Climate Change 2014: Synthesis Report. Contribution of Working Groups I, II and III to the Fifth Assessment Report of the Intergovernmental Panel on Climate Change," IPCC, Geneva, Switzerland, 2014.

[8] B. K. Sovacool, M. A. Brown, and S. V Valentine, *Fact and Fiction in Global Energy Policy*. Baltimore: John Hopkins, 2016.

[9] M. A. Brown and B. K. Sovacool, *Climate Change and Global Energy Security*. Cambridge, MA: The MIT Press, 2011.

[10] S. C. Singhal and K. Kendall, "Chapter 01 - Introduction to SOFCs," in *High Temperature and Solid Oxide Fuel Cells*, S. C. Singhal and K. Kendal, Eds. Amsterdam: Elsevier Science, 2003, pp. 1–22.

[11] L. Carrette, K. A. Friedrich, and U. Stimming, "Fuel Cells: Principles, Types, Fuels, and Applications," *ChemPhysChem*, vol. 1, no. 4, pp. 162–193, 2000.

[12] M. Carmo, D. L. Fritz, J. Mergel, and D. Stolten, "A comprehensive review on PEM water electrolysis," *Int. J. Hydrogen Energy*, vol. 38, no. 12, pp. 4901–4934, Apr. 2013.

[13] K. Zeng and D. Zhang, "Recent progress in alkaline water electrolysis for hydrogen production and applications," *Progress in Energy and Combustion Science*, vol. 36, no. 3. pp. 307–326, Jun-2010.

[14] J. D. Holladay, J. Hu, D. L. King, and Y. Wang, "An overview of hydrogen production technologies," *Catal. Today*, vol. 139, no. 4, pp. 244–260, 2009.

[15] D. A. Hickman and L. D. Schmidt, "Production of Syngas by Direct Catalytic Oxidation of Methane," *Science (80-.).*, vol. 259, no. 5093, pp. 343–346, Jan. 1993.

[16] Herminé Nalbandian, "Coal Conversion to Chemicals , Gaseous and Liquid Fuels," in *Gasification Technologies Conference*, 2014.

[17] D. S. Sholl and R. P. Lively, "Seven chemical separations to change the world,"

Nature, vol. 532, no. 7600, pp. 435–437, Apr. 2016.

[18] A. T. Ashcroft, A. K. Cheetham, M. L. H. Green, and P. D. F. Vernon, "Partial oxidation of methane to synthesis gas using carbon dioxide," *Nature*, vol. 352, no. 6332, pp. 225–226, Jul. 1991.

[19] D. Dissanayake, "Partial oxidation of methane to carbon monoxide and hydrogen over a Ni/Al2O3 catalyst," *J. Catal.*, vol. 132, no. 1, pp. 117–127, Nov. 1991.

[20] A. Choudhury, H. Chandra, and A. Arora, "Application of solid oxide fuel cell technology for power generation - A review," *Renew. Sustain. Energy Rev.*, vol. 20, pp. 430–442, 2013.

[21] A. B. Stambouli and E. Traversa, "Solid oxide fuel cells (SOFCs): A review of an environmentally clean and efficient source of energy," *Renew. Sustain. Energy Rev.*, vol. 6, no. 5, pp. 433–455, 2002.

[22] L. Bi, S. Boulfrad, and E. Traversa, "Steam electrolysis by solid oxide electrolysis cells (SOECs) with proton-conducting oxides," *Chem. Soc. Rev.*, vol. 43, no. 24, pp. 8255–8270, Aug. 2014.

[23] H. Iwahara, T. Esaka, H. Uchida, and N. Maeda, "Proton conduction in sintered oxides and its application to steam electrolysis for hydrogen production," *Solid State Ionics*, vol. 3–4, pp. 359–363, Aug. 1981.

[24] G. Wu, K. Xie, Y. Wu, W. Yao, and J. Zhou, "Electrochemical conversion of H2O/CO2 to fuel in a proton-conducting solid oxide electrolyser," *J. Power*

Sources, vol. 232, pp. 187–192, Jun. 2013.

[25] V. N. Nguyen and L. Blum, “Syngas and Synfuels from H2O and CO2 : Current Status,” *Chemie Ing. Tech.*, vol. 87, no. 4, pp. 354–375, Apr. 2015.

[26] Y. Lin *et al.*, “Proton-conducting fuel cells operating on hydrogen, ammonia and hydrazine at intermediate temperatures,” *Int. J. Hydrogen Energy*, vol. 35, no. 7, pp. 2637–2642, Apr. 2010.

[27] R. Lan, J. T. S. Irvine, and S. Tao, “Synthesis of ammonia directly from air and water at ambient temperature and pressure,” *Sci. Rep.*, vol. 3, no. 1, p. 1145, Dec. 2013.

[28] S. Giddey, S. P. S. Badwal, and A. Kulkarni, “Review of electrochemical ammonia production technologies and materials,” *Int. J. Hydrogen Energy*, vol. 38, no. 34, pp. 14576–14594, Nov. 2013.

[29] B. Smit, “Carbon Capture and Storage: introductory lecture,” *Faraday Discuss.*, vol. 192, no. 0, pp. 9–25, Oct. 2016.

[30] J. Gibbins and H. Chalmers, “Carbon capture and storage,” *Energy Policy*, vol. 36, no. 12, pp. 4317–4322, Dec. 2008.

[31] European Commission, “Novel carbon capture and utilisation technologies,” 2017.

[32] K. Kendall, N. Q. Minh, and S. C. Singhal, “Chapter 08 - Cell and Stack Designs,” in *High Temperature and Solid Oxide Fuel Cells*, S. C. Singhal and K. Kendal, Eds. Amsterdam: Elsevier Science, 2003, pp. 197–228.

[33] H. U. Anderson and F. Tietz, “Chapter 07 - Interconnects,” in *High Temperature and Solid Oxide Fuel Cells*, S. C. Singhal and K. Kendal, Eds. Amsterdam: Elsevier Science, 2003, pp. 173–195.

[34] J. W. Fergus, “Effect of cathode and electrolyte transport properties on chromium poisoning in solid oxide fuel cells,” *Int. J. Hydrogen Energy*, vol. 32, no. 16, pp. 3664–3671, 2007.

[35] S. P. Jiang, J. P. Zhang, and X. G. Zheng, “A comparative investigation of chromium deposition at air electrodes of solid oxide fuel cells,” *J. Eur. Ceram. Soc.*, vol. 22, no. 3, pp. 361–373, 2002.

[36] L. Zhao *et al.*, “Effect of Boron Deposition and Poisoning on the Surface Exchange Properties of LSCF Electrode Materials of Solid Oxide Fuel Cells,” *J. Electrochem. Soc.*, vol. 160, no. 6, pp. F682–F686, 2013.

[37] K. Chen, N. Ai, L. Zhao, and S. P. Jiang, “Effect of Volatile Boron Species on the Electrocatalytic Activity of Cathodes of Solid Oxide Fuel Cells,” *J. Electrochem. Soc.*, vol. 160, no. 3, pp. F301–F308, Jan. 2013.

[38] K. Chen, N. Ai, and S. P. Jiang, “Chemical Compatibility between Boron Oxides and Electrolyte and Cathode Materials of Solid Oxide Fuel Cells,” *Fuel Cells*, vol. 13, no. 6, pp. 1101–1108, 2013.

[39] K. . Kreuer, “On the development of proton conducting materials for technological applications,” *Solid State Ionics*, vol. 97, no. 1–4, pp. 1–15, May 1997.

[40] D. Chen, R. Ran, K. Zhang, J. Wang, and Z. Shao, “Intermediate-temperature electrochemical performance of a polycrystalline PrBaCo2O5+?? cathode on samarium-doped ceria electrolyte,” *J. Power Sources*, vol. 188, no. 1, pp. 96–105, 2009.

[41] F. Jin, Y. Shen, R. Wang, and T. He, “Double-perovskite PrBaCo2/3Fe2/3Cu2/3O5+δ as cathode material for intermediate-temperature solid-oxide fuel cells,” *J. Power Sources*, vol. 234, pp. 244–251, Jul. 2013.

[42] R. Pelosato, G. Cordaro, D. Stucchi, C. Cristiani, and G. Dotelli, “Cobalt based layered perovskites as cathode material for intermediate temperature Solid Oxide Fuel Cells: A brief review,” *J. Power Sources*, vol. 298, pp. 46–67, 2015.

[43] Y. Y. Chen *et al.*, “An In Situ Formed, Dual-Phase Cathode with a Highly Active Catalyst Coating for Protonic Ceramic Fuel Cells,” *Adv. Funct. Mater.*, vol. 1704907, p. 1704907, Dec. 2017.

[44] C. Duan *et al.*, “Highly durable, coking and sulfur tolerant, fuel-flexible protonic ceramic fuel cells,” *Nature*, vol. 557, no. 7704, pp. 217–222, May 2018.

[45] N. Zakowsky, S. Williamson, and J. Irvine, “Elaboration of CO2 tolerance limits of BaCe0.9Y0.1O3–δ electrolytes for fuel cells and other applications,” *Solid State Ionics*, vol. 176, no. 39–40, pp. 3019–3026, Dec. 2005.

[46] S. G. Kang, “Dense Metal and Perovskite Membranes for Hydrogen and Proton Conduction,” Georgia Institute of Technology, 2013.

[47] W. Winkler, “Chapter 03 - Thermodynamics,” in *High Temperature and Solid Oxide Fuel Cells*, S. C. Singhal and K. Kendal, Eds. Amsterdam: Elsevier Science, 2003, pp. 53–82.

[48] H.-H. Möbius, “Chapter 02 - History,” in *High Temperature and Solid Oxide Fuel Cells*, S. C. Singhal and K. Kendal, Eds. Amsterdam: Elsevier Science, 2003, pp. 23–51.

[49] T. Ishihara, N. M. Sammes, and O. Yamamoto, “Chapter 04 - Electrolytes,” in *High Temperature and Solid Oxide Fuel Cells*, S. C. Singhal and K. Kendal, Eds. Amsterdam: Elsevier Science, 2003, pp. 83–117.

[50] S. (Rob) Hui *et al.*, “A brief review of the ionic conductivity enhancement for selected oxide electrolytes,” *J. Power Sources*, vol. 172, no. 2, pp. 493–502, 2007.

[51] K. D. Kreuer, “Proton-Conducting Oxides,” *Annu. Rev. Mater. Res.*, vol. 33, no. 1, pp. 333–359, Aug. 2003.

[52] R. H. Mitchell, *Perovskites Modern and Ancient*. Thunder Bay, Ontario: Almaz Press, 2002.

[53] R. C. T. Slade and N. Singh, “Generation of charge carriers and an H/D isotope effect in proton-conducting doped barium cerate ceramics,” *J. Mater. Chem.*, vol. 1, no. 3, p. 441, Jan. 1991.

[54] L. Malavasi, C. A. J. Fisher, and M. S. Islam, “Oxide-ion and proton conducting electrolyte materials for clean energy applications: structural and mechanistic

features," *Chem. Soc. Rev.*, vol. 39, no. 11, p. 4370, Oct. 2010.

[55] J. Wu, R. A. Davies, M. S. Islam, and S. M. Haile, "Atomistic Study of Doped BaCeO 3 : Dopant Site-Selectivity and Cation Nonstoichiometry," *Chem. Mater.*, vol. 17, no. 4, pp. 846–851, Feb. 2005.

[56] M. M. Liu *et al.*, "High-performance Ni–BaZr0.1Ce0.7Y0.1Yb0.1O3−δ (BZCYYb) membranes for hydrogen separation," *Int. J. Hydrogen Energy*, vol. 38, no. 34, pp. 14743–14749, Nov. 2013.

[57] N. T. Q. Nguyen and H. H. Yoon, "Preparation and evaluation of BaZr0.1Ce0.7Y0.1Yb0.1O3−δ (BZCYYb) electrolyte and BZCYYb-based solid oxide fuel cells," *J. Power Sources*, vol. 231, pp. 213–218, 2013.

[58] B. H. Rainwater, "Electrical Properties of BaZr0.1Ce0.7Y0.1Yb0.1O3-δ and its application in Intermediate Temperature Solid Oxide Fuel Cells," Georgia Institute of Technology, 2012.

[59] L. Yang, "New Materials for Intermediate-Temperature Solid Oxide Fuel Cells To Be Powered By Carbon- and Sulfur-Containing Fuels," Georgia Institute of Technology, 2011.

[60] L. Yang *et al.*, "Enhanced Sulfur and Coking Tolerance of a Mixed Ion Conductor for SOFCs: BaZr0.1Ce0.7Y0.2-xYbxO3-," *Science (80-.).*, vol. 326, no. 5949, pp. 126–129, Oct. 2009.

[61] S. Choi *et al.*, "Exceptional power density and stability at intermediate temperatures

in protonic ceramic fuel cells," *Nat. Energy*, vol. 3, no. 3, pp. 202–210, Mar. 2018.

[62] Y. Chen *et al.*, "A robust fuel cell operated on nearly dry methane at 500 °C enabled by synergistic thermal catalysis and electrocatalysis," *Nat. Energy*, vol. 3, no. 12, pp. 1042–1050, Dec. 2018.

[63] A. Hauch, S. H. Jensen, S. Ramousse, and M. Mogensen, "Performance and Durability of Solid Oxide Electrolysis Cells," *J. Electrochem. Soc.*, vol. 153, no. 9, p. A1741, 2006.

[64] F. Tietz, D. Sebold, A. Brisse, and J. Schefold, "Degradation phenomena in a solid oxide electrolysis cell after 9000 h of operation," *J. Power Sources*, vol. 223, pp. 129–135, 2013.

[65] A. Brisse, A. Schefold, and M. Zahid, "High temperature water electrolysis in solid oxide cells," *Int. J. Hydrogen Energy*, vol. 33, no. 20, pp. 5375–5382, Oct. 2008.

[66] M. A. Laguna-Bercero, "Recent advances in high temperature electrolysis using solid oxide fuel cells: A review," *J. Power Sources*, vol. 203, pp. 4–16, Apr. 2012.

[67] K. H. Ryu and S. M. Haile, "Chemical stability and proton conductivity of doped BaCeO3–BaZrO3 solid solutions," *Solid State Ionics*, vol. 125, no. 1–4, pp. 355–367, Oct. 1999.

[68] E. Fabbri, A. D'Epifanio, E. Di Bartolomeo, S. Licoccia, and E. Traversa, "Tailoring the chemical stability of Ba(Ce0.8−xZrx)Y0.2O3−δ protonic conductors for Intermediate Temperature Solid Oxide Fuel Cells (IT-SOFCs)," *Solid State Ionics*,

vol. 179, no. 15–16, pp. 558–564, Jun. 2008.

[69] P. Sawant, S. Varma, B. N. Wani, and S. R. Bharadwaj, "Synthesis, stability and conductivity of BaCe0.8−xZrxY0.2O3−δ as electrolyte for proton conducting SOFC," *Int. J. Hydrogen Energy*, vol. 37, no. 4, pp. 3848–3856, Feb. 2012.

[70] Outokumpu Research Oy, *HSC Chemistry*, 5.11. 2008.

[71] B. Ihsan, *Thermochemical Data of Pure Substances*, 3rd ed. Weinheim, Germany: Wiley-VCH Verlag GmbH, 1995.

[72] R. D. Shannon, "Revised effective ionic radii and systematic studies of interatomic distances in halides and chalcogenides," *Acta Crystallogr. Sect. A*, vol. 32, no. 5, pp. 751–767, Sep. 1976.

[73] D. A. McQuarrie and J. D. Simon, *Physical Chemistry, A Molecular Approach*. University Science Books, 1997.

[74] S. G. Kang and D. S. Sholl, "Characterizing chemical stability and proton conductivity of B-site doped barium hafnate (BaHfO3) and barium stannate (BaSnO3) with first principles modeling," *J. Alloys Compd.*, vol. 693, pp. 738–743, Feb. 2017.

[75] A. M. Hussain, K.-J. Pan, I. A. Robinson, T. Hays, and E. D. Wachsman, "Stannate-Based Ceramic Oxide as Anode Materials for Oxide-Ion Conducting Low-Temperature Solid Oxide Fuel Cells," *J. Electrochem. Soc.*, vol. 163, no. 10, pp. F1198–F1205, Aug. 2016.

[76] D. S. Rivera, T. Ishimoto, and M. Koyama, “Density Functional Theory Study on the Catalytic Properties of BaTiO3 as Solid Oxide Fuel Cell Anode,” *ECS Trans.*, vol. 57, no. 1, pp. 2723–2732, Oct. 2013.

[77] J.-H. Li, X.-Z. Fu, J.-L. Luo, K. T. Chuang, and A. R. Sanger, “Application of BaTiO3 as anode materials for H2S-containing CH4 fueled solid oxide fuel cells,” *J. Power Sources*, vol. 213, pp. 69–77, Sep. 2012.

[78] N. Osman, I. A. Talib, H. A. Hamid, and A. M. Jani, “Characterization, electrical conduction and stability of Yb-doped barium cerate prepared by sol-gel method,” *Ionics (Kiel).*, vol. 14, no. 5, pp. 407–413, Sep. 2008.

[79] N. Bonanos, B. Ellis, K. S. Knight, and M. N. Mahmood, “Ionic conductivity of gadolinium-doped barium cerate perovskites,” *Solid State Ionics*, vol. 35, no. 1–2, pp. 179–188, Jul. 1989.

[80] J. Wu, L. P. Li, W. T. P. Espinosa, and S. M. Haile, “Defect chemistry and transport properties of BaxCe0.85M0.15O3-δ,” *J. Mater. Res.*, vol. 19, no. 08, pp. 2366–2376, Aug. 2004.

[81] S. Ricote and N. Bonanos, “Enhanced sintering and conductivity study of cobalt or nickel doped solid solution of barium cerate and zirconate,” *Solid State Ionics*, vol. 181, no. 15–16, pp. 694–700, Jun. 2010.

[82] E. Gilardi *et al.*, “Effect of Dopant–Host Ionic Radii Mismatch on Acceptor-Doped Barium Zirconate Microstructure and Proton Conductivity,” *J. Phys. Chem. C*, vol. 121, no. 18, pp. 9739–9747, 2017.

[83] A. Løken, S. W. Saeed, M. N. Getz, X. Liu, and T. S. Bjørheim, “Alkali metals as efficient A-site acceptor dopants in proton conducting BaZrO 3,” *J. Mater. Chem. A*, vol. 4, no. 23, pp. 9229–9235, 2016.

[84] D.-K. Lim, H.-N. Im, S.-J. Song, and H.-I. Yoo, “Hydration of Proton-conducting BaCe0.9Y0.1O3−δ by Decoupled Mass Transport,” *Sci. Rep.*, vol. 7, no. 1, p. 486, Dec. 2017.

[85] A. VahidMohammadi and Z. Cheng, “Fundamentals of Synthesis, Sintering Issues, and Chemical Stability of BaZr 0.1 Ce 0.7 Y 0.1 Yb 0.1 O 3-δ Proton Conducting Electrolyte for SOFCs,” *J. Electrochem. Soc.*, vol. 162, no. 8, pp. F803–F811, Jan. 2015.

[86] X. Zhou *et al.*, “Ionic conductivity, sintering and thermal expansion behaviors of mixed ion conductor BaZr0.1Ce0.7Y0.1Yb0.1O3−δ prepared by ethylene diamine tetraacetic acid assisted glycine nitrate process,” *J. Power Sources*, vol. 196, no. 11, pp. 5000–5006, Jun. 2011.

[87] S. Choi *et al.*, “Highly efficient and robust cathode materials for low-temperature solid oxide fuel cells: PrBa0.5Sr0.5Co(2-x)Fe(x)O(5+δ).,” *Sci. Rep.*, vol. 3, p. 2426, 2013.

[88] Y. Liu, L. Yang, M. Liu, Z. Tang, and M. Liu, “Enhanced sinterability of BaZr0.1Ce0.7Y0.1Yb0.1O3−δ by addition of nickel oxide,” *J. Power Sources*, vol. 196, no. 23, pp. 9980–9984, Dec. 2011.

[89] Furiouslettuce, “Bragg Diffraction Planes,” 2009. [Online]. Available:

https://commons.wikimedia.org/wiki/File:BraggPlaneDiffraction.svg. [Accessed: 31-Jul-2019].

[90] Gamry Instruments, "Basics of Electrochemial Impedance Spectroscopy." [Online]. Available: https://www.gamry.com/application-notes/EIS/basics-of-electrochemical-impedance-spectroscopy/. [Accessed: 18-Jun-2019].

[91] J. Guan, S. E. Dorris, U. Balachandran, and M. Liu, "Transport properties of BaCe0.95Y0.05O3−α mixed conductors for hydrogen separation," *Solid State Ionics*, vol. 100, no. 1–2, pp. 45–52, Sep. 1997.

[92] T. Matsui, M. Inaba, A. Mineshige, and Z. Ogumi, "Electrochemical properties of ceria-based oxides for use in intermediate-temperature SOFCs," *Solid State Ionics*, vol. 176, no. 7–8, pp. 647–654, Feb. 2005.

[93] A. R. Denton and N. W. Ashcroft, "Vegard's law," *Phys. Rev. A*, vol. 43, no. 6, 1991.

[94] L. Zhang, "Atomic Level Simulations of Proton Conducting BaHfO3 with A/B-Site Dopants," Georgia Institute of Technology, 2019.

[95] L. Heyne, "Electrochemistry of mixed ionic-electronic conductors," in *Solid Electrolytes*, G. S., Ed. Berlin, Heidelberg: Springer, 1977, pp. 169–221.

[96] W. Huang, P. Shuk, M. Greenblatt, M. Croft, F. Chen, and M. Liu, "Structural and Electrical Characterization of a Novel Mixed Conductor: CeO 2-Sm 2 O 3-ZrO 2 Solid Solution," 2000.

[97] J. Kim *et al.*, "Triple-Conducting Layered Perovskites as Cathode Materials for Proton-Conducting Solid Oxide Fuel Cells," *ChemSusChem*, vol. 7, no. 10, pp. 2811–2815, Oct. 2014.

[98] K. Bae *et al.*, "Demonstrating the potential of yttrium-doped barium zirconate electrolyte for high-performance fuel cells," *Nat. Commun.*, vol. 8, no. 1, p. 14553, Apr. 2017.

[99] C. Duan *et al.*, "Readily processed protonic ceramic fuel cells with high performance at low temperatures.," *Science*, vol. 349, no. 6254, pp. 1321–6, Sep. 2015.

[100] P. Pasierb, S. Komornicki, M. Rokita, and M. Rękas, "Structural properties of Li2CO3–BaCO3 system derived from IR and Raman spectroscopy," *J. Mol. Struct.*, vol. 596, no. 1–3, pp. 151–156, Sep. 2001.

[101] T. Taniguchi *et al.*, "Identifying Defects in Ceria-Based Nanocrystals by UV Resonance Raman Spectroscopy," *J. Phys. Chem. C*, vol. 113, no. 46, pp. 19789–19793, Nov. 2009.

[102] M. Guo, J. Lu, Y. Wu, Y. Wang, and M. Luo, "UV and Visible Raman Studies of Oxygen Vacancies in Rare-Earth-Doped Ceria," *Langmuir*, vol. 27, no. 7, pp. 3872–3877, Apr. 2011.

[103] T. Scherban, R. Villeneuve, L. Abello, and G. Lucazeau, "Raman scattering study of BaCeO3 and SrCeO3," *Solid State Commun.*, vol. 84, no. 3, pp. 341–344, Oct. 1992.

[104] D. R. Lide and H. P. R. Frederikse, Eds., *CRC Handbook of Chemistry and Physics. 77th Edition*, 77th ed. CRC Press, 1997.

[105] J. Tong, D. Clark, L. Bernau, M. Sanders, and R. O'Hayre, "Solid-state reactive sintering mechanism for large-grained yttrium-doped barium zirconate proton conducting ceramics," *J. Mater. Chem.*, vol. 20, no. 30, p. 6333, Jul. 2010.

[106] M. Biswas *et al.*, "Thermal Evolution of BaO-CuO Flux as Sintering Aid for Proton Conducting Ceramic Fuel Cells," *J. Korean Ceram. Soc.*, vol. 53, no. 5, pp. 506–510, Sep. 2016.

[107] C. Changkang, H. Yongle, B. M. Wanklyn, and J. W. Hodby, "Crystal growth of CuO from BaO flux," *J. Cryst. Growth*, vol. 129, pp. 239–242, 1993.

[108] M. Amsif, D. Marrero-López, J. C. C. Ruiz-Morales, S. N. N. Savvin, and P. Núñez, "Effect of sintering aids on the conductivity of BaCe0.9Ln 0.1O3-δ," *J. Power Sources*, vol. 196, no. 22, pp. 9154–9163, Nov. 2011.

[109] Z. Sun, E. Fabbri, L. Bi, and E. Traversa, "Lowering grain boundary resistance of BaZr 0.8 Y 0.2 O 3−δ with LiNO 3 sintering-aid improves proton conductivity for fuel cell operation," *Phys. Chem. Chem. Phys.*, vol. 13, no. 17, pp. 7692–7700, Apr. 2011.

[110] J. J. Lander, "The Phase System BaO-NiO," *J. Am. Chem. Soc.*, vol. 73, no. 6, pp. 2450–2452, Jun. 1951.

[111] H. P. Cordfunke, A. S. Booij, and M. E. Huntelaar, "The thermochemical properties

of BaCeO3(s) and SrCeO3(s) from T=(5 to 1500) K," *J. Chem. Thermodyn.*, vol. 30, pp. 437–447, 1998.